NASA CONTRACT NO. NAS8-36146
FINAL REPORT

MEASUREMENT OF DAMPING OF GRAPHITE EPOXY MATERIALS & STRUCTURAL JOINTS

Sponsored by:

NATIONAL AERONAUTICS & SPACE ADMINISTRATION
GEORGE C. MARSHALL SPACE FLIGHT CENTER
HUNTSVILLE, AL 35812

RESEARCH REPORT

Submitted by:

MALCOLM J. CROCKER
MOHAN D. RAO
P.K. RAJU
XINCHE YAN

MECHANICAL ENGINEERING DEPARTMENT
AUBURN UNIVERSITY

AUGUST 1989

NASA CONTRACT NO. NAS8-36146

FINAL REPORT

MEASUREMENT OF DAMPING OF GRAPHITE EPOXY COMPOSITE MATERIALS & STRUCTURAL JOINTS

Period: October 1984 - June 1989

Sponsored By:

National Aeronautics & Space Administration
George C. Marshall Space Flight Center
Huntsville, AL. 35812

Submitted By:

Malcolm J. Crocker, Principal Investigator.
Mohan D. Rao, Graduate Research Assistant
P.K. Raju, Associate Professor.
Xinche Yan, Visiting Scholar.

AUGUST 1989

TABLE OF CONTENTS

LIST OF TABLES

LIST OF FIGURES

I. INTRODUCTION

Motivation

Owing to their favorable performance characteristics, composite materials have been gaining wide use in commercial, military and spacecraft applications. Typical commercial applications include building materials, sports equipment, and automobile parts such as drive shafts, engines, leaf springs and wheels. The main applications of composite materials, however, have been in the aerospace and defense related projects. Aircraft and spacecraft structures are typically weight-sensitive and advanced composites with high strength-to-weight and stiffness-to-weight ratios have become almost indispensable in such structures.

Spacecraft structures and equipment mounted in these structures are required to operate in hostile environments and to be subjected to a wide range of dynamic loads. When structural resonances are excited, the dynamic loads can produce excessive vibration in the structures and equipment. There is a need for the vibration of the structures to decay as quickly as possible so that it will not affect the normal working and utility of the structures and missions. Vibration can be significantly reduced by increasing the damping in the dominant modes through the application of active and passive damping control devices.

Active control can be used to suppress the vibration by the use of certain active elements such as actuators which alter the dynamic response of the structure. It requires the use of special purpose hardware, and real-time control-design algorithms applicable to individual structural components. Active vibration control technology is still in its primitive stages of development and unfortunately, feasible solutions are still not available to alleviate the vibration problems of real-life complex space structures.

In passive control, energy dissipation can be achieved by external add-on damping devices such as isolators or constrained viscoelastic layers. Yet another source of passive damping in most structures is provided by their joints and supports. The use of passive damping treatments provides a simple and reliable solution for vibration suppression, in limited frequency ranges. A balanced combination of both active and passive damping is, however, likely to be a more realistic and practical solution in future aerospace structures than the use of active or passive control alone.

In any case, a detailed understanding of the inherent damping in the material and the structural system is important. Little information is available on material damping, especially for advanced composite materials. It is difficult to obtain a good understanding of the damping phenomena in a material or structure as there are many mechanisms involved. All these mechanisms eventually involve the conversion of mechanical energy into thermal energy. For composite materials, the damping mechanisms, of course, are more complex because several factors will influence the damping capacity of the material.

These include, but are not limited to: 1) internal friction or hysteresis within each of the constituent materials, 2) interfacial slip at the fiber-matrix interfaces, and 3) fiber orientation and length. Hence damping cannot be estimated easily, but instead must be measured.

The influences of common environmental factors such as moisture and temperature have been found significantly to degrade the matrix dominated mechanical properties of many polymer composites. When moisture is absorbed, the composite gets heavier and the resin matrix expands. Matrix swelling and rapid heating may eventually lead to surface cracking. The amount and type of degradation that this can cause in the mechanical properties of the composite depend on matrix material, fiber content and orientation, cure quality, service temperature, humidity, duration of exposure and geometry of the component. Hence, it is extremely difficult to make theoretical predictions regarding the effects of the above environmental factors on the mechanical properties, particularly the damping capacity of composite materials.

Joints are used in deployable structures as well as in structures which must be assembled in space. Unlike metals, fiber composites cannot be welded together. The alternatives include the use of mechanical fasteners, such as bolts and rivets, or adhesive bonding. These techniques produce joints with vastly different properties. Adhesive bonding is preferred over conventional fastening techniques due to a greater uniformity in load distribution, elimination of drill holes, reduced weight and increased processing ease.

It is believed that bonded (and bolted) joints act to enhance the damping capacity of the structure. The energy dissipation in a joint, however, is a complicated process involving several mechanisms. The characterization of a joint presents many experimental and analytical challenges. Because of the complexity of the problem it appears that very little work is being done in evaluating the damping in joints and built-up structures. Hence there is a considerable need for the contribution of knowledge in the understanding of the damping capacity of joints.

Scope of the Study

The Hubble Space Telescope, which will be placed in orbit by NASA in 1989, is a new telescope which will be able to peer far out in space and back into time, producing images of unprecedented clarity of galaxies, planets and stars billions of light years away from the earth. The Space Telescope requires precise pointing accuracy and its optical system is held together by a truss made of graphite epoxy composite material. Graphite epoxy is a strong, lightweight composite material, developed by NASA in the early 1970s, that expands and contracts very little in response to temperature changes. The metering truss is 5.3 m long and 2.9 m in diameter and has a mass of only 114 kg[1].

The pointing control system of the telescope consists mainly of optical sensors, a digital computer, gyros and four massive reaction wheels. Pointing torques are applied with the reaction wheel assemblies. The reaction wheels produce vibration disturbances when they are rotated due to imbalance of the rotor and imperfections in the spin bearings. The vibration disturbances could excite the system resonances which would lead to significant truss system displacement amplitudes. These would result in the blurring of the optical system image of the space telescope. Vibration suppression of the truss system is provided by passive isolation systems in the form of viscous dashpots[2]. A specific knowledge of the material and system damping of the truss system is mandatory in the design of the passive isolation systems. Hence one of the main objectives of the present research was to evaluate systematically, the damping capacity of the graphite epoxy material of the telescope truss system. Furthermore, since the telescope will operate in space, it is necessary to determine the damping capacity of these materials in a simulated space environment.

When graphite epoxy materials are used in a vacuum environment, they have a tendency to outgas. During outgassing they release all the gases and moisture which were trapped during manufacture. There is some concern, however, that mechanical properties including its material damping may change after the material has outgassed for long periods of time. For graphite epoxy materials, this outgassing can take a period of about six months but this period may be reduced to about 3-4 weeks by heating the material to about $100^{\circ}C$ in a vacuum chamber.

The telescope is expected to experience variations in temperature of as much as $140^{\circ}C$ in space[3]. As mentioned previously, the damping capacity of graphite epoxy materials is considerably influenced by the variation in temperature. Though it is known that temperature affects the damping capacity of these materials, not much work has been done on the behavior of these materials in cryogenic temperatures. Such temperatures may be important during launching and deployment in space.

The truss system of the telescope is a joint-dominated structure. As discussed earlier, the damping provided by joints is a potential source of passive damping which is useful for the suppression of vibration in the truss system. It is not known, however, whether the bonded joints in the truss will significantly increase the damping over the material damping. Analytical and experimental work on the evaluation of system damping of basic structural joints is a good starting point for research in this area. The data derived from simple structures will provide some necessary information which can be used to gain an understanding of the dynamic behavior of complex structures such as the truss system of the telescope.

The other objectives of the present study include, i) a study of the effects of outgassing (moisture desorption), and temperature (both high and low) on the damping capacity of the graphite epoxy composite material of the truss system, and b) an analytical and experimental evaluation of the damping capacity of simple adhesively bonded structural joints.

Report Outline

This report contains the results of the present investigation into the above-mentioned objectives. The project work was performed in the Sound and Vibration Laboratory of the Mechanical Engineering Department at Auburn University. The report is divided into seven major chapters. A general overview of damping— its characterization, and some mathematical models is presented in chapter 2. The various experimental and estimation techniques for the evaluation of damping are included in the same chapter. The advantages and disadvantages of each method are discussed. An improved forced vibration method developed during the course of the project is explained.

Chapter 3 covers the previous pertinent work on the evaluation of damping of composite materials. Work on the effects of moisture absorption and desorption, and temperature on the dynamic properties of composites is also reviewed. Recent developments in the study of dynamics of structural joints is also discussed.

Chapter 4 deals with the measurement of the damping of graphite epoxy material. It details the methodology and results of the damping measurements made on graphite epoxy tube and beam specimens under normal atmospheric conditions and in a vacuum. Experimental findings regarding the influence of moisture desorption and temperature (both high and low) on the damping capacity of the material are also discussed.

Chapter 5 is devoted to the study of damping of bonded structural joints. An analytical model has been developed to predict the natural frequencies, loss factors, and mode shapes of a bonded lap joint for free flexural vibration. The mathematical details, solution scheme, and numerical results are presented. Numerical results are compared with the experimental results obtained on graphite epoxy lap-jointed specimens. Some experimental results on the damping of graphite epoxy double-butt-jointed specimens are described in the same chapter. A summary of the project results, conclusions drawn, and some recommendations for future work are presented in chapters 6, 7 and 8.

II. DAMPING OVERVIEW

The term damping refers to any form of energy dissipation from a vibrating system. There are two main kinds of damping: 1) material damping and 2) system or structural damping. Material damping is the damping inherent in the material and is caused by a variety of physical mechanisms which depend on the material. System damping is due to energy dissipation in the total structure, i.e. in addition to the damping present in the material, it includes several non-material damping mechanisms such as, energy dissipation effects at joints, fasteners, and interfaces, acoustic radiation damping, and coulomb or dry friction damping, etc. A knowledge of the damping property of a structure is of primary importance in controlling its resonant response, and thus in prolonging its service life. Damping also plays a crucial role in the proper design of the system for vibratory loadings.

Characterization of Damping

A number of different units and notations have been proposed to express the damping parameter. The variety of combinations of energy dissipation mechanisms, the wide range of materials and testing techniques, the effects of joints and interfaces, and various different motivations for damping studies have led to different viewpoints towards damping and different mathematical models for its characterization[4-10]. Many different disciplines have been concerned with the damping research and each discipline, it appears, has its own favorite nomenclature. It is therefore essential to review at least some of the important damping representations in current use and to indicate the relationships between them.

Absolute Energy Units

In terms of the absolute energy units, which are applicable to both linear and non-linear materials, the damping energy dissipated in the specimen in a cycle per unit volume (U_{dV}) is a measure of the material damping. Thus the total damping energy U_D, is

$$U_D = \int_V U_{dV} dV, \tag{2.1}$$

where V is the volume. The usual unit of U_D is joule/cycle and of U_{dV}, joule/cm³-cycle.

The absolute energy dissipation is difficult to measure, in practice, in most cases. Hence relative energy units are more popular.

Relative Energy Units

Relative Energy Units, also applicable to both linear and non-linear materials are dimensionless ratios of damping energy to strain energy. Four different forms of relative units appear in the literature:

1\) The loss factor η is defined as the ratio of energy dissipated in a cycle to the maximum energy stored during that cycle. For a simple harmonic excitation, $f(t) = F \sin \omega t$, the response can be described as $x(t) = X \sin (\omega t + \phi)$, where ϕ is the phase angle between the force and the displacement. The energy dissipated D is equal to the work done in that cycle:

$$D = \int_0^{2\pi/\omega} f(t) \frac{dx(t)}{dt} dt \tag{2.2}$$

$$= \pi X F \sin\phi.$$

The strain energy U in the system is nothing but the energy supplied to the system, which is given by,

$$U = \frac{1}{T} \int_0^T f(t) \ x(t) \quad = \frac{1}{2} FX\cos\phi \ . \tag{2.3}$$

Therefore, from Equations (2.2) and (2.3), the loss factor is given by

$$\eta = \frac{D}{2\pi U} = \tan\phi. \tag{2.4}$$

2) <u>The quality factor Q</u> which is defined as the reciprocal of the loss factor η is also sometimes used as a measure of damping,

$$Q = \frac{1}{\eta} \ . \tag{2.5}$$

3) A most popular representation of damping is the <u>Damping Ratio</u> (ζ). It is the dimensionless ratio associated with a resonance frequency (modal frequency) and is defined by

$$\zeta = \frac{c}{c_c} \ , \tag{2.6}$$

where c is the viscous damping coefficient and c_c is the critical damping coefficient, for which the system will cease to oscillate when displaced from rest and released. The damping ratio ζ, often expressed as a percentage gives a quick visualization of the damping present in the system. Values of $\zeta < 1$ suggest that it is an underdamped system, $\zeta = 1$ represents a critically damped system, and $\zeta > 1$ represents an over-damped system. Throughout this report, the percent critical damping ratio ζ is adapted as the measure of damping.

4) <u>Complex Modulus approach</u> - In many polymer and composite materials, the Young's modulus(E) can be treated as a complex quantity, since there will be a phase difference between the stress and strain[10]. In this approach, we define the following relationship between stress σ and strain ϵ:

$$\sigma = E\epsilon + \alpha E \frac{\partial \epsilon}{\partial t}, \qquad (2.7)$$

where E is the Young's modulus and α is a constant. Assuming a time dependance of the form, $e^{i\omega t}$, we can write, $\sigma = \sigma_0 \; e^{i\omega t}$, and $\epsilon = \epsilon_0 \; e^{i\omega t}$. Then Equation (2.7) becomes

$$\sigma_0 = E\,(1 + i\omega\alpha)\,\epsilon_0 . \qquad (2.7a)$$

In Equation (2.7a), the term E $(1 + i\omega\alpha)$ can be treated as a complex modulus of the material, which is written in a more convenient form,

$$E^* = E' + i\,E'', \qquad (2.7b)$$

where $E' = E$, the real part is called the 'storage modulus', and $E'' = \omega\alpha E$, the imaginary part is called the 'loss modulus'. The tangent of the phase angle between the stress and strain is defined as loss tangent or loss factor.

$$\tan\phi = \eta = \frac{E''}{E'} . \qquad (2.8)$$

All of the above relative energy unit representations of damping are, however, related to one another by:

$$\eta = \tan\phi = 2\zeta = \frac{1}{Q} . \qquad (2.9)$$

It should be noted that Equation (2.9) is valid for the damping measured at a resonance frequency and it is assumed that $\zeta \ll 1$ (lightly damped systems).

Experimental Methods for Damping Measurement

There are several methods available for measuring the material damping or damping in general. The choice of the technique to be used depends on several factors such as whether the material has a small or large value of modulus of elasticity, a small or large value of damping, the frequency range of interest, temperature, stress state, size and shape of the specimen, specimen configuration and excitation, available instrumentation, etc. Comprehensive reviews of the basic experimental techniques, along with their relative merits and demerits, have been published by Plunkett [11], Bert and Clary [12], and Chu and Wang [13]. The different methods for the estimation of the damping ratio can be broadly classified as:

1) Time domain methods,
2) Frequency domain methods, and
3) Other special methods developed for testing viscoelastic materials.

Time Domain Methods

As the name implies, the system response data in the time domain are utilized in these methods for the estimation of the modal damping ratio. There are two such methods: a) Logarithmic decrement method, and b) Impulse response method. These are described in the following sections.

Logarithmic Decrement Method

This is also called the free-vibration decay method. This is one of the oldest techniques used for the estimation of the damping ratio. In this method, the free vibration decay (displacement amplitude history) of a system to a transient input (an impulse) is measured by a transducer and recorded by a recorder. From this decay curve, the logarithmic decrement δ, which is related to the damping ratio of the system is calculated. The theory behind this simple method is briefly outlined here. For a single degree of freedom system (Figure 1 (a)) the time response of the system due to a transient input can be expressed as

$$y(t) = A\, e^{-\zeta\omega_n t} \sin(\omega_d t + \phi), \tag{2.10}$$

where, A is a constant defined by the initial conditions, ζ = damping ratio, ω_n = undamped natural frequency, ω_d = damped natural frequency, ϕ = phase angle, and t = time. Equation (2.10) represents a decaying sinusoidal motion (Figure 1 (b)) and provided ζ is small, $\omega_d \approx \omega_n$ and if the sine term in Equation (2.10) is unity at some time t_o, then it will again be unity at times, $t_N = t_o + 2\pi N/\omega_d \approx t_o + 2\pi N/\omega_n$, where N is an integer number, N = 1,2,3 .... Thus, by examining Equation (2.10), we see that,

$$\frac{y(t_o)}{y(t_N)} = e^{N(2\pi\zeta)}. \tag{2.11}$$

By taking natural logarithms, we obtain the logarithmic decrement δ as:

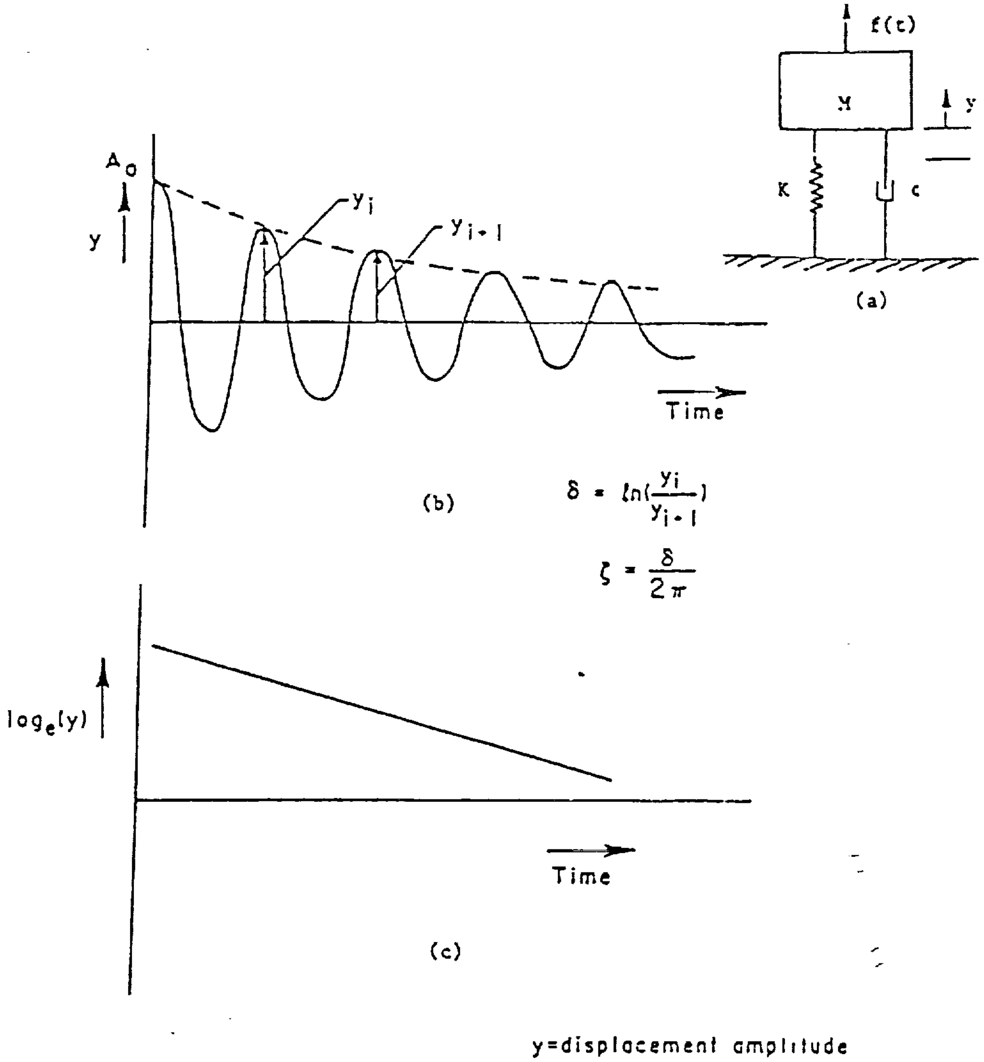

(a) A Single Degree of Freedom System
(b) Ideal Free Vibration Response when y is Plotted on a Linear Scale
(c) Ideal Free Vibration Response when y is Plotted on a Logarithmic Scale

Figure 1. Illustration of the Logarithmic Decrement Method

$$\delta = 2\pi\varsigma = \frac{1}{N} \ln \frac{y(t_o)}{y(t_N)} . \qquad (2.12)$$

Use of Equation (2.12) provides a convenient way of measuring the damping ratio ς. In this method, the specimen is clamped in a cantilever position, then "plucked" and allowed to vibrate freely. The decaying motion may be measured by strain gauges, accelerometers or optical sensors. Crawley and his co-workers [14,15] have utilized strain gages to test their specimen in free-fall in a simulated space environment. This was done to avoid the extraneous energy losses due to supports and acoustic radiation.

If the system has many resonances, this approach can still be used. One way is to use a band-pass filter to filter out the undesired frequency content of the signal prior to displaying the signal in the time domain on the recording system. An alternative method is to 'tune' the desired mode of vibration by attaching several shakers to the system and by using force appropriation techniques described by Asher [16]. When the system is vibrating in a desired mode, the shakers are simultaneously cut-off, and the resulting decay for that mode is measured and the damping ratio is calculated by using Equation (2.12). This approach, however, requires elaborate instrumentation and hence has been used only for testing large aircraft structures.

In the logarithmic decrement method, it is assumed that the damping ratio is independent of the displacement amplitude. A modification of the decay method can be used very easily by passing the time response through a log amplifier. The decay curve will then be a straight line and the slope of this line is a measure of the damping [Figure 1(c)]. An alternative approach is to use a least-squares curve-fitting procedure for the measured decay curve to obtain an accurate estimate of the damping ratio. The theory behind this curve-fitting method is given in [17]. A computer simulation was carried out in reference [17] in order to compare the decay method with the least squares curve-fitting method for the estimation of the damping ratio. It was shown that the curve-fitting method is more accurate than the decay method for the conditions most frequently encountered in practice. The optimum number of data points for which the best estimate of the damping ratio is obtained was found to be about twenty.

Some other methods of measurement associated with the decay of free vibration of mechanical systems have been noted in the literature[4,18]. One such approach is the use of the time-averaged, squared response y^2, in decibels. If we define the displacement level L_y to be:

$$L_y = 10 \log_{10}(y^2/y^2_{ref}), \text{ dB} \qquad (2.13)$$

where, y is the displacement amplitude and y_{ref} is a reference displacement amplitude, then it is easy to show, by substituting for y from Equation (2.10), that,

$$\frac{-dL_y}{dt} = \frac{-d}{dt}\left[20 \text{ Log}_{10} \left(Ae^{-\zeta\omega_n t}/y_{ref}\right)\right], \qquad (2.14)$$

and the Decay rate Δ_t is given by:

$$\Delta_t = \frac{-dL_y}{dt} = - [20 \ \mathrm{Log}_{10}(e)] \ [-\zeta\omega_n] = 8.69\zeta\omega_n \ . \qquad (2.15)$$

Another way of estimating the damping ratio of a system is to measure the reverberation time of the vibration decay in the system. The reverberation time T_R is defined as the time in which the displacement level is reduced by 60 dB. It is seen from Equation (2.15) that this value is given by:

$$T_R = 6.90/\zeta\omega_n = 1.10/\zeta f_n. \qquad (2.16)$$

(This is easily shown by letting $dt = T_R$ and $dL_y = -60$ dB, and $\omega_n = 2\pi f_n$ in Equation (2.15).)

Impulse Response Method

This method is essentially a forced vibration method. With the advent of modern digital FFT analyzers, it is now possible to obtain the frequency response of a system to any physically realizable excitation, and the data can be processed either in the time domain or in the frequency domain within a fraction of a second. The frequency response $H(\omega)$ of a system is the ratio of system response to an input excitation in the frequency domain. The impulse response $h(t)$ is the time domain equivalent of the frequency response. It can be obtained very easily by an inverse Fourier transformation of the frequency response function (FRF).

A typical experimental set-up for measuring the impulse response function is shown in Figure 2. For a single degree of freedom system, the unit impulse response (i.e. the system's response to a unit force) is identical to that of Equation (2.10) and it can be easily recognized that the exponential decay is also a straight line when the displacement amplitude is plotted on a logarithmic scale. Hence, the techniques described in the previous section can be used to estimate the damping ratio. The decay rate method discussed previously is most commonly used in conjunction with the impulse response method.

For a multi-degree of freedom system, the impulse response function is more complicated. It can be written in terms of the modal parameters as [19,20]:

$$h(t) = \sum_{i=1}^{n} |R_i| e^{-\zeta_i \omega_i t} \sin(\omega_i t + \alpha_i) \ , \qquad (2.17)$$

where, n = number of modes

R_i = residue,

α_i = angle of residue,

ζ_i = modal damping ratio, and

ω_i = modal frequency.

The subscript i stands for the ith mode of vibration. The residue R_i is related to the mode shape of the ith mode. Brown et al. [20] have described a curve-fitting technique called the complex-exponential algorithm, to extract the modal damping ratios and other modal parameters from the measured impulse response data using Equation (2.17). This technique has the disadvantage that it requires very elaborate data reduction equipment and generally gives an

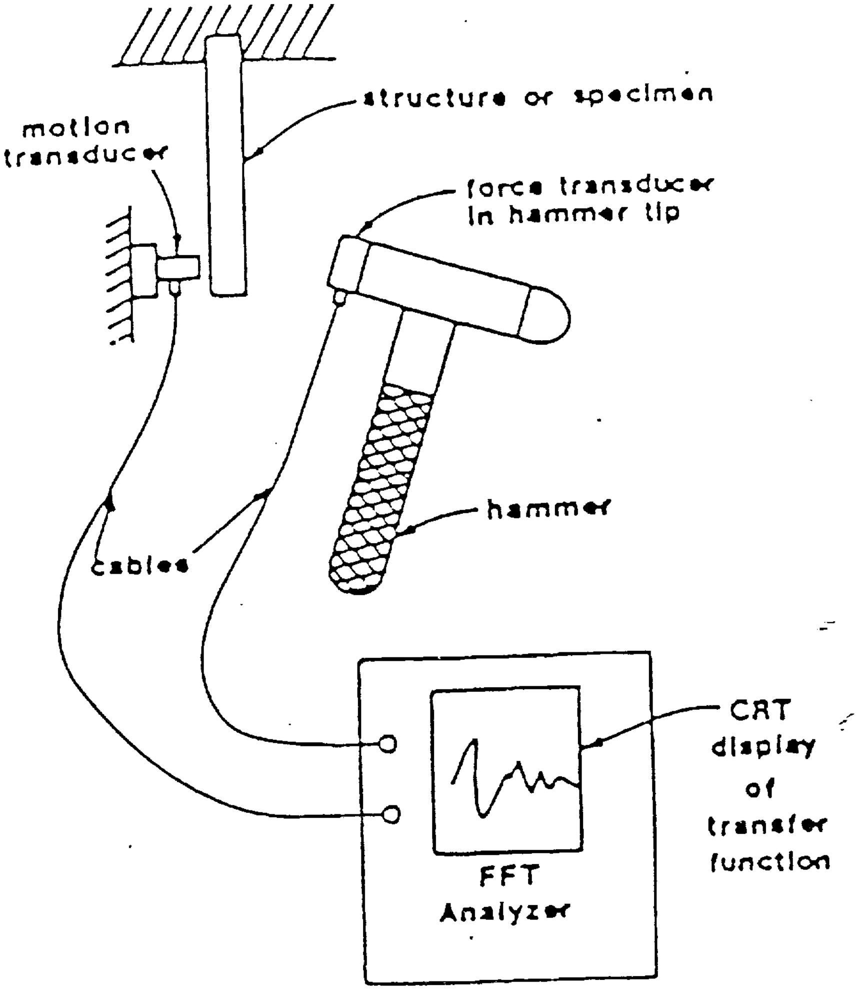

Figure 2. A Typical Experimental Set-up for the Measurement of Impulse Response Function

overestimation of the damping values because of the damping induced by the exponential window in the FFT analyzer. This method is, however, the only powerful technique available for measuring the damping ratio of systems with very high modal density and modal interference. Many commercial modal analysis software packages have incorporated this technique as one of the standard curve-fitting routines for extracting the modal parameters.

Frequency Domain Methods

Several techniques are available for estimating the damping from the system response data in the frequency domain. Usually, in all these methods, a simple single degree of freedom system model with either a viscous or a hysteretic type of damping is assumed. A detailed description of viscous and hysteretic damping models can be found in [10]. The following is a broad classification of the frequency domain techniques for the estimation of the damping ratio:

1) Resonant forced vibration methods,
2) Non-resonant forced vibration methods and,
3) Input-power method.

Resonant Forced Vibration Methods

As in the time domain methods, the damping ratio is assumed to be independent of the displacement amplitude, but dependent on the resonance frequency of vibration.

If the damped simple system in Figure 1 (a) is excited by a simple harmonic force of amplitude | F | at angular frequency $\omega = 2\pi f$, the frequency response function is given by[18]:

$$\frac{Y(\omega)}{F(\omega)} = \frac{1}{(K-M\omega^2) + ic\omega} = \frac{1/K}{(1-r^2) + i(2\zeta r)}. \qquad (2.18)$$

Here $r = \omega/\omega_n$ is the frequency ratio, and $i = (-1)^{1/2}$. The ratio Y/F is called the frequency response function (FRF) which in this case is the receptance or the displacement admittance function. In practice, transient, random, and sinusoidal excitations can all be used to obtain the FRF function. When random excitation is used, the FRF is estimated by power spectrum averaging. In this case the FRF is defined as the ratio of the cross-spectrum between the force and the displacement signals to the auto-spectrum of the force signal. The random excitation technique is normally used to obtain more accurate results than the other excitation methods if noise is present in the measurement process. A survey of the different excitation techniques, their relative merits and demerits for modal analysis of structures can be found in references [21,22].

Equation (2.18) forms the basis for many of the damping estimation methods as follows:

(a) Half-power Points Method

The magnitude of the receptance function of Equation (2.18) can be expressed as:

$$\left|\frac{Y}{F}\right|_{mag} = \frac{(1/K)}{((1-r^2)^2 + (2\zeta r)^2)^{1/2}}. \qquad (2.19)$$

Provided the damping is small, $\varsigma^2 \ll 1$, which is the situation in most engineering applications, then, when the forcing frequency ω equals the undamped natural frequency ω_n, the displacement admittance is nearly maximum. The dynamic magnification factor, DMF = | Y | / | F | / K for this situation when $\omega = \omega_n$ (resonance) is thus, DMF = $1/2\varsigma = Q$ (where Q is the quality factor).

Defining the half-power points as the points at which

| Y | / | F | / K has fallen to $\sqrt{2}$ of its value at resonance (see Figure 3(a), we obtain the two values of angular frequency ω_1, and ω_2 for this to occur from

$$\frac{1}{2\varsigma\sqrt{2}} = \frac{1}{\{(1-r^2)^2 + (2\varsigma r)^2\}^{1/2}}\ , \tag{2.20}$$

and assuming $\varsigma^2 \ll 1$, we obtain from the quadratic solution:

$$r_{1,2} = \frac{\omega_{1,2}}{\omega_n} = 1 \pm \varsigma. \tag{2.21}$$

Thus, the damping ratio ς can be obtained from the half power bandwidth $\Delta\omega = \omega_2 - \omega_1$ as

$$\varsigma = \frac{\omega_2 - \omega_1}{2\omega_n}\ . \tag{2.22}$$

Thus, by determining the two frequencies ω_1 and ω_2, at which the response is $1/\sqrt{2}$ of the value at the resonance frequency ω_n, the damping ratio ς can quickly be determined using Equation (2.22). The amplitude ratio of $1/\sqrt{2}$ corresponds to reduction of amplitude measured

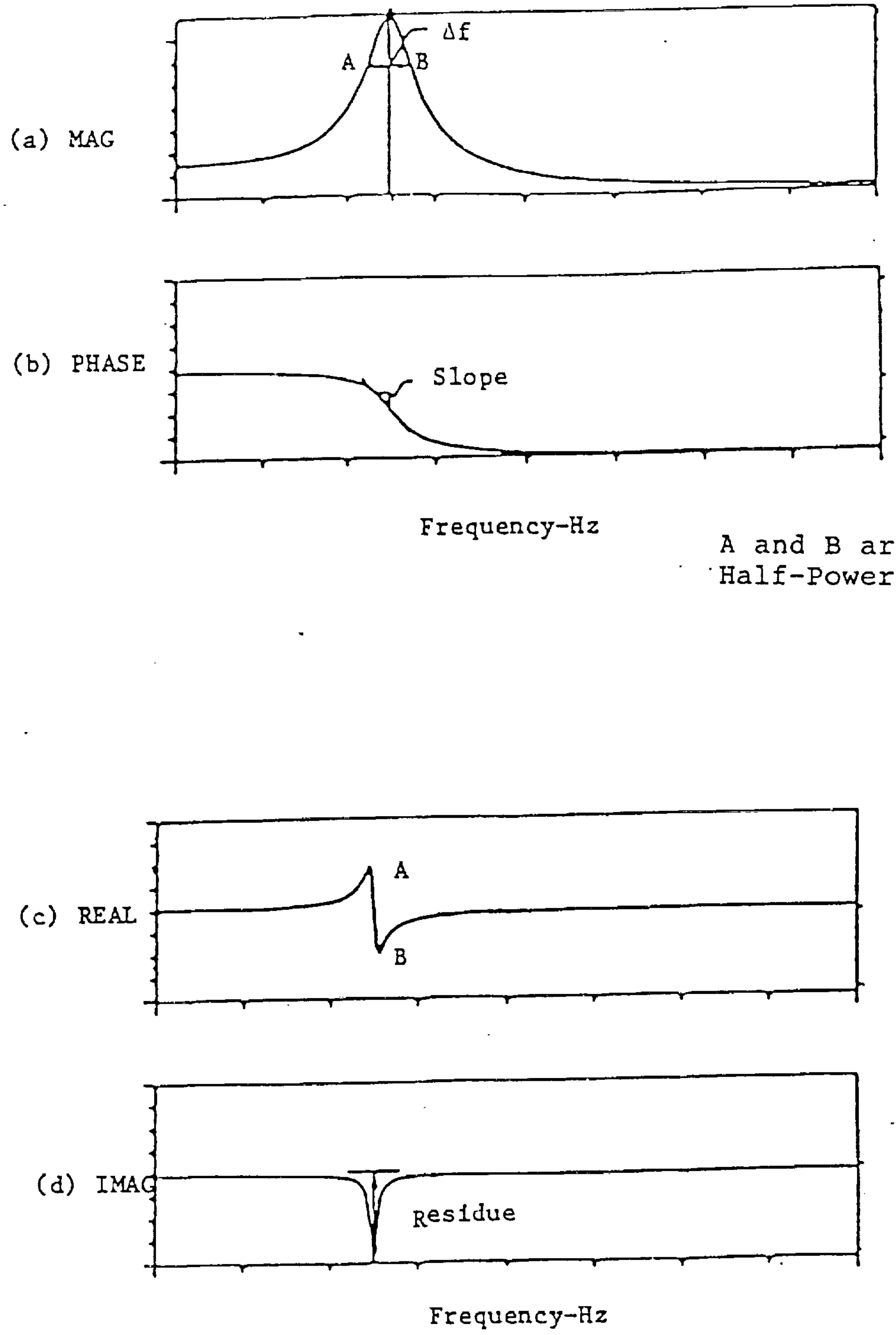

A and B are the Half-Power points

Figure 3. Frequency Response of a Single Degree of Freedom System-(a) Magnitude, (b) Phase, (c) Real Part, (d) Imaginary Part.

in decibels of 20 $\mathrm{Log}_{10}(1/\sqrt{2}) = -3$ dB. Thus a measurement associated with an amplitude ratio of $1/\sqrt{2}$ is frequently referred to a "3 dB bandwidth." If the system has many higher resonance frequencies, then the same procedure can still be used by measuring the half-power bandwidth of each resonance peak in the curve. This approach can be used provided that ς is not too large and that the resonance peaks are fairly sharp and can be separated in the frequency domain.

(b) Damping from Real and Imaginary Parts of Receptance (co-quad plots)

The real and imaginary parts of Equation (2.19) shown in Figure 3 (c) and 3 (d) are

$$\mathrm{Re}\left(\frac{Y}{F}\right) = \frac{(1-r^2)^2/K}{(1-r^2)^2 + (2\varsigma r)^2}\text{, and} \tag{2.23}$$

$$\mathrm{Im}\left(\frac{Y}{F}\right) = \frac{-2\varsigma r/K}{(1-r^2)^2 + (2\varsigma r)^2}. \tag{2.24}$$

The real part will be zero at a resonance (when $r = 1$). The damping ratio can be estimated from the relation:

$$\varsigma = \frac{\omega_2^2 - \omega_1^2}{2(\omega_2^2 + \omega_1^2)}, \tag{2.25}$$

where ω_1 and ω_2 are the frequencies on each side of ω_n where the magnitude of the real part reaches a maximum.

From the imaginary plot, the resonance is located at the point where Im(Y/F) has a peak. The half-power points correspond to frequencies at which the quadrature response (imaginary part) has half of the maximum amplitudes. Thus Equation (2.22) can once again be used for calculating the damping ratio.

(c) Damping Estimation from the Phase Angle Plot

Estimation of the damping ratio from the phase angle plot is well described by Pendered and Bishop [23]. The equation for calculating the phase angle is,

$$\tan\phi = \frac{-2\zeta r}{(1-r^2)} \cdot \qquad (2.26)$$

A typical variation of the phase angle with frequency is shown in Figure 3 (b). At a resonance, theoretically, the phase angle between force and displacement should be -90°. The half-power points, A and B correspond to phase angles of -45° and -135° respectively, thus, the damping ratio can be evaluated using Equation (2.22). In practice, since it is often very difficult to measure the half power points from the phase angle curve, an alternate approach has been suggested. This involves a measure of the slope of the tangent to the curve at the inflection point, $\partial^2\phi/\partial\omega^2 = 0$. The damping ratio can then be calculated from the relation:

$$\zeta = \frac{1}{\omega_n(\text{slope at } \omega_n)} = \frac{1}{\omega_n\left(\frac{\partial\phi}{\partial\omega}\right)_{\omega = \omega_n}} \cdot \qquad (2.27)$$

Although the phase method has an advantage in the sense that, the determination of the natural frequency does not depend on the accurate location of a 'peak', it has not, however, been very popular, since, even now in practice, it is very difficult accurately to measure the phase angles.

(d) Vector Diagram Method (Kennedy-Pancu Method)

This method was originally developed by Kennedy and Pancu [24]. If the complex receptance function of Equation (2.18) is plotted on an Argand plane, which is a plot of real part vs. imaginary part on a x-y coordinate system, the resulting curve would be a circle as shown in Figure 4. In fact, this can be proved very easily by considering Equations (2.23) and (2.24). By a simple mathematical manipulation, it can be shown that

$$\{\mathrm{Re}(Y/F)\}^2 + \{\mathrm{Im}(Y/F) + 1/(4\zeta r)\}^2 = 1/(4\zeta r)^2 \;, \qquad (2.28)$$

which represents a circle with center at $(0, 1/(2\zeta r))$, and having a radius of $1/(2\zeta r)$. From the plot, Kennedy and Pancu noted that: 1) at resonance, the displacement vector lies on the imaginary axis and hence, is 90 degrees out of phase with the applied force, 2) the change in arc length(s) along the curve per unit change in frequency $(ds/d\omega)$ is a maximum at resonance, and 3) the diameter of the circle is inversely proportional to the damping ratio.

As in the phase angle method, here also two approaches are used to estimate the damping ratio. One approach, of course, is to use the half-power point Equation (2.22). The half-power point frequencies can be determined readily from the Argand Plot by drawing a line parallel to the real axis through the center of the circle; the points of intersection of this line with the circle are the half power point frequencies. These points also correspond to frequencies ω_1, and ω_2 at $\pm 90^0$ angle with respect to the damped natural frequency. The resonance frequency is the point on the circle farthest from the real axis (where the imaginary part is zero). An alternate approach to determine the resonance frequency is from arc length measurements; the resonance frequency corresponds to a point of maximum rate of change of arc length with frequency. A mathematical analysis for this is presented in many references [25-28]. Alternatively, the damping ratio, can be estimated by knowing the rate of change of phase with frequency, evaluated at resonance (see Equation 2.27).

In applying the Kennedy-Pancu method, the normal procedure is to fit the 'best circle' through the measured data points around a resonance. This is called the 'circle fit' procedure. For a multi-degree of freedom system, the complex receptance can be viewed as a summation of the complex receptances of several single degree of freedom systems as in Equation (2.18). A typical Kennedy-Pancu plot for a two-degree of freedom system is shown in Figure 4 (b). It is evident that there are two resonance frequencies because of the presence of two circular arcs. The normal procedure for such systems is to fit a circle to each of the loops separately as a single degree of freedom system. Notice that the vector diagram of systems with many degrees of freedom are not circles, but curves with many loops, usually one for each resonance. Woodcock [29] has extended the Kennedy-Pancu method to study systems with many degrees of freedom. It is reported in the literature that the circle-fitting procedure yields better estimates of modal parameters than the other methods in the presence of closely spaced modes. But, the choice of data points utilized in the circle fit gives different answers and the best answer becomes a matter of judgement [20].

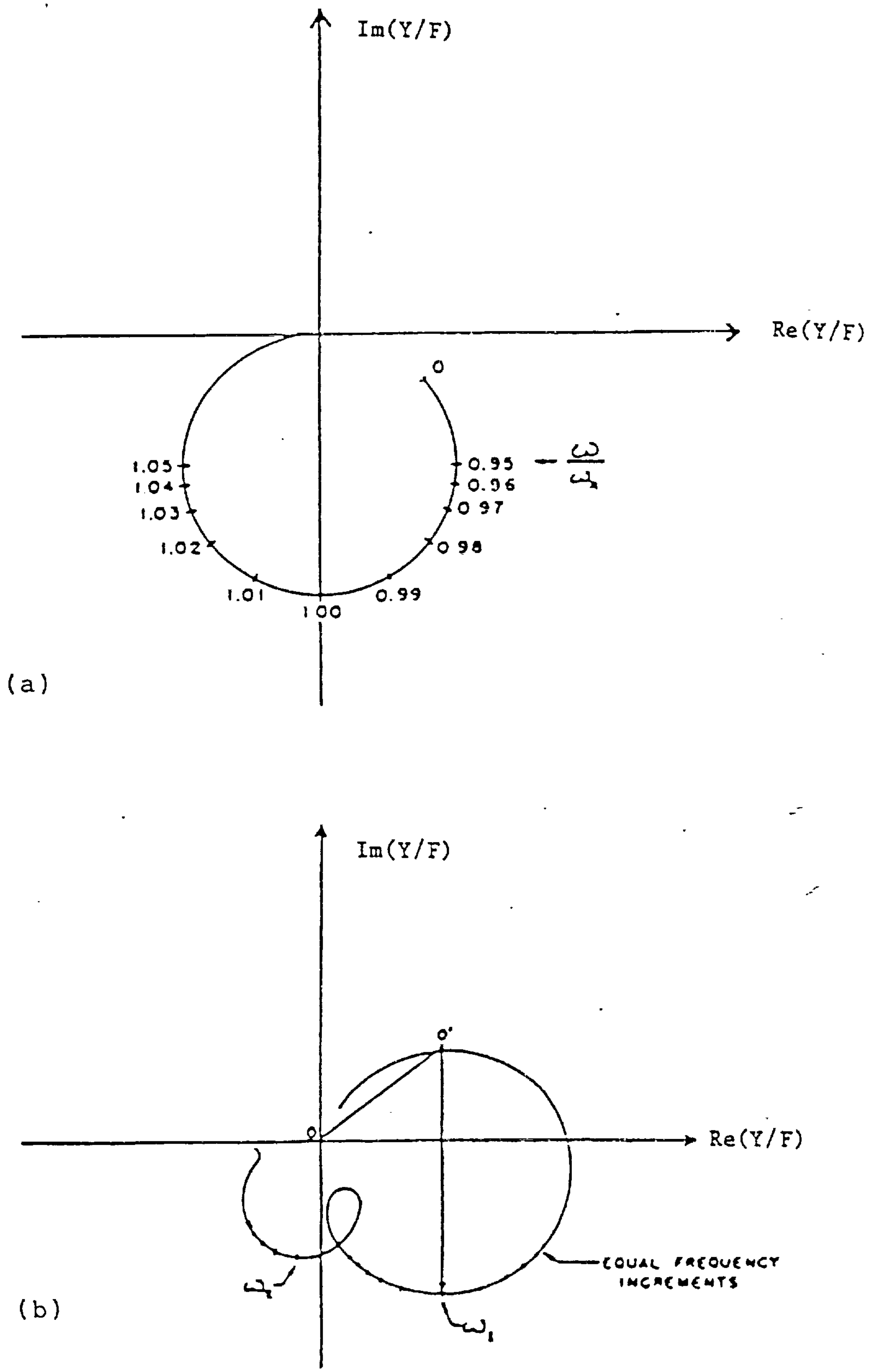

Figure 4. Nyquist Plots of Single and Two Degree of Freedom Systems

The principal assumptions made in all the methods discussed so far for the estimation of the damping ratio are: 1) the system is linear, 2) the system possesses very light damping, and 3) the modes of the system are well separated. Each method has its own advantages and disadvantages. In general, most of the above methods have a major drawback in that they just use two or three points on the response curve for the estimation of the damping ratio. Hence, the accuracy of the estimated damping ratio depends on how well the two or three data points are chosen. In practice, it is usually difficult accurately to locate the resonance frequency and the half-power points. Furthermore, the frequency resolution of the analyzing instrument has a restriction on the value of the damping ratio that can be estimated. Hence, recognizing the need for a better method for damping ratio estimation, the following improved forced vibration method has been developed as a part of this research project.

Improved Resonant Forced-Vibration Method

The method consists of fitting a 'best curve' for the measured receptance data using an iterative least-squares error criterion. The damping ratio and the undamped natural frequency are then, computed from the coefficients of the rational fraction polynomial determined from the curve-fitting technique. Any of the three functions of the receptance namely, the magnitude, the real part, or the imaginary part can be used in the method. The theory behind this method is as follows.

The frequency response function used in the analysis is the receptance function (displacement/force) of a single degree of freedom system, obtained from a single point excitation. Either a random input excitation (white noise) or a swept sine excitation can be used. The receptance function can easily be measured in practice by an impedance head and a dual channel signal analyzer. In the following analysis, the equations of motion of a multi degree of freedom system with proportional damping are used. These are chosen to illustrate the fact that the method developed here can also be used for a system response containing several distinct modes by fitting each of the modes separately as a single degree of freedom system.

For a general multi-degree of freedom system with proportional damping the equation of motion in matrix form is:

$$M\ddot{x} + R\dot{x} + Kx = P(t) \ , \qquad (2.29)$$

where, M = mass matrix, nxn,

R = damping matrix, nxn,

K = stiffness matrix, nxn,

$\ddot{x}$, $\dot{x}$, x = acceleration, velocity and displacement vector, respectively, nx1,

$P(t)$ = force vector, nx1,

n = number of degrees of freedom.

If the normal mode shape of the system without damping is $[\phi]_{nxn}$, then applying the following transforms:

$$x = [\phi]q, \ \dot{x} = [\phi]\dot{q}, \text{ and } \ddot{x} = [\phi]\ddot{q}$$

and the orthogonality conditions:

$$[\phi]_j{}^T M[\phi]_i = 0, \quad [\phi]_i{}^T M[\phi]_i = M_G .$$

$$[\phi]_j{}^T K[\phi]_i = 0, \quad [\phi]_i{}^T K[\phi]_i = K_G ,$$

where M_G and K_G represent the decoupled (diagonal) mass and stiffness matrices of the system respectively. Pre-multiplying both sides of Equation (2.29) with $[\phi]^T$ and applying the above transforms the following equation is obtained:

$$[\phi]^T M[\phi]\ddot{q} + [\phi]^T R[\phi]\dot{q} + [\phi]^T K[\phi]q = [\phi]^T P(t) \ . \qquad (2.30)$$

Assuming that the damping is viscous, and that the damping matrix is proportional to mass matrix, $r_r = 2\zeta_r\omega_{nr}M_r$, a diagonal matrix equation from Equation (2.30) is obtained:

$$M_G\ddot{q} + M_G[{}^{\backslash}2\zeta_r\omega_{nr\backslash}]\dot{q} + K_G q = P_G(t) \ , \qquad (2.31)$$

where, $P_G(t) = [\phi]^T P(t)$. If $P_G(t) = P_G e^{i\omega t}$, then the steady state solution of Equation (2.31) can be obtained as:

$$q = Qe^{i\omega t},$$

where, $$Q_r = \frac{P_{Gr}}{M_{Gr}[\omega_{nr}^2 + i2\zeta_r\omega_{nr}\omega - \omega^2]}, \ r = 1, 2, \ldots n.$$

Since $$x = [\phi]q = q_o e^{i\omega t}$$

$$q_o = \sum_{r=1}^{n} \frac{\{\phi_r\}^T \{P\} \{\phi_r\}}{M_{Gr}[\omega_{nr}^2 + i2\zeta_r\omega_{nr}\omega - \omega^2]} \ . \qquad (2.32)$$

If only one force acts on the j-th point and the response is measured at the same point, then the r-order driving point displacement admittance is obtained as follows:

$$M_{Dr} = \frac{\phi_r^2}{M_{Gr}[\omega_{nr}^2 + i2\varsigma\omega_{nr}\omega - \omega^2]} \,. \tag{2.33}$$

The magnitude, the real part and the imaginary part of the receptance for the r-th mode are, respectively,

$$|M_{Dr}|^2 = \frac{\phi_r^2 \,/(2\pi)^4}{M_{Gr}[f_{nr}^4 + 2(\varsigma^2 - 1)f_{nr}^2 f^2 + f^4]} \,, \tag{2.34}$$

$$Re(M_{Dr}) = \frac{\phi_r^2\,(f_{nr}^2 - f^2)/(2\pi)^2}{M_{Gr}[f_{nr}^4 + 2(2\varsigma^2 - 1)f_{nr}^2 f^2 + f^4]} , \tag{2.35}$$

$$Im(M_{Dr}) = \frac{-2\phi_r^2\,\varsigma\, f_{nr} f \,/(2\pi)^2}{M_{Gr}[f_{nr}^4 + 2(2\varsigma^2 - 1)f_{nr}^2 f^2 + f^4]} , \tag{2.36}$$

where, f_{nr} is the excitation frequency, Hz. Equations (2.34) through (2.36) can be expressed by rational functions:

$$|M_{Dr}|^2 = \frac{A_3}{[A_1 + A_2 f^2 + f^4]} \,, \tag{2.37}$$

$$Re(M_{Dr}) = \frac{A_4(A_1)^{1/2} - A_4 f^2}{A_1 + A_2 f^2 + f^4} \,, \tag{2.38}$$

$$Im(M_{Dr}) = \frac{A_5 f}{A_1 + A_2 f^2 + f^4} , \tag{2.39}$$

where, $A_1 = f_{nr}^4$, $A_2 = 2\ (2\varsigma^2 - 1)\ f_{nr}^2$, $A_3 = \phi_r^2 \,/\, M_{Gr}(2\pi)^4$, (2.40)

$A_4 = \phi_r^2 / M_{Gr}(2\pi)^2$, and $A_5 = -\phi_r^2 \, 2\varsigma f_{nr} / M_{Gr}(2\pi)^2$.

From the coefficients A_1 and A_2, the natural frequency and the damping ratio can be obtained:

$$f_n = A_1^{1/4}, \tag{2.41}$$

$$\varsigma = \{ \frac{1}{2} [\frac{A_2}{2f_n^2} + 1] \}^{1/2}. \tag{2.42}$$

Using the measured data for the magnitude or the real part or the imaginary part of the receptance and the frequencies in the range of the bandwidth of the half-power points, these data can be fitted to the corresponding equations given above. Using the magnitude with Equation (2.37) for example, the curve-fitting procedure is as follows:

Let $y = |M_{Dr}^2(f)|$, then the estimate of $\hat{y}$ is:

$$\hat{y} = \frac{B_1}{1 + B_2 f^2 + B_3 f^4}, \tag{2.43}$$

where, $B_1 = \frac{A_3}{A_1}$, $B_2 = \frac{A_2}{A_1}$, and $B_3 = \frac{1}{A_1}$. Equation (2.43) can be written as, $B_1 - \hat{y}\,(1 + B_2 f^2 + B_3 f^4) = 0$. The residual r is:

$$r = \hat{y} - y = B_1 - Y(B_2 f^2 + B_3 f^4) - y \tag{2.44}$$

$Y = r+y$. For each experimental point, corresponding to a $y_i - f_i$ pair, the residual is

$$r_i = B_1 - Y_i(B_2 f_i^2 + B_3 f_i^4) - y_i. \tag{2.45}$$

The least-squares curve-fitting criterion requires that the sum S of the squares of residuals for N points be a minimum, that is

$$S = \sum_{i=1}^{N} r_i^2 = \sum_{i=1}^{N} [B_1 - Y_i(B_2 f_i^2 + B_3 f_i^4) - y_i]^2 = \text{min.} \qquad (2.46)$$

Setting the partial derivatives of Equation (2.46) with respect to the coefficient B_1, B_2 and B_3 to be zero, the matrix equation is obtained:

$$\begin{bmatrix} N & -\Sigma Y_i f_i^2 & -\Sigma Y_i f_i^4 \\ \Sigma Y_i f_i^2 & -\Sigma Y_i^2 f_i^4 & -\Sigma Y_i^2 f_i^6 \\ \Sigma Y_i f_i{}^4 & -\Sigma Y_i^2 f_i^6 & -\Sigma Y_i^2 f_i^8 \end{bmatrix} \begin{bmatrix} B_1 \\ B_2 \\ B_3 \end{bmatrix} = \begin{bmatrix} \Sigma Y_i \\ \Sigma y_i Y_i f_i^2 \\ \Sigma y_i Y_i f_i^4 \end{bmatrix} \qquad (2.47)$$

Equation (2.47) can be solved for the constants, B_1, B_2 and B_3 by an iterative method. For the first iteration, it is assumed that $Y_i = y_i$, then, $Y_i(L) = y_i + r_i(L-1)$, where L is the iteration time. Then the calculations are repeated till the desired convergence criterion is obtained. After at most 10 iterations, the coefficients will converge to an accuracy of about 10^{-6}. Then the undamped natural frequency and the damping ratio can then be obtained from Equations (2.41) and (2.42) respectively. A computer program has been written to carry out the iteration using all the three functions, namely the magnitude, the real part and the imaginary part of the receptance data.

The residual for Equation (2.43) can be defined in an alternative form:

$$r_i = y_i(A_1 + A_2f^2 + f^4) - A_3, \tag{2.48}$$

then the matrix equation for the least squares curve-fitting will be simpler than Equation (2.47) and this procedure does not require any iteration for its solution. Hence this is even a simpler method than the iterative least square method suggested above. Similar expressions can be developed using the real and imaginary parts of the receptance.

The major advantage of this method is that, the entire data near a resonance are used for the estimation of the damping ratio, as opposed to three points in the half-power points method. Thus, a more accurate estimate of the damping ratio can be obtained. Furthermore, the undamped natural frequency obtained from the least-squares computation is used in the calculation of the damping ratio. Also, this method is not limited to systems with small damping and the frequency resolution of the analyzer does not influence the accuracy of the method to some extent. Since this method uses fewer data near a resonance as compared to other complex curve-fitting techniques [30,31] a smaller memory is required in the computer and a higher data-reduction speed can be achieved. This method has been used in the present investigation for the measurement of the damping ratio of the graphite epoxy composite material. Details of its application to the present project are discussed in the forthcoming chapters. Some results showing the comparison between the curve-fitting technique and the half-power points method is included in Appendix A.

Non-Resonant Forced Vibration Methods

This method has been mostly applied in the measurement of the complex Young's modulus of polymers and viscoelastic materials. The loss factor (2ζ) is calculated from the real and imaginary part of the modulus by use of the equation $\eta = E''/E'$, where E' and E'' are the real and imaginary parts of the complex dynamic modulus respectively. The method can be best illustrated by considering the equation of motion for a single degree of freedom system using the complex modulus approach. For many composite materials, the force and displacement cycles will be out-of-phase by ϕ, so if F_0 and y_0 are the force and displacement amplitudes respectively, then

$$M\ddot{y} + (K' + iK'')\,y = F_0\,e^{i(\omega t + \phi)}, \tag{2.49}$$

where ω is the angular frequency.

Let $y = y_0\,e^{i\omega t}$, then Equation (2.49) can be written as:

$$-M\omega^2 + K' = (F_0/y_0)\cos\phi, \text{ and} \tag{2.50}$$

$$K'' = (F_0/y_0)\sin\phi\ . \tag{2.51}$$

For a very small sample, operating at low frequencies (stiffness-controlled region), the inertia term of Equation(2.50) is usually neglected. Further, the stiffness K of the beam specimen is related to the modulus E in the form $K = EA/t$, where, A is the area of cross section and t the thickness of the sample. Hence, from Equations (2.50) and (2.51), the damping ratio can be evaluated as:

$$\zeta = K''/K' = 1/2\tan\phi. \tag{2.52}$$

Hence the forced non-resonance method relies on the measurement of the phase angle between the force and displacement signals at a particular frequency ω, thus, it can be used as an indirect method for obtaining the damping as a function of frequency. This method, however, has a major drawback in that it can be used only on very small specimens and in the low frequency region, since the effect of inertia is neglected in the method. This method has been adapted for the measurement of the complex modulus of polymers and composites in many commercially available instruments like the DMTA (Dynamic Mechanical Thermal Analyzer) [32,33].

In a typical DMTA test arrangement, the displacement is applied via a loading stage attached to the table of an electromagnetic vibrator. The displacement is measured usually by a non-contacting magnetic transducer. The force is measured by a force transducer attached behind the specimen. The specimen is mounted horizontally within a controlled temperature enclosure in a single cantilever or dual-cantilever. A typical sample used in this arrangement is about 1 mm thick, 6 mm wide, and 28 mm long, and the frequency of excitation is limited to below 90 Hz.

The advantage of this method lies in its ability to study the dependence of the dynamic properties upon frequency, strain amplitude and temperature. Materials with a modulus greater than 10 GN/m^2 cannot easily be tested by this method. For the measurement of the damping the phase angle must be measured accurately. For phase angles less than 1 degree it is not possible to measure them very accurately. But larger values of phase angles can be measured accurately. The method therefore is not good for measuring small values of damping, but is ideally suited for measuring large damping values.

The hysteresis loop approach is another widely used non-resonance forced vibration method. Its theoretical basis is explained in detail by Lazan [2]. This method enables the measurement of very low material damping particularly in metals. It is limited, however, to the very low loading frequencies that are usually achievable in material testing machines.

Input Power Method

The theory for this method is developed from a consideration of the energy balance in the structure. If a damped mass-spring single degree-of-freedom system (Figure 1 (a)), is excited by a force F at a sinusoidal frequency ω, then the dissipated power Π_{diss} is proportional to the product of damping force F_d and velocity:

$$\Pi_{diss/cycle} = \int F_d \, dv = \int_0^{2\pi/\omega} F_d \, v \, dt = \pi c \omega v_0^2 \qquad (2.53)$$

where v_0 is the velocity amplitude, and c is the viscous damping coefficient.

In steady state conditions, the power supplied Π_{in} from a shaker must be equal to the power dissipated. Thus if Π_{in} can be measured and $\Pi_{in} = \Pi_{diss}$ is assumed, then ζ can easily be calculated from Equation (2.53). The input power can easily be measured using an impedance head. If a simple harmonic force of angular frequency ω and amplitude F_o is applied, then the time-averaged input power is

$$\Pi_{in} = v_o F_o \cos\beta, \tag{2.54}$$

where β is the phase angle between the force and velocity. Fahy [34] has discussed the case of input power measurement for random excitation. Nakayama and Crocker [35] have made extensive measurements of power supplied to structures and determined the structural damping from such measurements. According to Nakayama and Crocker, the input power for a random excitation with a time delay between the force and acceleration signals is given by:

$$\Pi_{in} = \frac{-1}{2\pi} \sum_{K=1}^{N/2} \{C_{Fa}(f)\sin\Delta\phi_k + Q_{Fa}(f_k)\cos\Delta\phi_k\} \cdot \ln\left[\frac{f_k + \Delta f/2}{f_k - \Delta f/2}\right], \tag{2.55}$$

where, Δf = frequency resolution of the analyzer,

N = number of data points in the time domain (Block size).

$C_{Fa}(f_k)$ and $Q_{Fa}(f_k)$ are the real and imaginary parts of the cross spectrum between force and acceleration respectively at frequency f_k. $\Delta\phi_k$= phase lag between acceleration and force signals. The band-limited input power can be obtained from Equation (2.55) by a simple averaging procedure. Structures such as panels have many resonance frequencies, and the normal procedure, then, is to measure the space-averaged mean square velocity over the structure: $\langle v^2 \rangle_{s,t}$. The dissipative loss factor $\eta = 2\zeta$ is then obtained as [36]:

$$\eta = \frac{\Pi_{in}}{M\langle v^2 \rangle 2\pi f}, \tag{2.56}$$

where M is the mass of the structure. The input power method has been used mainly in conjunction with an approach called the Statistical Energy Analysis of Structures (SEA)[36]. Cremer, Heckl and Ungar [37] have developed an expression for the loss factor based on the modal density (number of modes in a frequency band) for a broad band random excitation. Clarkson and his co-workers [38-40] have used these equations to obtain the modal densities and frequency-averaged loss factors of plates and shells. The frequency-averaged loss factor results they obtained compared well with the results from the logarithmic decrement method. According to their experience, at least five natural frequencies should be present within the analysis band and the damping should be small for the results to hold good.

The input power method is only an approximate method capable of yielding frequency-averaged loss factors.

Other Methods

Several other methods for measuring the damping ratio have been developed specifically for viscoelastic materials. Some of the important techniques are briefly reviewed here. The <u>Oberst bar technique</u> - also called the Bruel & Kjaer cantilever beam method, was developed by Oberst [41] and is the basis for the ASTM standard method for measuring the material damping [42]. In the original Oberst method, a cantilever metal beam (steel or aluminum) is coated on one side with a layer of viscoelastic material whose damping is to be measured. The beam is excited by a sinusoidal signal with different frequencies and the frequency response of the system is measured. The loss factor η and the Young's modulus of the material are then extracted from lengthy equations given in [45]. Due to the high thermal coefficient of expansion for most viscoelastic materials, considerable thermal bending is induced on the coating side of the Oberst bar. In order to cancel out the thermal bending, Nashif [43] proposed to coat both sides of the beam. He derived separate expressions for calculating the modulus and the loss factor. In this method, the loss factor of the metal beam is assumed to be negligible. Jones [44], further improved the testing apparatus with an approach that allowed the test specimen to be heated to any temperature within the limitation of the testing apparatus.

Cannon, Nashif and Jones [45] have proposed another method for measuring the damping ratio of very soft viscoelastic materials. In this method, a cylindrical specimen of the material with a variable mass on top is driven by a shaker. The loss factor can be calculated by measuring the amplification factor, which is the ratio of the resonant displacement response of the top mass to the shaker input. Although, this method requires a simple test setup, it is not very accurate for materials with modulus greater than 7 MN/m^2.

Ritcher [46], has proposed a rotating-beam deflection method for measuring the damping ratio. In this method, a tubular shaft, made of the material under investigation is mounted in a cantilever mode and rotated about its axis in a horizontal plane. The horizontal and vertical displacements of the free end of the shaft are measured optically, and their ratio is related to the loss factor. The rotating-beam deflection method, however, has not been popular since it requires very-high-precision optical instruments and is limited to very low frequencies (0.001 to 20 Hz).

Damping has been estimated in the special case of a base-excited system by measuring the ratio of tip to base displacement amplitudes of a cantilever-beam specimen vibrating in its fundamental mode [47-50]. Gibson and Yau [51], have derived a more general expression for calculating the damping in terms of the displacement amplitude at an arbitrary point along a beam vibrating in any mode. In a previous paper, Gibson and Plunkett [52], have measured the damping ratio of a double-cantilever beam specimen from the energy balance method. Under steady state conditions, the material damping is defined in terms of the ratio of input energy to the strain energy stored in the systems. In their experiments the specimen was driven in its first or second mode, and the resonance frequency, input acceleration and bending strain (using a strain gage) were measured. The input energy and the strain energy were calculated from the above-measured quantities and the specimen geometry. The accuracy of the damping ratio obtained by this method depends on the accuracy with which the bending strain is measured.

A method utilizing the gravitational acceleration called the _gravity method_ has been proposed by Sekiguchi and Asami [53] for measuring large damping. The authors have used this method for measuring the viscous damping coefficient of an oil damper. Several types of _wave propagation methods_ have been reported in recent years in connection with the measurement of dynamic modulus of long and slender composite specimens or structural elements [12,54]. The dynamic properties of the test specimen are measured by observing the changes that occur in certain characteristics of a stress wave during its propagation through that medium. Both pulse and continuous waves can be utilized. The main advantage of this method is its ability to generate damping data that are independent of the damping of the support system. The drawback, however, is that tests are confined to long and slender rods subjected to high loading rates.

Summary

Among the various methods for measuring the damping ratio of materials and structures described in this chapter, the logarithmic decrement method and the half-power points method are simple, but not very accurate. For obtaining more accurate results, either the impulse response method or the improved resonant forced vibration technique should be used. The improved resonant forced vibration technique consists of the estimation of the damping ratio from an iterative least-squares curve-fitting procedure for the measured frequency response data. The non-resonant forced vibration technique is applicable only for testing very small samples in the low frequency range. For studying the variation of damping with frequency, the input power-method can be used to get some approximate idea. Finally, several new methods developed specially for evaluating the damping of viscoelastic materials were described.

The choice of the technique to be used for a particular application depends on several factors such as : 1) the modulus of the material, 2) the damping of the material, 3) the instrumentation available, d) the frequency and displacement amplitude range of interest, e) the accuracy required in the estimation of the damping, etc. As a rule, while measuring the material damping by any method care must be exercised to minimize the errors due to various factors in the data collection, and data analysis process. Some of these factors are listed below:

1) Specimen mounting - mount the specimen so as to avoid external losses at the supports, joints etc. A free-free boundary condition is ideal for material damping measurements.

2) Transducer/exciter mounting - location and orientation - use of mini-accelerometers or non-contacting type of transducers and exciters is recommended to minimize the effects of the added mass on the response of the system.

3) External disturbances - Minimize the effects of external influences like, electro-magnetic interference, foundation vibration, acoustic noise, cable motion, air damping, fluid flow, etc.

4) Non-linearity of the structure -- such as, rattling, banging, whipping of loosely fastened components, violation of "small-displacement" theory, non-linear stiffness, non-linear damping, etc. should be avoided wherever possible.

5) Data analysis - The various signal processing errors that could arise because of inappropriate selection of the measurement parameters

such as weighting function, number of averages, amount of overlap, calibration factor, etc. should be minimized. Errors due to aliasing and leakage should also be reduced.

III. LITERATURE REVIEW

Previous Pertinent Work on the Damping of Composite Materials

Efforts to measure, model and improve the dynamic properties of advanced fiber-reinforced polymer composite materials have been reported in several publications in recent years. There is a wide range of specimen configurations, materials, frequency range, and testing conditions, in the existing literature. Bert [55], Gibson and Wilson [56], and Gibson [57] have reviewed the work of various investigators in this area. Schultz and Tsai [58] have reported the measurement of elastic moduli and damping ratios of glass epoxy composite materials. Data on moduli and damping ratios were gathered by studying the free and forced transverse vibrations of cantilever beam specimens in the frequency range from 5 Hz to 10,000 Hz. The elastic moduli showed little tendency to change within this frequency range, and the damping ratios were typically of magnitude 10^{-2}. They however, exhibited both frequency and amplitude dependence. Jones [59] has measured the damping ratio of steel epoxy composite material having controlled volume fractions and varying wire sizes.

In a study of dynamic properties of graphite epoxy composites, Rehfield et al [60] noticed that these materials experience a degradation of mechanical properties due to moisture absorption and presence of elevated temperature environment. Leung [61] has studied the effects of gamma-radiation exposure on the mechanical properties of graphite epoxy composites. Interlaminar shear strength and the damping ratio showed an initial increase, followed by a decrease as the dosage of the gamma radiation was increased. In another study, Springer and his co-workers [62-64] have made an extensive investigation on the effect of moisture absorption and desorption on the dynamic properties of graphite epoxy and glass epoxy composites. The effect of these properties on the damping capacity, however, was not included in their study.

The effect of temperature on the damping and modulus of composite materials has also been studied. The variation of Young's modulus (E), and loss factor η with temperature at fixed frequency and at low cyclic strain amplitude are typically of the form shown in Figure 5 [65].

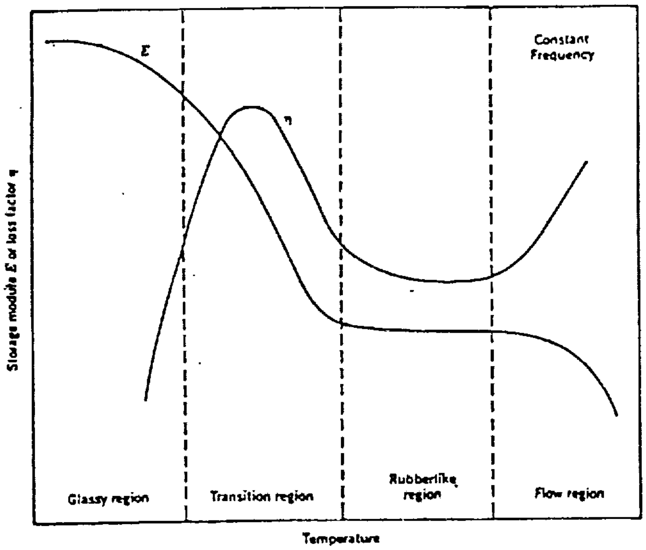

Figure 5. Variation of Storage Modulus and Loss Factor With Temperature for Typical Damping Materials

Three distinct regions are observed, namely the glassy, transition and rubbery regions. In the glassy region E is high and η is low; in the transition region E varies rapidly with temperature and η is high; in the rubbery region E varies more slowly with temperature and η is lower than in the transition region, although not always as low as in the glassy region. For many materials, not one but several transition regions may occur, which usually merge into one another. Yakovlev and Bykovskii [66] have studied the effect of temperature on glass fiber epoxy composites. Their results indicate that the variation of damping with temperature depends on the kind of fiber, fiber length and orientation. The authors also noted that, at cryogenic temperatures, the damping of the glass epoxy composites was much lower than the damping at room temperature.

The effect of fiber orientation and lamination on the elastic modulus and damping capacity of composites has been studied by some investigators [67-73]. In most composite materials, it has been found that the damping is minimum and stiffness is maximum at 0° fiber orientation, i.e., in the fiber direction. As the orientation angle is increased, the general trend is for the damping to increase up to a certain value, and the stiffness to decrease. For carbon fiber epoxy composites, the maximum damping is reported to occur at a fiber orientation of about 67°. According to the study by Mazza et al. [68], cross-ply glass fiber reinforced composites have considerably more damping than 0° unidirectional fiber-reinforced composites. Adams and Bacon [70], in their study noted that the damping of graphite fiber-reinforced composites, decreased slightly with the cross-ply ratio [ratio of the total thickness of layers of 0° orientation to total thickness of layers of 90° orientation].

The effect of imperfect interface bonding on damping characteristics of composites has been investigated by Kishore, et al. [74,75]. Very high loss factors were obtained, and the loss factors were strongly dependent on the coefficient of friction at the interface. Nelson, et al. [76,77] have also noticed that slip in unbonded regions of the interface caused a significant increase in damping.

There is some promise that damping could be used qualitatively to detect damage in composite materials since the damping is quite sensitive to damage in composites. Gibson and Plunkett [78], in their study, progressively damaged cross-ply E-glass composite beams with large amplitude vibration and determined changes in damping and natural frequency. They found that microstructural damage could cause as much as a 350% increase in damping and at the same time reduce the natural frequency by 5% or less. Adams [79], has used frequency shifts of longitudinal modes in a glass epoxy tube cross sectional area. Cawlay [80,81], has extended Adam's work to two dimensions, using modal analysis and finite element analysis to detect and locate localized damage in cross-ply and single-ply graphite epoxy plates. The information on the variation of damping with the number of loading cycles has been most inconsistent. The general trend is for the damping to increase with the number of loading cycles [82.83].

In contrast to this general trend, Kim and Matthews [84], noticed a rapid decrease in damping in the first few cycles, followed by a gradual decrease after that. This initial rapid decrease in the damping was attributed to the residual strain caused by the mismatch between the fiber and matrix thermal-expansion coefficients.

Finally, the mathematical prediction of the dynamic properties of laminated composite materials has been investigated by many authors. Hashin [85] has predicted the complex moduli of unidirectional fiber reinforced materials based on the properties of resin and fiber. Gibson and Plunkett [78] have described a mathematical model for predicting the effective complex moduli of unidirectional and cross-ply glass epoxy beams in flexural vibration. This model was an extension of Hashin's model. Chang and Bert [86] have investigated the analytical characterization of the damping and stiffness behaviour of a single layer of filamentary composite material.

Adams and Bacon [70], have proposed a model for predicting the damping of a narrow angle-ply laminated plate. This method has recently been further developed by Ni and Adams [87]. They have shown good agreement can be obtained between predicted and measured values of damping and stiffness of carbon and glass fiber-reinforced plastic beams. In an accompanying paper, Lin, Ni and Adams [88], have used a finite element model of Cawley and Adams [89] to predict the natural modes and damping capacity of carbon and glass fiber reinforced laminated plates. Hwang and Gibson [90,91], have demonstrated the application of a finite element model based on the strain energy approach for predicting damping in discontinuous fiber composites. Johnson and Kienholtz [92], have also used the finite element method to predict the damping in structures with constrained viscoelastic layers.

Previous Pertinent Work on the Damping of Structural Joints

It has been found that nearly 90% of the total damping which occurs in real structures usually arises in the structural joints [93]. The energy dissipation in a joint is a complicated process involving several mechanisms, the relative significance of which depends on the joint conditions. Because of the complexity of the problem it appears that very little work is being done in analyzing the damping in joints and built-up structures. In an adhesive bonded joint, it is the interface between the adhesive and the adherant that is more prone to environmental degradation and which plays a key role in the damping capacity of the joint. A major source of damping in a joint is the Coulomb friction damping which arises due to frictional forces arising from the relative motion of two contacting surfaces. This is usually modelled by a constant force which is proportional to the normal load between the surfaces and is directed against the velocity vector at each instant. But, in actual practice, the amount of energy dissipated depends on both the normal and tangential forces in a complicated and non-linear fashion [94-99]. Another source of damping in a joint is that due to pumping of air, water or other fluids through highly constrained passages [100,101]. The damping is caused by the change in spacing of the parts. For example, if a rib is riveted or spot-welded to a plate, it will not make contact at all points. If the combination is then bent, the clearance between the two will change, thus 'pumping' the surrounding fluid (air or water) through the narrow passage between them. The viscosity of the fluid will cause the damping.

The damping in a joint is generally non-linear. Most attempts are made to linearize the equations in some way [102,103]. A very useful method is to calculate an equivalent viscous force component to obtain the enegy dissipation. Crawley and co-workers [104-105], have developed a method called the force-state mapping for identifying the non-linear properties of structural members such as joints. The technique includes the use of very accurate instrumentation to measure the force transmission properties of a joint as a function of the relative displacement and velocity across the joint; i.e., as a function of the full mechanical state of the joint. The force-state map of a general linear spring mass damper system would be a plane whose slope with respect to displacement would be the linear stiffness K and with respect to velocity would be the linear viscous damping. Any deviation in a force-state map from a flat plane is an indication of a nonlinearity in the system. The force-state mapping technique has been shown to provide a good method for characterizing the dynamics of joints and structural elements.

IV. MEASUREMENT OF DAMPING OF GRAPHITE EPOXY MATERIAL

The main objective of the work reported in this chapter was to determine experimentally the material damping of the graphite epoxy material used in the construction of the truss system of the Hubble Space Telescope. Other objectives were: a) to study the effect of outgassing (moisture desorption) on the damping of the material, and b) to determine the influence of temperature (both high and low) on the material damping values. Damping measurements were made on both tube and beam specimens. These samples were supplied by the NASA George C. Marshall Space Flight Center. The following sections describe the test strategy, experimental apparatus, test procedure and results and discussions.

Tube Specimen

The composite tube supplied by NASA was in the form of a cylindrical tube with 6.17 cm outer diameter, 0.16 cm wall thickness, and 95.5cm length. The tube was tested to evaluate its damping ratio value under normal atmospheric conditions and in a vacuum chamber to simulate the conditions in space.

Damping Measurements in Normal Atmospheric Conditions

Both free vibration and forced vibration methods were employed. The ambient temperature averaged 27°C during the whole period of experimentation. The tube specimen was first tested with two different types of edge support conditions. They were: 1) knife edge supports to simulate idealized simply-supported boundary conditions at the edges, 2) a three-points support to hold the tube at the edges. Then a free-free support condition with no constraints at the edges, was utilized which was found to be most suitable and consistent for accomplishing our main objective.

The idea of using knife edge supports at the two ends of the tube specimen was to simulate the idealized simply supported boundary condition. This type of boundary condition is normally used in the theoretical analysis for its mathematical simplicity. But to simulate such a boundary condition is rather difficult in practice. The constraint here is that the support should not allow any axial or vertical deflection of the specimen at the ends, and allow any slope at the ends due to any bending moment. With this in mind, it was decided to use circular knife edge supports to simulate this boundary condition. The design was such that one knife edge would support the tube from the inside and the other would support it from the outside at each end location. Each circular outer knife edge was made of stainless steel in two halves to facilitate easy mounting. Each inner knife edge was also made from stainless steel but was only in one piece. A housing to hold the knife edges was designed and fabricated. This housing allowed the movement of the knife edges in the axial direction for fine adjustment. The housing was made from mild steel.

Figure 6 shows the knife edges and housing which were designed. Two such supports were fabricated, one for each end of the tube.

Some preliminary measurements of the damping value of the tube specimen with the knife edge supports indicated a large contribution from the edge supports. Hence, in order to reduce the influence of the support damping and to measure only the material damping, a new type of edge support was designed and fabricated as shown in Figure 7. The idea here was to support the tube at each end at three points which were 120 degrees apart.

Free Vibration Experiments

A schematic diagram of the experimental set-up used in the free vibration tests is shown in Figure 8. The test set-up consists of a non-contacting type (capacitive) displacement transducer (ASP-20) along with a measuring amplifier (Accumeasure System 1000 made by MT Instruments). A holder was developed for the pick-up to allow for easy adjustment of the gap between the specimen and probe surface. The output in the form of voltage from the transducer was fed to the dual channel signal analyzer (B&K type 2032). The specimen was excited for free vibration with an impulse using a small hammer and the vibration displacement as a function of time was recorded on the analyzer. The damping ratio value of the tube specimen was obtained from the time domain data by the logarithmic decrement method. The accuracy of estimation of the damping value was later improved by fitting a curve to the data obtained using a least-squares error criterion.

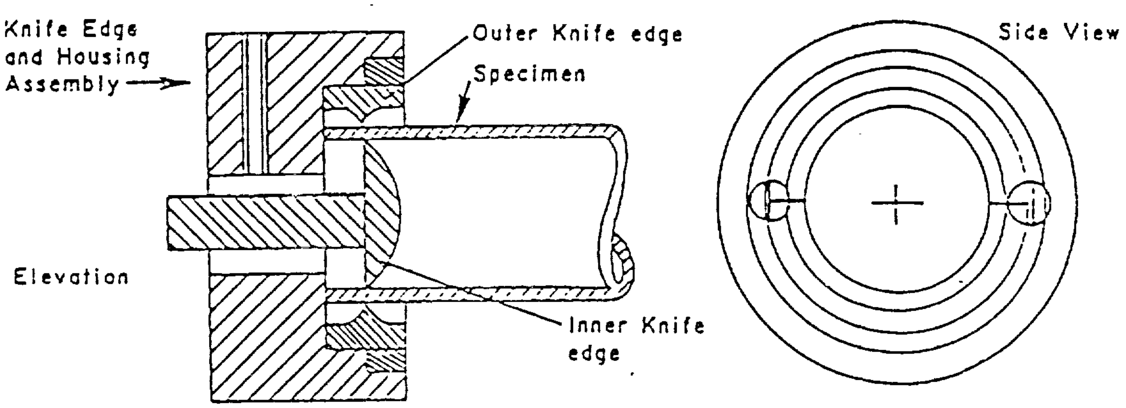

Figure 6. Knife Edge Support for Mounting the Tube Specimen

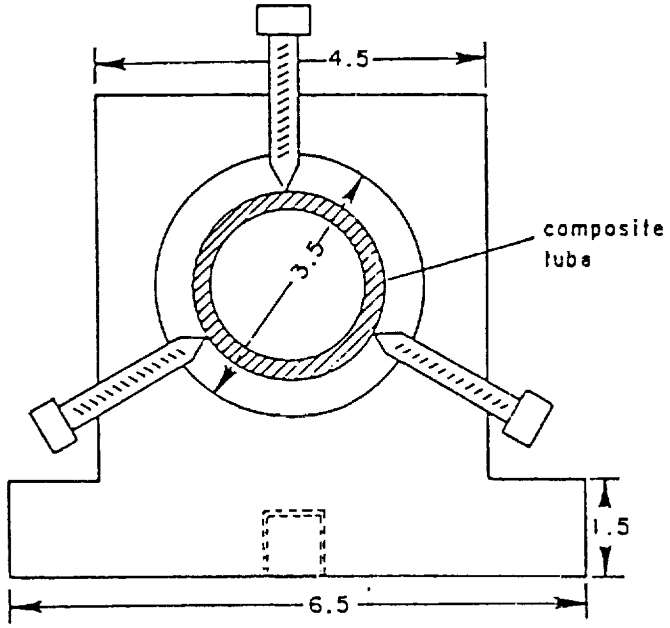

All Dimensions in inches.

Figure 7. Three-points Support for Mounting the Tube Specimen

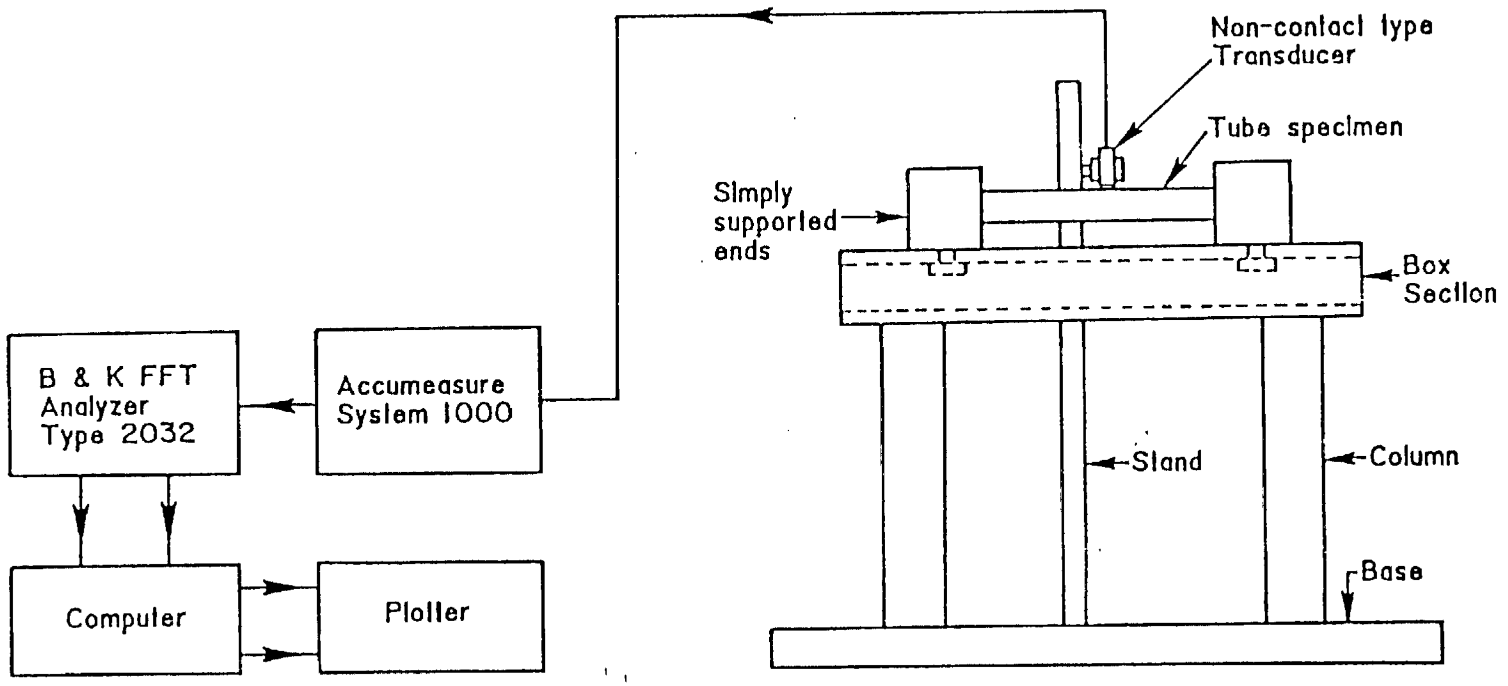

Figure 8. Experimental Set-up for Free Vibration Tests

The experiments were conducted using both the knife edge and three-points supports. The specimen was held in the supports at both the ends. The tube specimen with the supports was clamped to a rigid stand with a heavy base specially fabricated for this purpose. With the knife edge supports, three sets of results were obtained, namely 1) for very large amplitudes of displacement, 2) for moderate amplitudes of displacement and 3) for very small amplitudes of displacement. The values of damping ratio obtained using the logarithmic decrement method in the three cases are summarized in Table 1. It can be seen that the damping ratio is of the order of 1.0% in all the cases. In order to obtain a better estimation of the damping ratio value, a least squares curve-fit was used for the time domain data as mentioned earlier. Figures 9 through 11 show the least-squares fit for the experimental data obtained with the knife edge supports. Note that in Figures 9 through 11 the displacement amplitude is plotted on a logarithmic scale. The tube damping ratio value obtained from the least-squares fit procedure agrees with that obtained from the logarithmic decrement method. It is seen that in Figure 11, for very small displacement amplitudes, there seem to be some oscillations in the decay data. This is perhaps due to the external noise, since at very small displacement amplitudes, the signal to noise ratio is low.

Table 1

Computation of Damping Ratio of the Tube Specimen From Different Cycle Ratios

Case1 Max. Displacement 3.6×10^{-3} cm.	Case 2 Max. Displacement 1.3×10^{-3} cm.	Cycle 3 Max. Displacement 0.1×10^{-3} cm.
$\zeta_{0-35} = 1.09\%$	$\zeta_{0-35} = 1.07\%$	$\zeta_{0-20} = 1.19\%$
$\zeta_{0-20} = 1.00\%$	$\zeta_{0-20} = 1.13\%$	$\zeta_{0-10} = 1.47\%$
$\zeta_{0-10} = 0.97\%$	$\zeta_{0-10} = 1.16\%$	$\zeta_{10-20} = 0.91\%$
$\zeta_{10-20} = 1.04\%$	$\zeta_{10-20} = 1.10\%$	$\zeta_{0-15} = 1.09\%$
$\zeta_{20-35} = 1.20\%$	$\zeta_{20-35} = 0.99\%$	
ζ =1.06% average	ζ =1.09% average	ζ =1.16% average

Legend: the subscript 0-35 indicates that the damping ratio was obtained from the vibration decay measurement from 0 to 35 cycles.

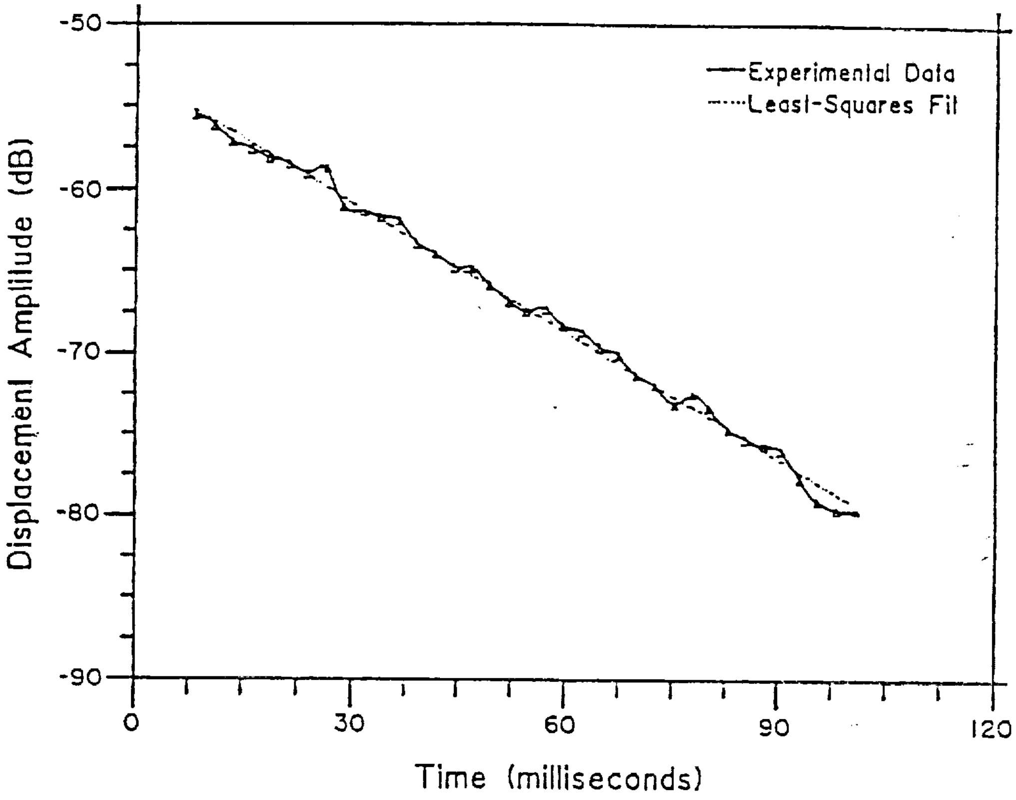

Figure 9. Free Vibration Decay Curve for the Tube Specimen (Maximum Displacement = 3.6 x 10^{-3} cm)

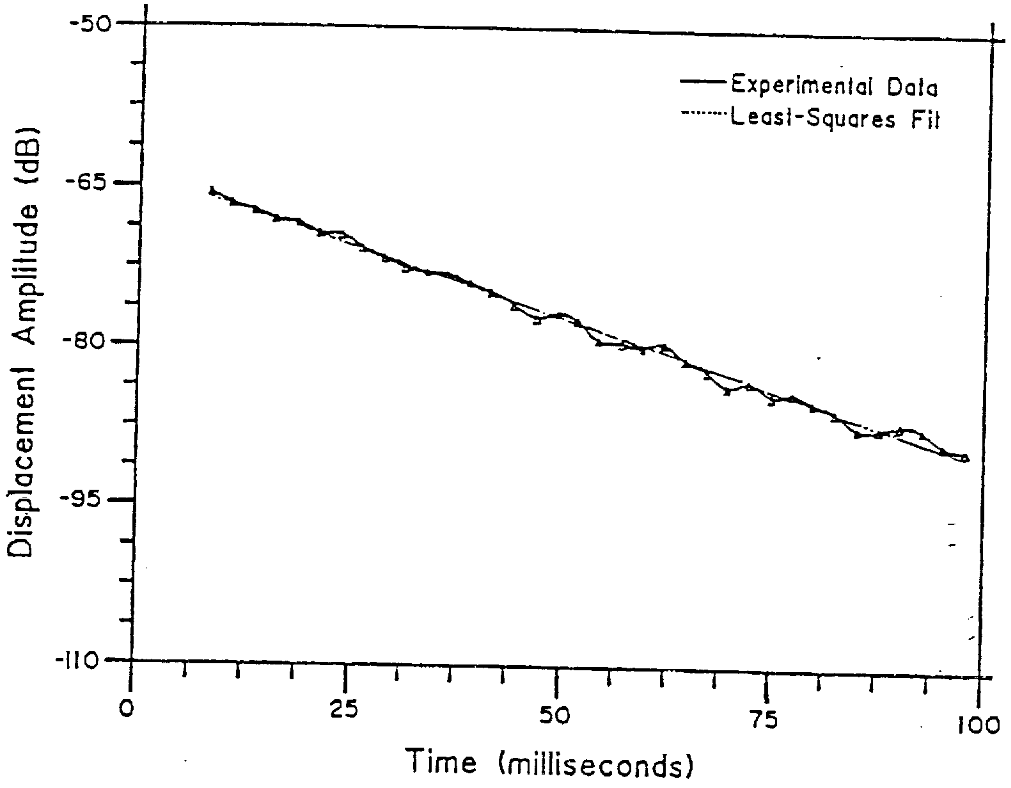

Figure 10. Free Vibration Decay Curve for the Tube Specimen (Maximum Displacement = 1.3 x 10^{-3} cm)

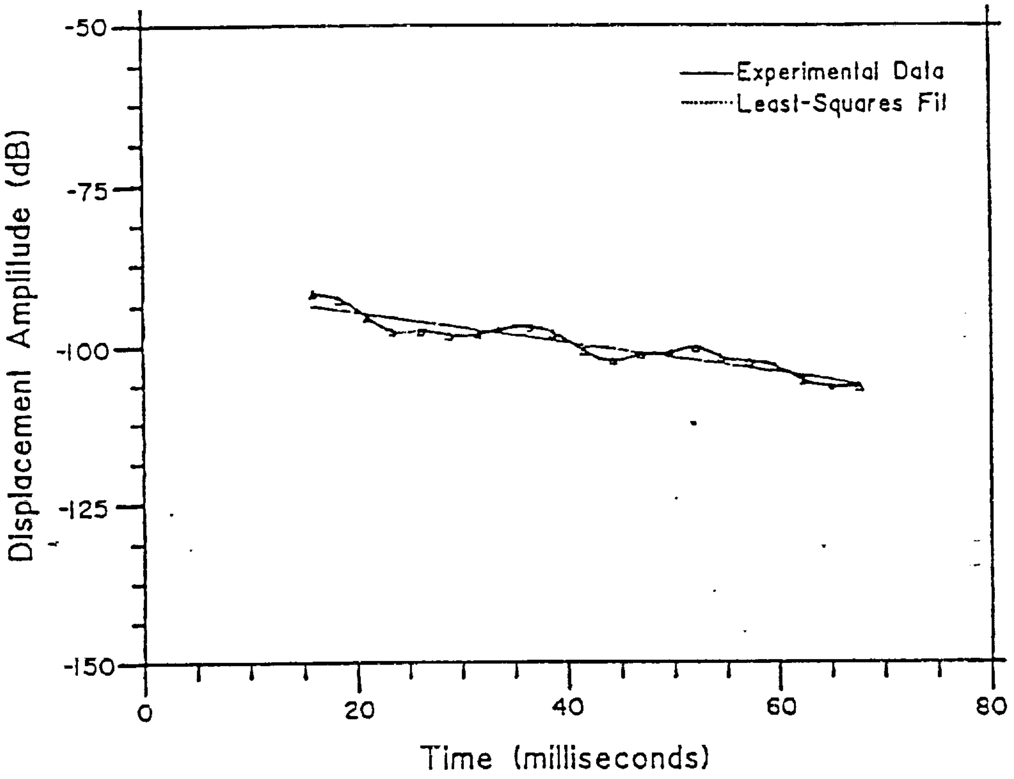

Figure 11. Free Vibration Decay Curve for the Tube Specimen (Maximum Displacement = 0.1×10^{-3} cm)

Experiments were repeated on the tube specimen using the three-points supports at the ends of the tube. The same experimental set up as described earlier was used in this experiment. The damping ratio value with this type of support was also about 1.0%. Experiments with this type of support showed that the damping ratio value is very sensitive to the positioning of the three supports. For the case of the knife edge supports, a Fourier transform of the time domain data indicated a dominant resonance peak at a frequency of 390 Hz, when the length between the supports was 91.4 cm (36 inch). For the case of the three-points support, the resonance frequency was reduced to 299 Hz for the same length between the supports.

The theoretical resonance frequencies of the tube specimen with simply-supported ends for flexural vibration were determined using beam theory. From this analysis, the first and second modal frequencies were found to be 321 Hz and 1287 Hz respectively. Hence, it is seen that the experimental resonance frequency of 390 Hz, is not matched very closely by that of the theoretical first bending mode frequency of the tube specimen. The discrepancy between the two values can be attributed to several factors, such as the knife edges not exactly simulating an ideal simply-supported boundary condition, the material modulus being different in different directions of the tube specimen.

Forced Vibration Experiments

A schematic diagram of the experimental set-up used for conducting forced vibration tests is shown in Figure 12. In this set-up the specimen was excited by means of a shaker (B & K 4809) driven by a random noise generator. The shaker was suspended using a very soft rubber rope thus enabling the natural frequency of the shaker suspension system to be much less than the natural frequency of the test specimen. In the present case the natural frequency of the suspension system was observed to be about 1 Hz. The experiments were performed on the specimen using the same edge supports as in free vibration tests, namely, the knife edge supports, and the three points supports. The frequency response of the specimen in the form of its receptance (displacement/force) was measured using an impedance head (B&K 8001) and a dual channel signal analyzer (B&K 2032.). From the response curve the half power points and hence their bandwidth of frequency separation (Δf) and the natural frequency (f_n) of the specimen were measured. The damping ratio (ζ) is given by $\zeta = \Delta f/2f_n$. The improved half-power points method using a curve-fit analysis (chapter 2) was later used in all the cases to obtain a better estimation of the damping ratio. The results were not very consistent, the lowest value of the damping ratio measured with this support was of the order of 0.57%. Using the same experimental set-up, a second set of experiments was conducted on the tube specimen with the ends supported by means of three-points support. The damping

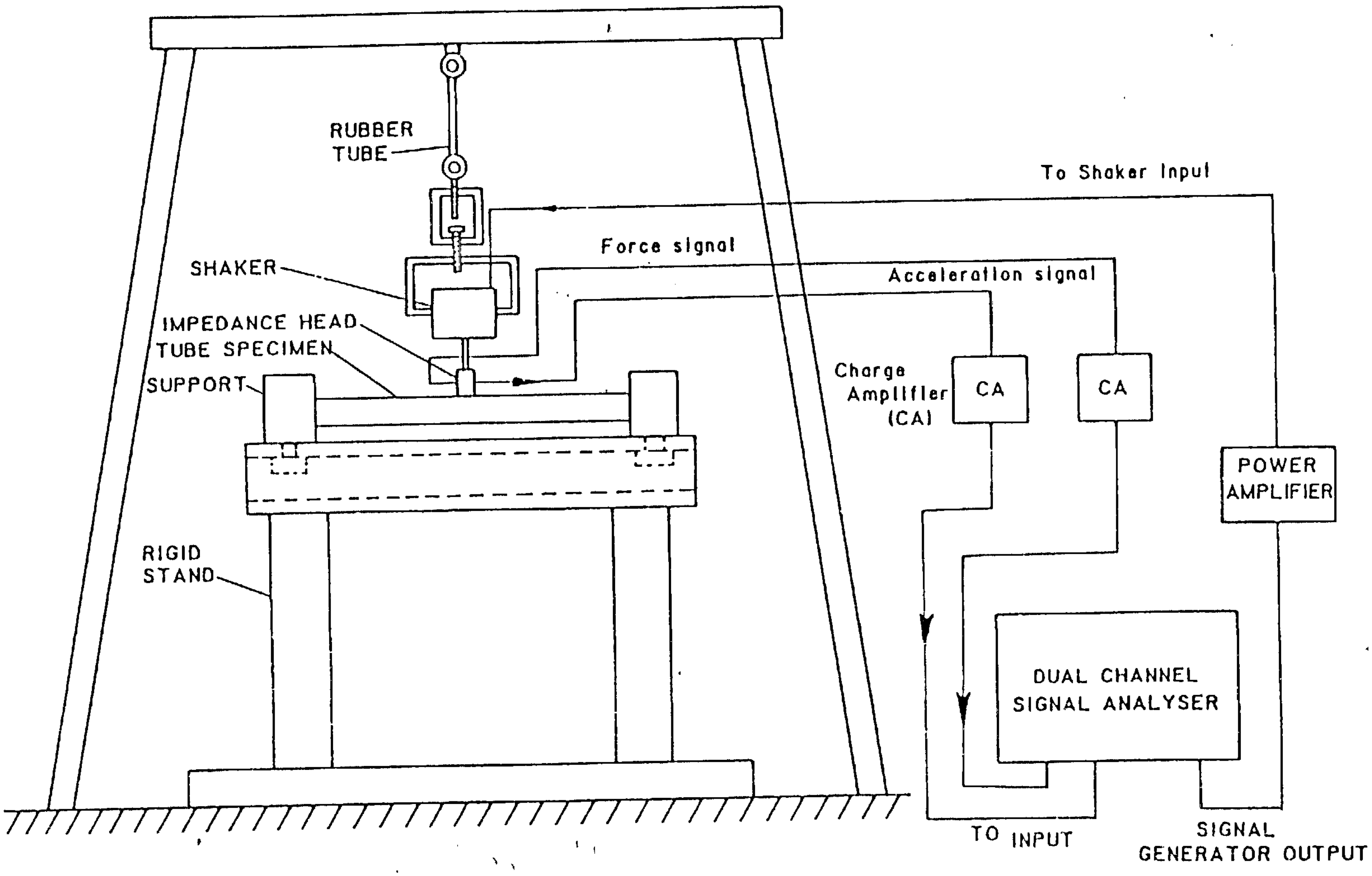

Figure 12. Experimental Set-up for Forced Vibration Tests

ratio value obtained in this case was of the order of 1.15%. The difference in the damping ratio of the composite specimen with the two edge support conditions confirms that the edge supports had considerable influence on the damping ratio of the specimen.

Having established that the damping ratio of the composite tube is strongly dependent on the end support conditions, it was decided to support the specimen so that the two ends of the tube were not constrained at all. This type of support simulated free-free boundary conditions at the two edges. A schematic diagram of the experimental set-up for this case is shown in Figure 13. The specimen was carefully mounted directly on the shaker and the impedance head using a supporting ring (made in two halves) with an interior knife edge as shown in Figure 13. The inner knife edge of the ring allowed the tube to be held firmly in the ring. The ring also had a tapped hole on its outer surface to connect it to the impedance head and shaker assembly.

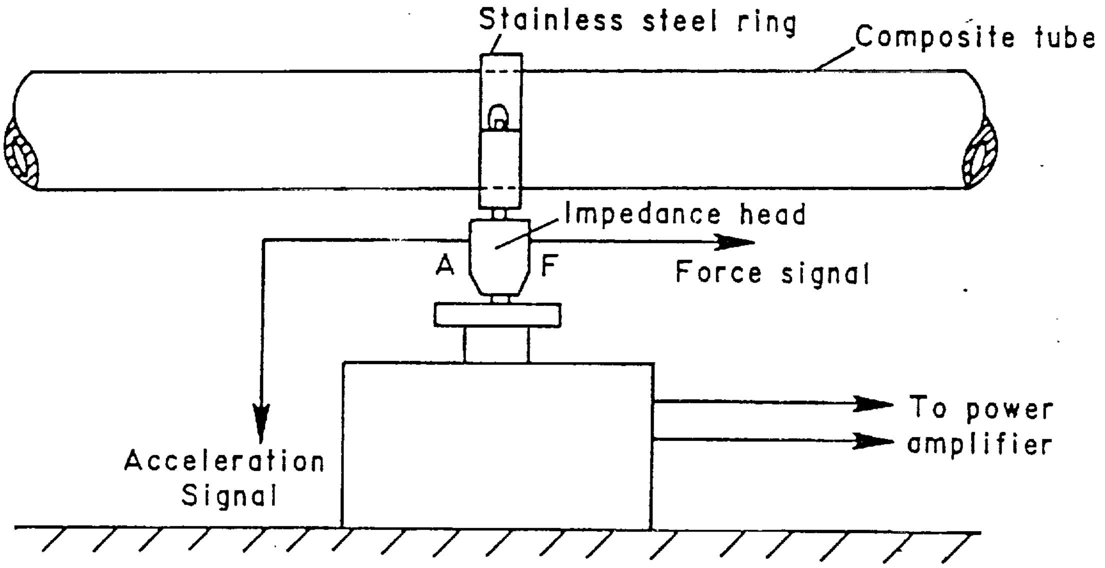

Figure 13. Tube Specimen with Free-Free Boundary Conditions

The tube with the free-free edge conditions was then excited using a random excitation signal in the frequency range of 0-800 Hz. A dominant peak at 509 Hz was observed in the frequency response plot as shown in Figure 14. The response was later measured by zooming into this peak to get better frequency resolution. The so-called zoom analysis is actually a band selectable Fourier analysis, in which Fourier transform based digital spectral analysis is performed over a frequency band whose upper and lower frequencies are independently selectable. In the baseband analysis, Fourier transform is computed in a frequency range from zero frequency to some maximum frequency. This digital Fourier transform is spread over a fixed number of frequency lines (typically 1024) which therefore limits the frequency resolution between lines. Zoom analysis can provide an improvement in frequency resolution of more than a factor of 100, as well as a 10 dB increase in dynamic range compared to baseband Fourier analysis[19]. In the present case, the frequency difference between any two consecutive measurement points on the analyzer was decreased from 1 Hz to 0.125 Hz, through the zoom analysis. With this set-up the damping ratio value of the specimen was measured and found to be about 0.13%. This was the mean value from 10 trials. There was a variation of about ±0.03% in the values of the damping ratio ζ. This value is about 8 times lower than that obtained earlier, and hence was believed to be mostly due to the material damping of the specimen as there were no structural joints and the specimen was not constrained at its ends.

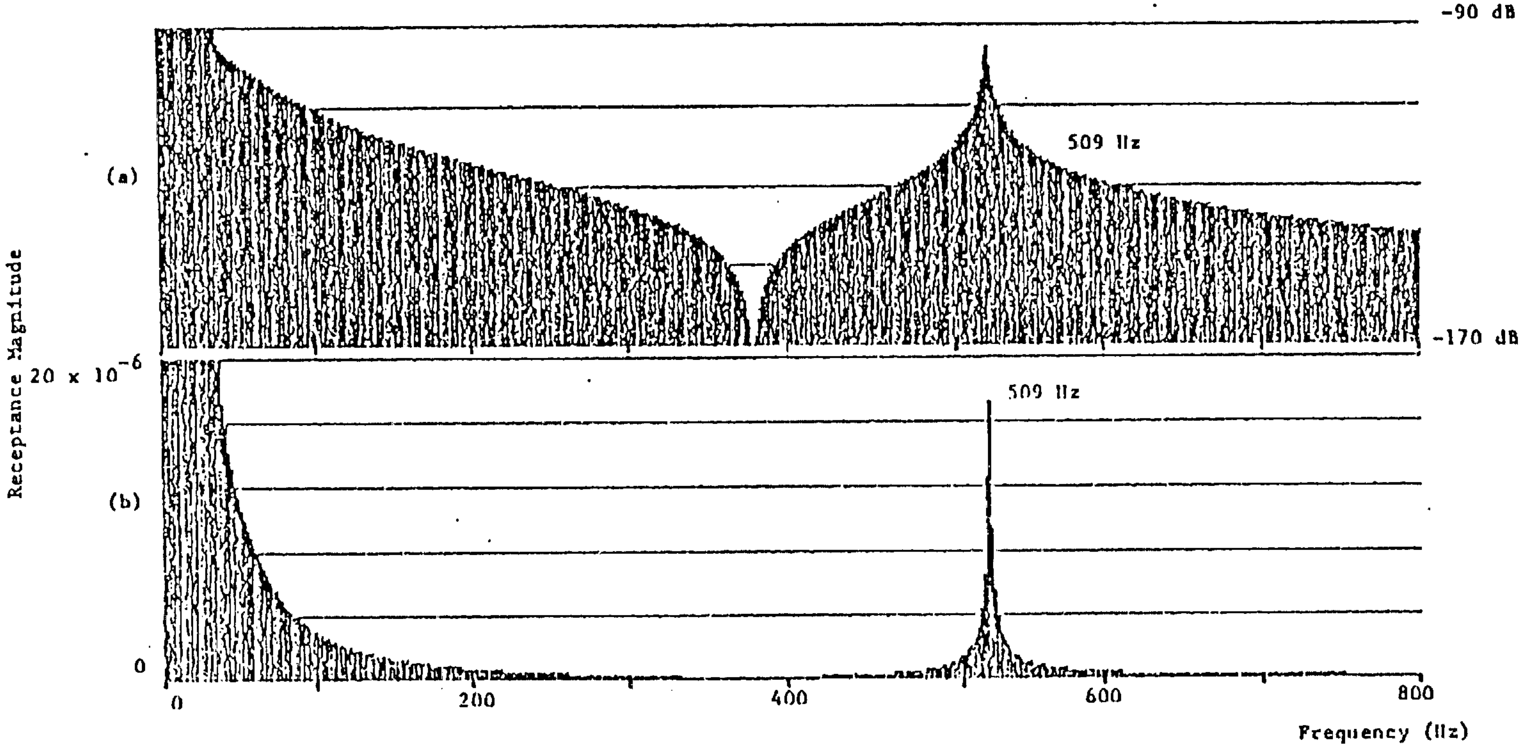

a) Log scale
b) Linear scale

Figure 14. Frequency Response of Free-Free Tube

The measurements were repeated several times on different days, in order to check the consistency of the result. Similar results were obtained on all the occasions. The experiment was also repeated with two other types of excitation signals, 1) pseudo random noise and 2) variable sine with manual sweep. Similar results were obtained with both of these types of excitation.

The next course of investigation was directed at calculating the damping induced by the supporting ring used in the above free-free experiments. In order to check the damping induced by the supporting ring, measurements were made with the top half of the ring removed. The specimen then was supported only by the bottom half of the ring. It was observed that the natural frequency of the specimen (first mode) increased to a value of 552.5 Hz due to the influence of the reduced mass of the supporting ring. But the damping ratio value obtained was the same as that obtained with the full supporting ring, namely 0.13%. This gave more confidence in the measured value of the damping ratio of the specimen. The dominant peak at 509 Hz as shown in Figure 14 corresponds to the first bending mode of vibration of the tube. This was revealed by carrying out a modal analysis of the tube specimen. The measured mode shape is shown in Figure 15.

The next set of experiments was conducted on the cylindrical tube specimen using the free-free boundary conditions (half ring) in order to study the variation of the damping ratio value with different modes of vibration. Figure 16 shows the frequency response curve of the specimen in the frequency range of 0 to 3.2 kHz. The numerical value of the resonance frequency of each mode of vibration cannot be accurately estimated from this plot due to its large frequency range and hence poor frequency resolution. To reduce this problem, two techniques may be used, a) reduce the frequency range of analysis, b) zoom the frequency response plot at the natural frequency of interest. The resonance frequencies estimated from the plots obtained through zoom analysis for the first six modes of the specimen are given in Table 2. It is seen from the table that the damping ratio value increases with the mode number. This increase could be attributed to increased frictional losses at the center support due to increased curvature of the mode shapes at the support point.

Table 2

Damping of the Tube Specimen in Different Modes for Free-Free End Conditions

Peak No.	Frequency(Hz)	Damping Ratio
1	552.5	0.13%
2	1514.0	0.25%
3	1873.0	0.33%
4	2204.5	0.35%
5	2232.0	0.36%
6	2841.8	0.36%

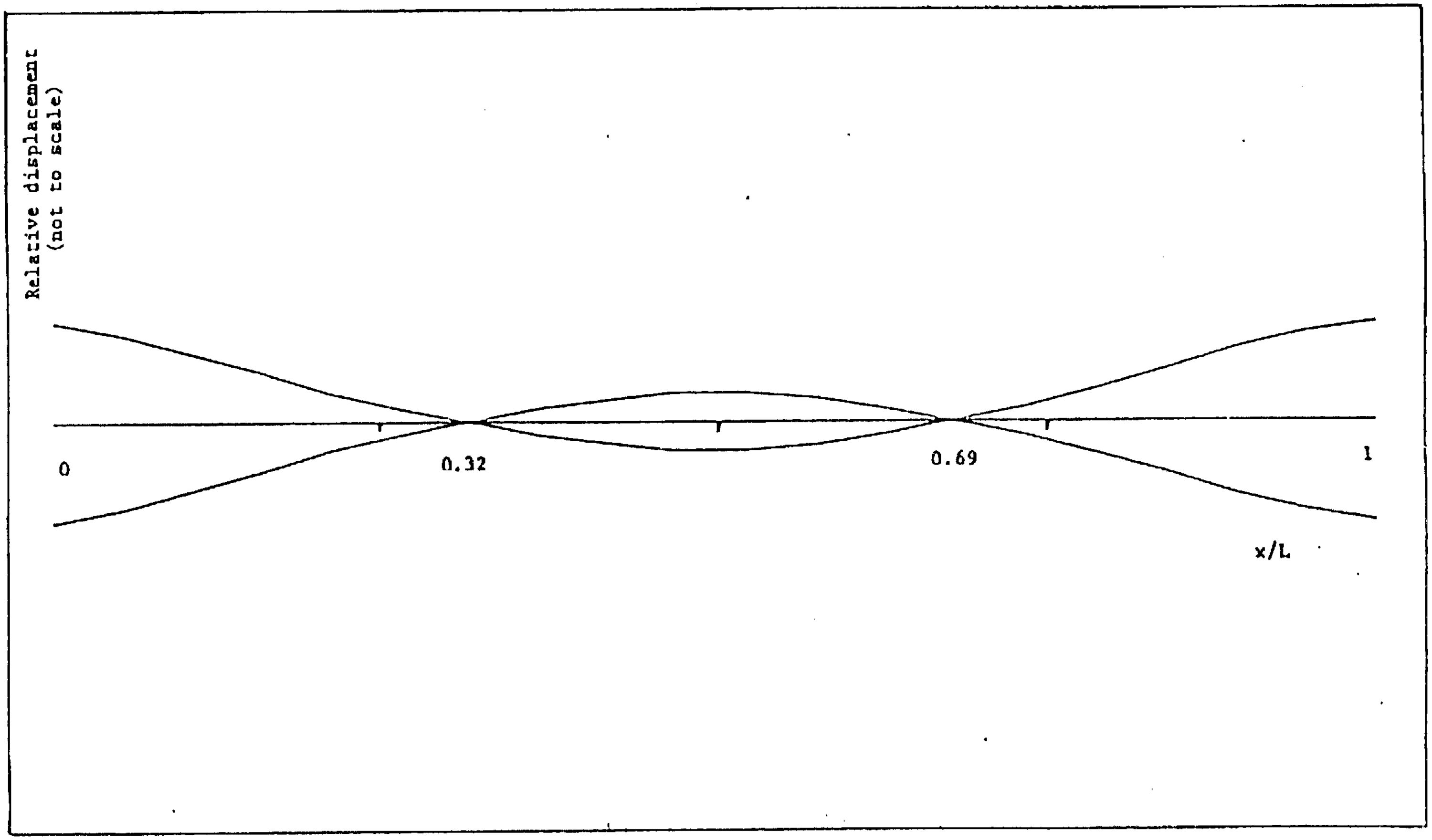

Figure 15. Measuerd Mode Shape of the Tube Specimen Corresponding to a Resonance at 509 Hz

ORIGINAL PAGE IS
OF POOR QUALITY

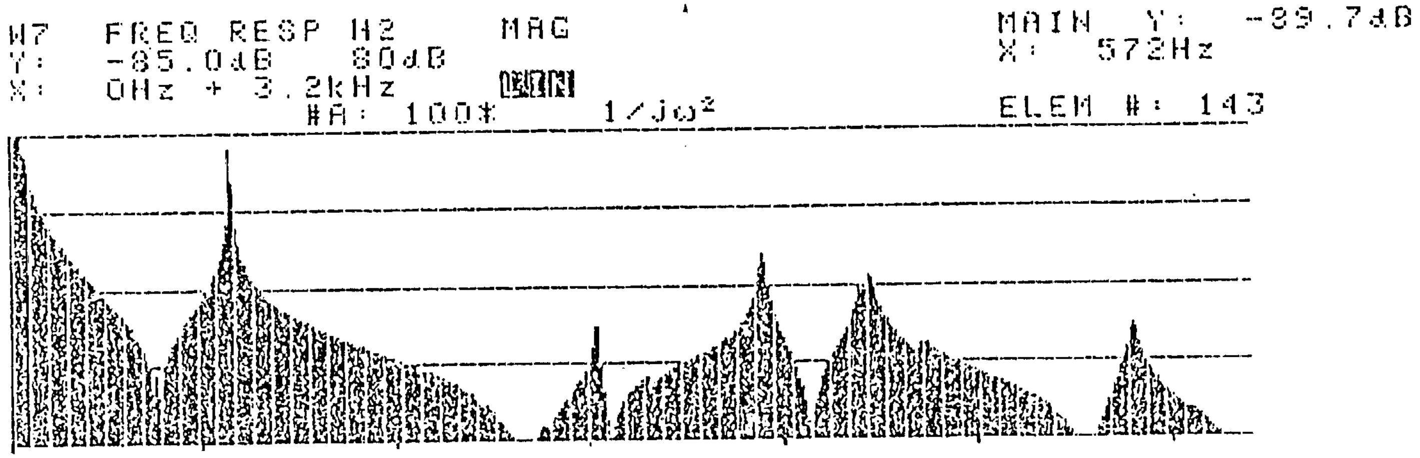

```
SETUP W7

MEASUREMENT:       DUAL SPECTRUM AVERAGING
TRIGGER:           FREE RUN
DELAY:             CH.A→B:  0.00ms
AVERAGING:         LIN    100     OVERLAP: 75%

FREQ SPAN:         3.2kHz      ΔF:4Hz          T:250ms       ΔT:122us
CENTER FREQ:       BASEBAND
WEIGHT CH.A:       HANNING
WEIGHT CH.B:       HANNING
CH.A:              400mV   +    3Hz DIR      FILT:25.6kHz   10.0UNIT/V
CH.B:              1V      +    3Hz DIR      FILT:25.6kHz   50.0UNIT/V
GENERATOR:         RANDOM NOISE           OFF
SINE GENERATOR FREQ.:       165.078Hz
                                                -90
```

Figure 16. Frequency Response of the Tube Specimen Showing Several Resonances

To summarize, all the above experiments were performed on the cylindrical graphite epoxy tube specimen under normal atmospheric conditions. The damping ratio value was measured using free and forced vibration techniques. All of the damping results from the above experiments are summarized in Table 3. The damping values obtained using the free-free boundary condition for the edges are believed to represent most closely the material damping of the specimen. As stated earlier the damping value is significantly influenced by the edge support conditions. Edges and support fixtures can normally be expected to increase the value of damping.

Tabel 3

Damping of the Tube Specimen for the First Bending Mode Using Different End Conditions

End Condition	Damping Ratio	Frequency
Knife Edge Supports	0.90 - 1.10 %	390 Hz
Three-points Supports	1.00 - 1.20 %	298 Hz
Free-Free	0.10 - 0.15 %	553 Hz

Damping Measurements in a Vacuum

A vacuum chamber as described in this section was designed and built to test the cylindrical graphite epoxy specimen. The following factors were considered for the design of the chamber: 1) The chamber should have a small volume which should thus require a short time to create a vacuum in the space. A small volume in the chamber should also make it possible to heat the specimens and degas them more easily. 2) It should have a minimum number of connecting junctions in order to avoid leakage problems. 3) It should be made so that it is convenient to excite the cylindrical graphite epoxy specimens with different edge support conditions. 4) It should be made convenient to test the cylindrical graphite epoxy specimens of different lengths. 5) It should be rigid and should be isolated from the vibration of structural parts. Keeping these factors in mind, two designs were considered: i) A rectangular box type enclosure for the specimen, ii) A cylindrical chamber with end flanges. In view of the difficulties that were envisaged in providing vacuum sealing around all the edges and also the difficulties that are likely to be encountered in providing feed-throughs, a rectangular type of chamber design was discarded.

It was decided to use a cylindrical chamber design whose details are shown schematically in Figure 17. It was also felt that it would be easy to procure cylindrical stainless steel tubes which would then make it possible to avoid many welding and sealing problems. A four-way stainless steel cross (15.24 cm in diameter) was used to support

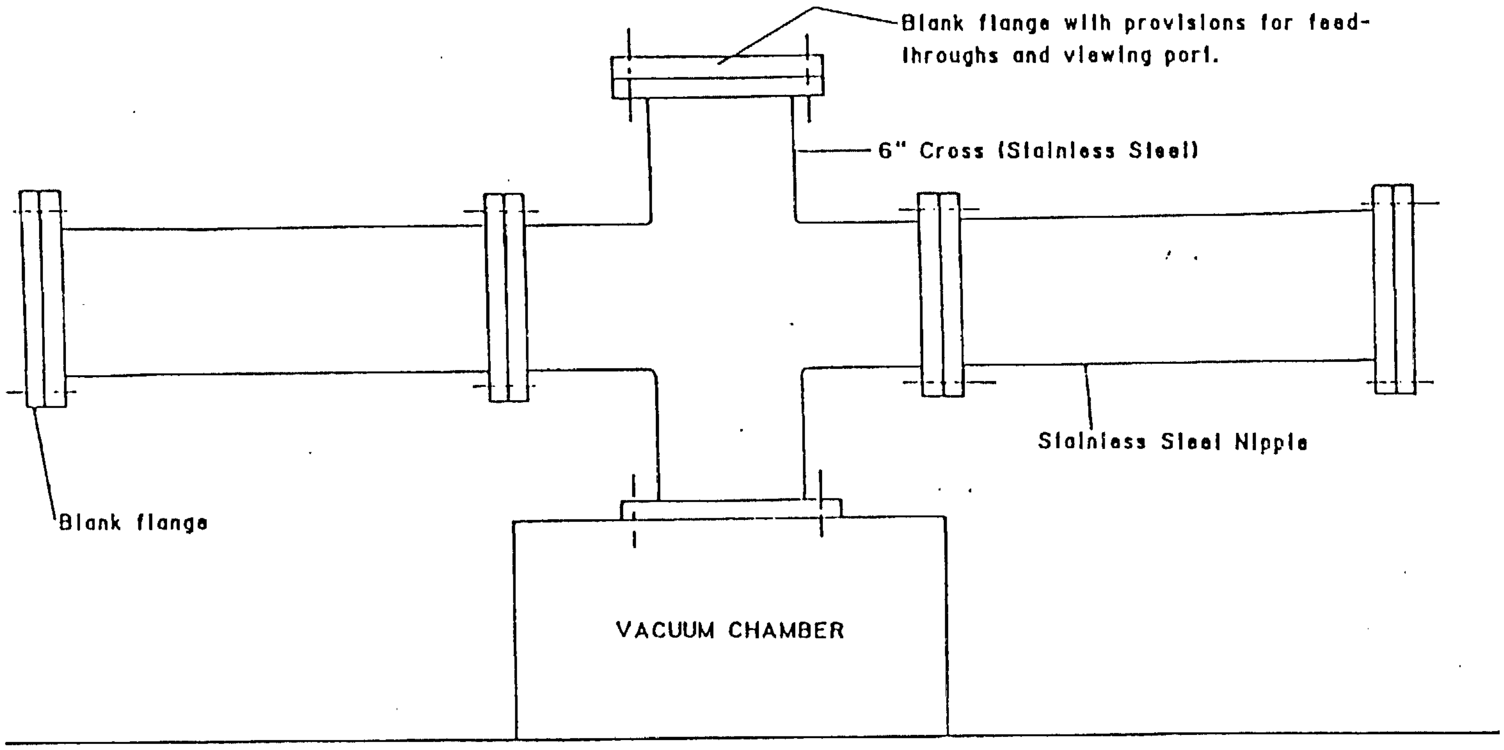

Figure 17. Cylindrical Chamber for Testing the Tube Specimen in a Vacuum

the chamber as shown in Figure 17. The feed-throughs, ports, etc. were provided at the top of the cross. A heating coil was provided inside the chamber for heating the graphite epoxy specimen. This heating coil was necessary to ensure that the composite material outgassed rapidly. Two six-inch stainless steel tubes (of 33cm length) with end flanges were connected to the flanges on the two sides of the cross as shown in the figure. The bottom flange of the cross was connected to the vacuum pump unit. The joints at the flanges were provided with O-rings and were sealed with vacuum grease. Considerable time and effort was spent to detect the leaks in the vacuum system and in the vacuum chamber. The system was able to produce a vacuum pressure of about 10^{-3} torr (1 torr = 1 mm of Hg).

The tube specimen was carefully placed and positioned in the vacuum chamber. A free-free edge support condition was simulated for the specimen by the use of the full ring with an inner knife edge as discussed earlier. The tube specimen was excited by means of an electrodynamic shaker. Figure 18 shows the fixture designed for exciting the tube specimen in the chamber for forced vibration experiments. The excitation force from the shaker was transmitted to the composite tube with the help of a thin rod and a metallic bellows assembly. The end flanges of the bellows were connected to the mating flanges of the connecting elements (half nipples) by using copper gaskets and screw nuts. Care was taken to see that the specimen was in a horizontal position and that it did not touch the sides of the

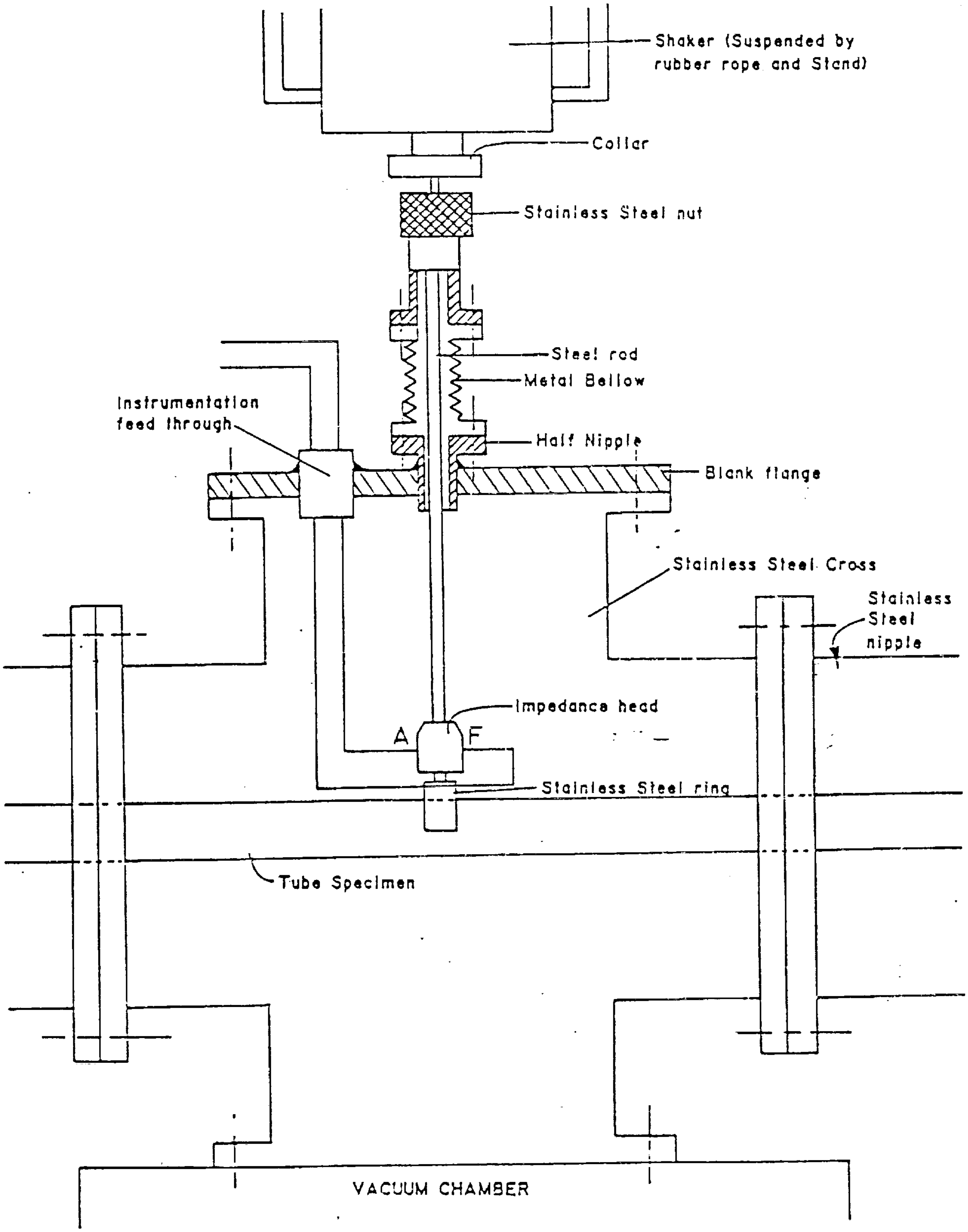

Figure 18. Experimental Set-up for Exciting the Tube Specimen in a Vacuum Chamber

vacuum chamber. Figure 19 shows a photograph of the vacuum chamber in its assembled form, and Figure 20 is a cut-out view of the chamber showing the composite tube, heating coil and the impedance head.

Experimental Procedure and Results

As before, the frequency response measured in the present case is also the receptance, which is the ratio of the displacement to force. The damping ratio and the undamped resonance frequency were estimated using the half-power points method along with the curve-fitting technique which was discussed before. Random excitation with a Hanning window was used in all the experiments. Some experiments were repeated with a swept sine excitation and similar results for the damping ratio value were obtained as with random excitation. The random excitation was chosen since results are obtained faster with this type of excitation than with sine sweep testing. The response curve was zoomed in the frequency range of 450 Hz to 550 Hz to obtain the first bending mode of vibration. This was found to be the best set-up for a good frequency resolution.

First, measurement of the damping ratio of the tube specimen was made while the tube was in the vacuum chamber before the air was pumped out. Several measurements were made in order to check the repeatability of the results. Figure 21 shows the result of a measurement made on the tube at 27°C (80°F) under atmospheric conditions before the chamber was evacuated. The damping ratio

ORIGINAL PAGE
BLACK AND WHITE PHOTOGRAPH

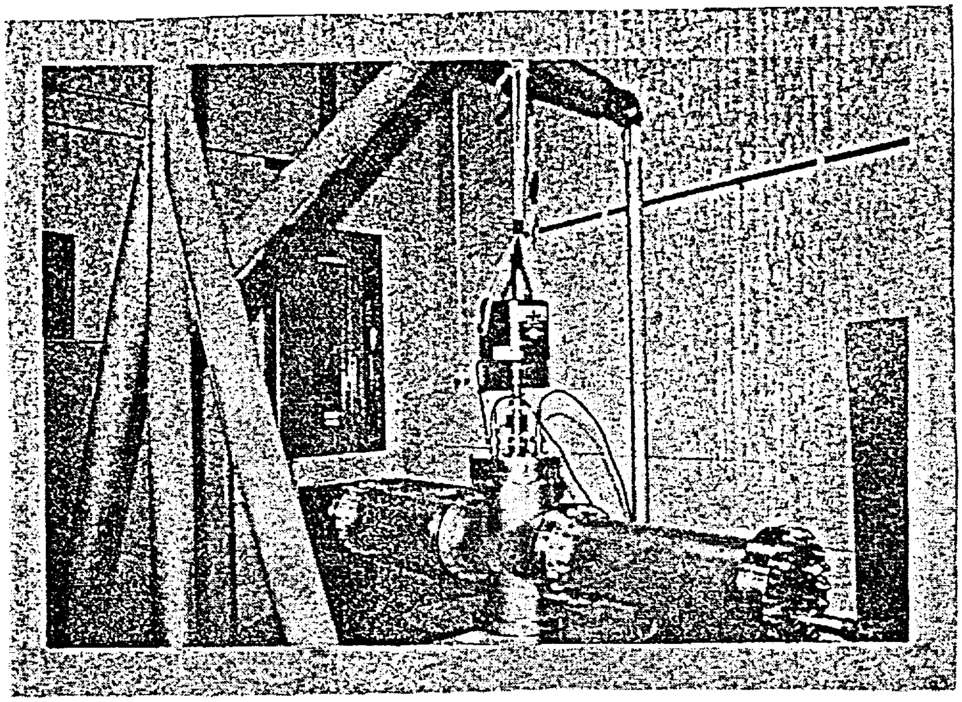

Figure 19. A Complete View of the Vacuum Chamber

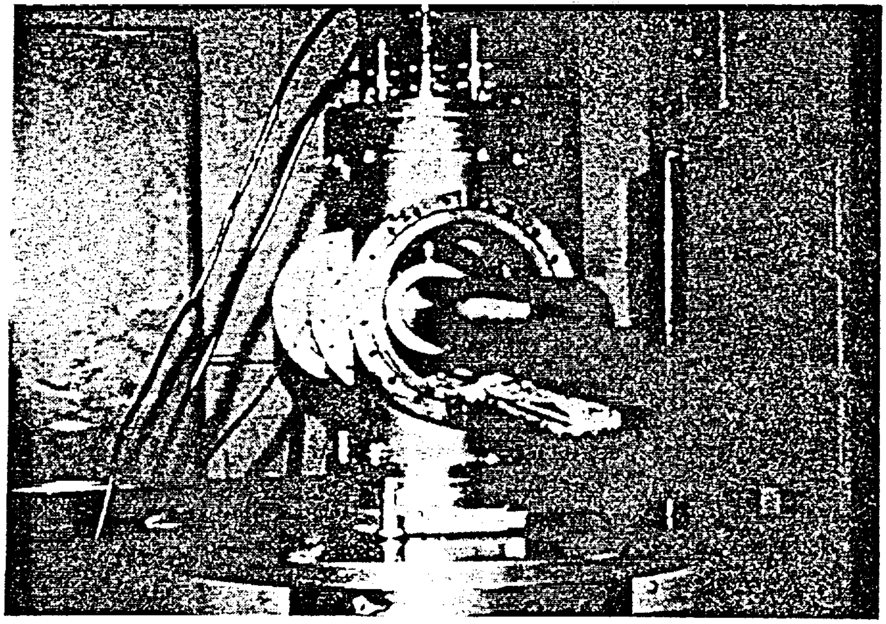

Figure 20. A View Showing the Tube Specimen Inside the Vacuum Chamber

measured was about 0.10% and the resonance frequency was about 531.9 Hz. This value of the damping ratio is somewhat close to the value of 0.13% obtained earlier for the same specimen in tests performed in normal atmospheric conditions. The slight discrepancy between the two values can be attributed to the difference in the experimental configuration.

Later the end flanges of the vacuum chamber were closed and the vacuum pump was started. The damping ratio value and the resonance frequency of the tube specimen were measured on each day for the next two days. The vacuum pressure was observed to be 10^{-2} torr on the second day and 10^{-3} torr on the third day. The temperature inside the chamber was still the ambient temperature, namely 27°C (80°F). The damping ratio value of the specimen was measured to be 0.069% on both of the days. Figure 22 shows the frequency response plot measured on the second day.

The heating of the specimen was started on the third day. A heating coil was placed inside the vacuum chamber below the tube specimen (before pumping was started). Care was taken to see that the coil did not touch the tube anywhere. The current through the coil was gradually increased until the temperature of the space inside the chamber was 94°C(200°F). The tube was kept inside the chamber at this pressure for a period of one month. The objective was to desorb the moisture from the tube material.

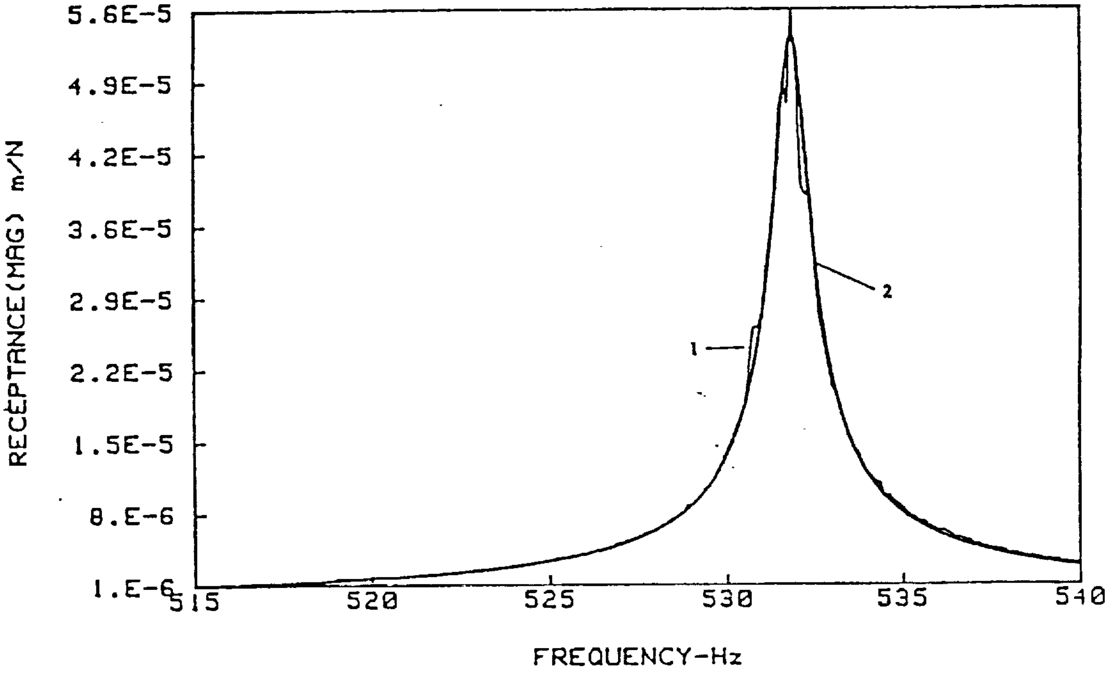

Figure 21. Frequency Response of the Tube Specimen Under Atmospheric Conditions

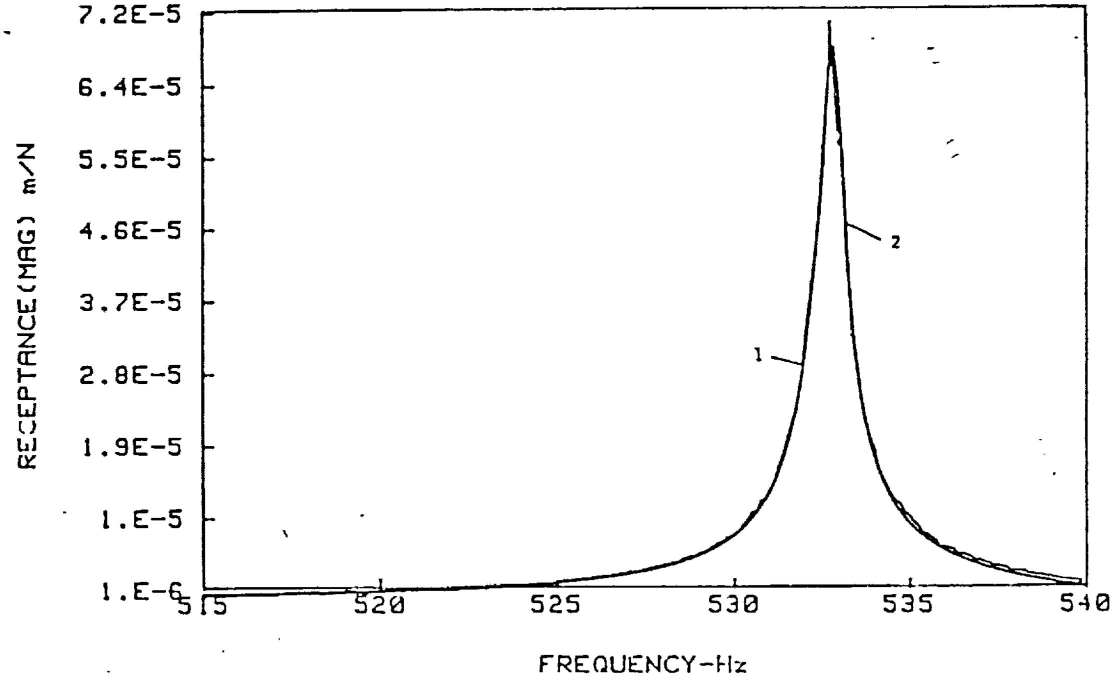

1- Measured Data, 2- Curve-Fit Data

Figure 22. Frequency Response of the Tube Specimen After Being in a Vacuum for Two Days at 27°C

At the end of the fourth week the heating of the tube specimen was stopped. The tube was then gradually cooled to room temperature. The damping ratio value and the resonance frequency of the tube specimen were measured. When the temperature of the chamber was cooled to 26°C (atmospheric conditions) it was interesting to observe that the damping ratio value of the tube was 0.063%. This value is very close to the damping value obtained for the tube specimen four weeks earlier before the heating was started.

Finally after cooling, the pressure in the chamber was restored to atmospheric conditions and the damping ratio value of the tube was measured again. It was found to be 0.083% and the resonance frequency was 531.20 Hz. Earlier, under atmospheric pressure, the tube damping ratio value was measured to be 0.10%.

The tube was then carefully dismantled and it was weighed in a precision balance. The difference in weight of the tube before and after heating was found to be 4.20 grams. The percentage change in the weight of the tube from its original weight was 0.9%. This was assumed to be caused by the loss of moisture which occurred while the tube was degassing. The change in damping ratio value due to outgassing of the tube specimen was observed to be 0.016%.

All of the results discussed so far in this section are summarized in Table 4.

Table 4

Summary of the Damping Data of the Tube Specimen in a Vacuum

ACTIVITY	CHAMBER PRESSURE	DAMPING RATIO •	MASS OF THE TUBE
1. Before pumping the air out	Atmospheric	0.10 %	466.8 grams
2. Immediately after pumping	10^{-2} torr	0.07 %	–
3. Continued pumping–2 days	10^{-3} torr	0.07 %	–
4. Continued pumping and heating the tube to about 100 C for 30 days	$10^{-2} - 10^{-3}$ torr	0.06–0.09 %	–
5. Stopped heating and pumping. Atmospheric conditions restored	Atmospheric	0.08 %	462.6 grams

• Mean value of 10 trials

1 torr= 1 mm Hg

Temperature Effects on the Damping of the Graphite Epoxy Material

The next course of the investigation was directed at finding the effects of temperature on the damping of the graphite epoxy material. Experiments were conducted on both tube specimen and some beam-like samples using specially built temperature chambers. Forced vibration experiments were conducted on these specimens with free-free boundary conditions. All of the measurements were made in air, since, it was more convenient to conduct experiments at controlled temperatures in air than in a vacuum.

High Temperature Experiments

Figure 23 shows a schematic diagram of the experimental apparatus used to study the effects of high temperatures on the damping of beam samples. The specimens were carefully mounted inside the temperature chamber and were supported at the center by a steel rod. The steel rod was tapped and attached through a hole in the specimen by means of a small nut. The other end of the steel rod was connected to the shaker via an impedance head. The force and the acceleration signals from the impedance head were fed to the FFT analyzer after amplification by the charge amplifiers. The temperature inside the chamber was monitored and controlled precisely by two chromel-alumel thermocouples and a temperature control programmer. As before, damping ratio values were extracted from the receptance plots using the improved half-power points method.

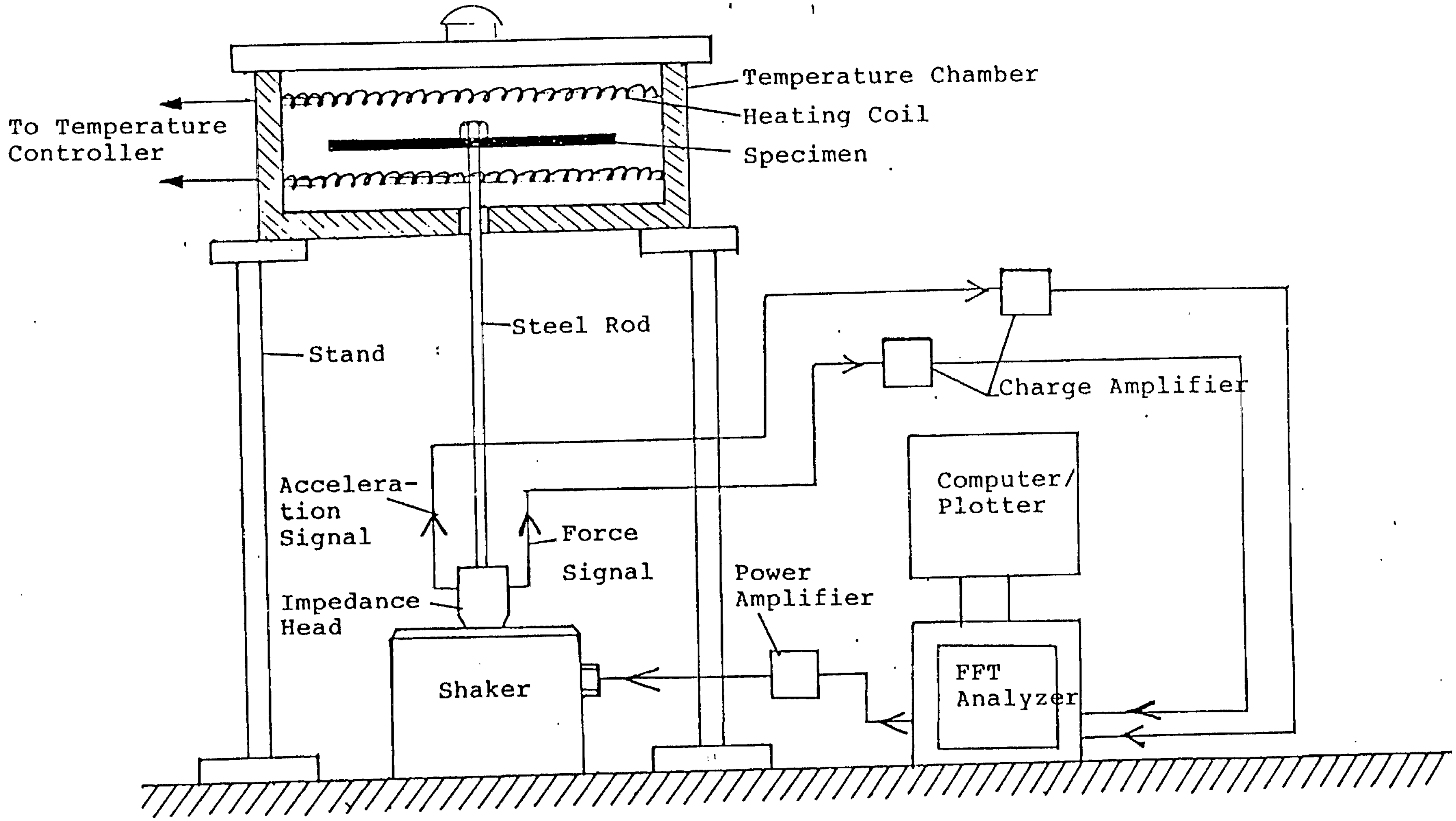

Figure 23. Experimental Set-up for Measuring Damping Under High Temperatures

Figures 24 and 25 show the variation of the damping ratio with temperature for graphite epoxy beam specimens of two different lengths. The temperature where the first peak appears is believed to be the glass transition temperature of the material. As can be seen from these figures, the variation of ζ with temperature has almost the same trend in both cases, and also it agrees well with the standard plot found in the literature [see Figure 5].

A similar experiment was conducted on the tube specimen. Because of the limitations of the heating equipment, it was possible to raise the temperature of the tube only up to 300°C. For better temperature control, the temperature of the tube was measured at three points along its length. The temperature of the tube was gradually increased from atmospheric temperature and damping measurements were made at regular intervals. The frequency response was measured when the tube temperature was the same at all the three points. Figure 26 shows the final result for the variation of ζ from atmospheric temperature to about 300°C. This is again for the first bending mode of vibration of the tube. It is seen from this figure that the trend in the variation of ζ is somewhat similar to that of the beam results, i.e. the damping ratio increases with temperature. The discrepancy in the absolute value of the damping ratios and the value of the glass transition temperature as observed in the three plots could be attributed to a) difference in the geometry of the specimens, b) difference in the frequencies of vibration and c) difference in the lamination (fiber winding) of the beam and the tube samples.

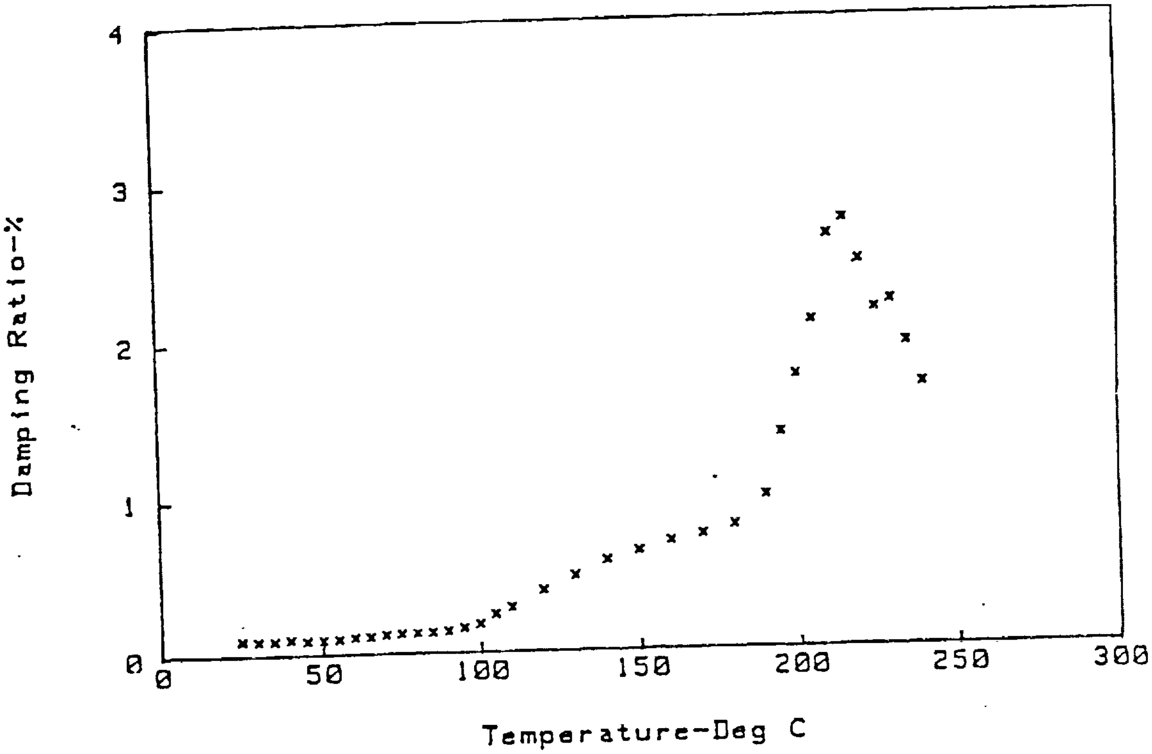

Figure 24. Plot of Damping Ratio of Graphite Epoxy Beam 1 vs. Temperatures Above Ambient

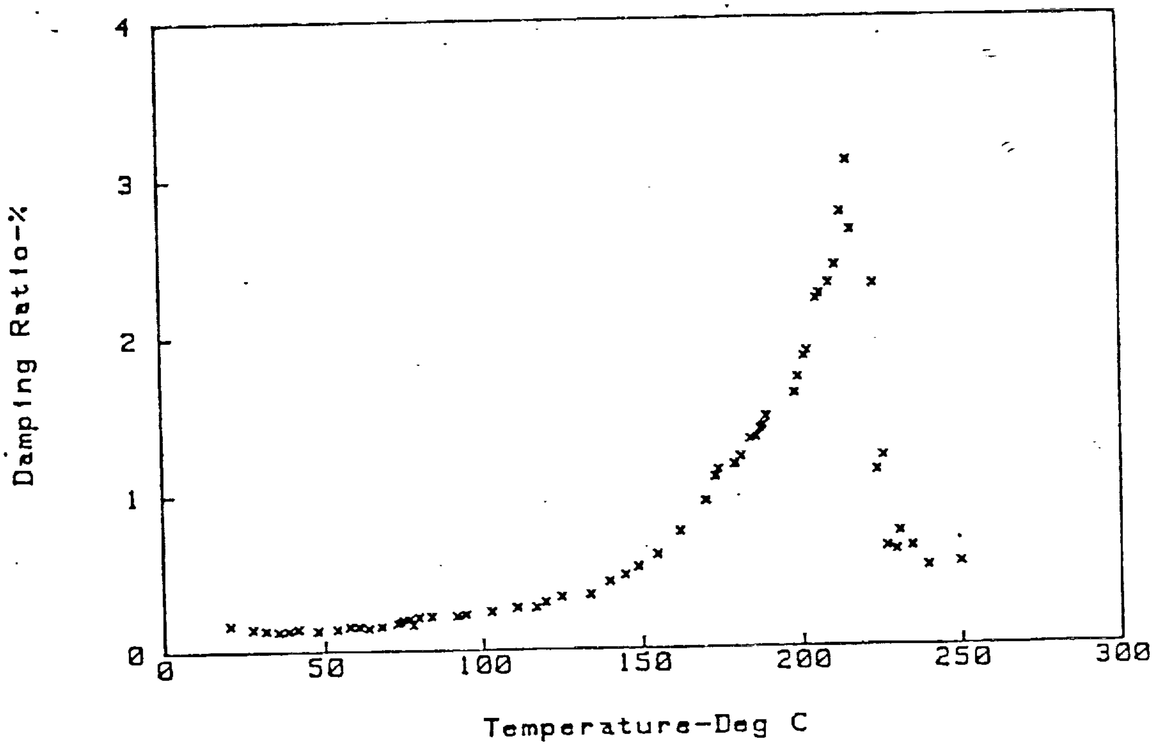

Figure 25. Plot of Damping Ratio of Graphite Epoxy Beam 2 vs. Temperatures Above Ambient

C-2

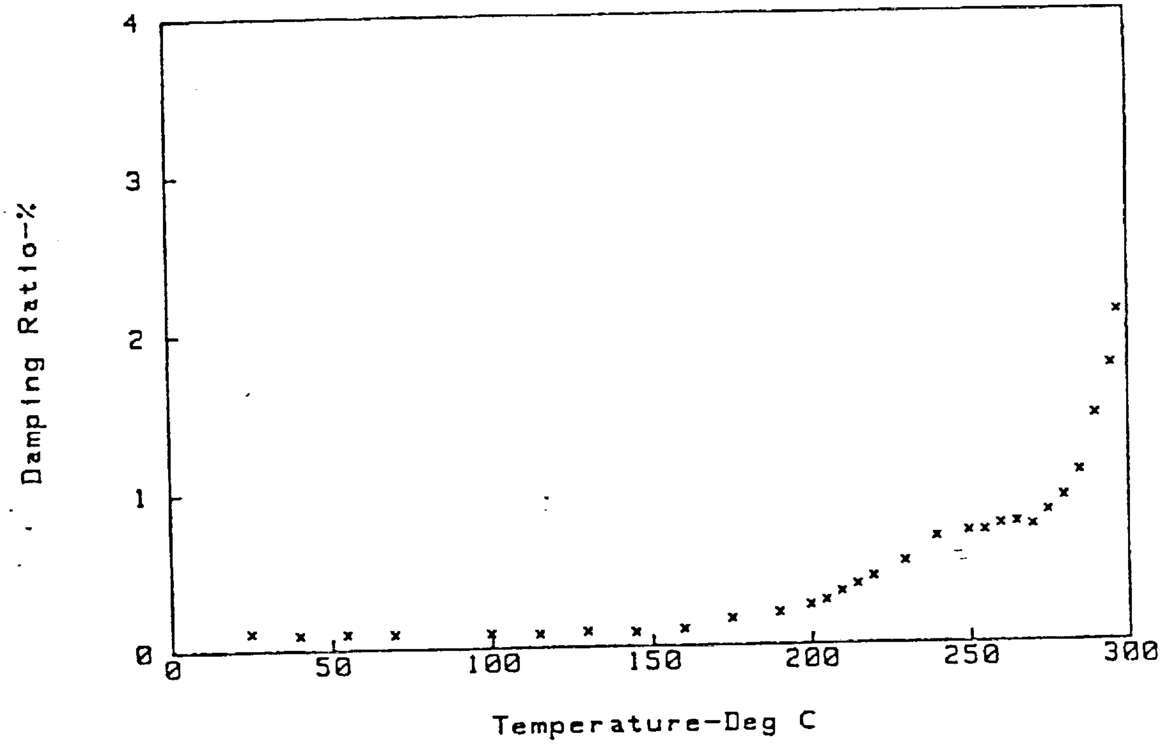

Figure 26. Plot of Damping Ratio of Graphite Epoxy Tube Specimen Vs. Temperatures Above Ambient

In order to gain confidence in the experimental methodology followed, and to validate the results obtained so far, it was decided to conduct the same temperature experiments on some metal beams. Figures 27 and 28 show the variation of damping with temperature for an aluminum beam and a stainless steel beam respectively. As can be seen from these results, the damping capacity of these materials is almost constant with temperature.

Low Temperature Experiments

The experimental apparatus used previously for conducting high temperature experiments was not suitable for conducting low temperature experiments. Hence, an entirely new temperature chamber was designed and fabricated. It was initially planned to conduct the low temperature experiments in a vacuum chamber. Thus, the set-up shown in Figure 29 was developed. As can be seen from the figure, the specimen to be tested was enclosed in a temperature chamber, which, in turn, was placed in a vacuum chamber. The specimen was connected to the shaker (the shaker was kept outside the temperature chamber, but inside the vacuum chamber) by means of a steel rod and an impedance head as was done during the high temperature experiments. The temperature chamber consisted of double-layered side walls forming a closed cavity. The cavity had an inlet and an outlet for the flow of liquid nitrogen through it. The outside surface of the chamber was well-insulated so that only the specimen which is inside the chamber will be cooled. There was also a small heating coil in the chamber to heat the specimen if required. The flow of liquid nitrogen was

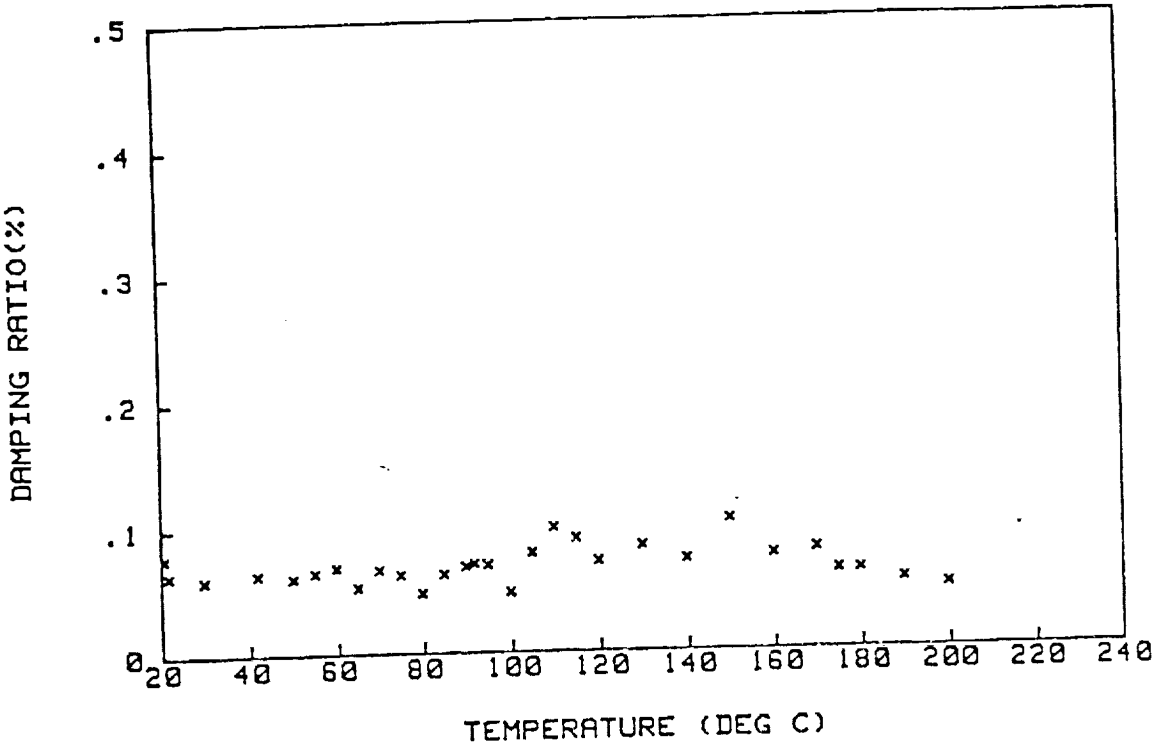

Figure 27. Plot of Damping Ratio of Aluminum Beam vs. Temperatures Above Ambient

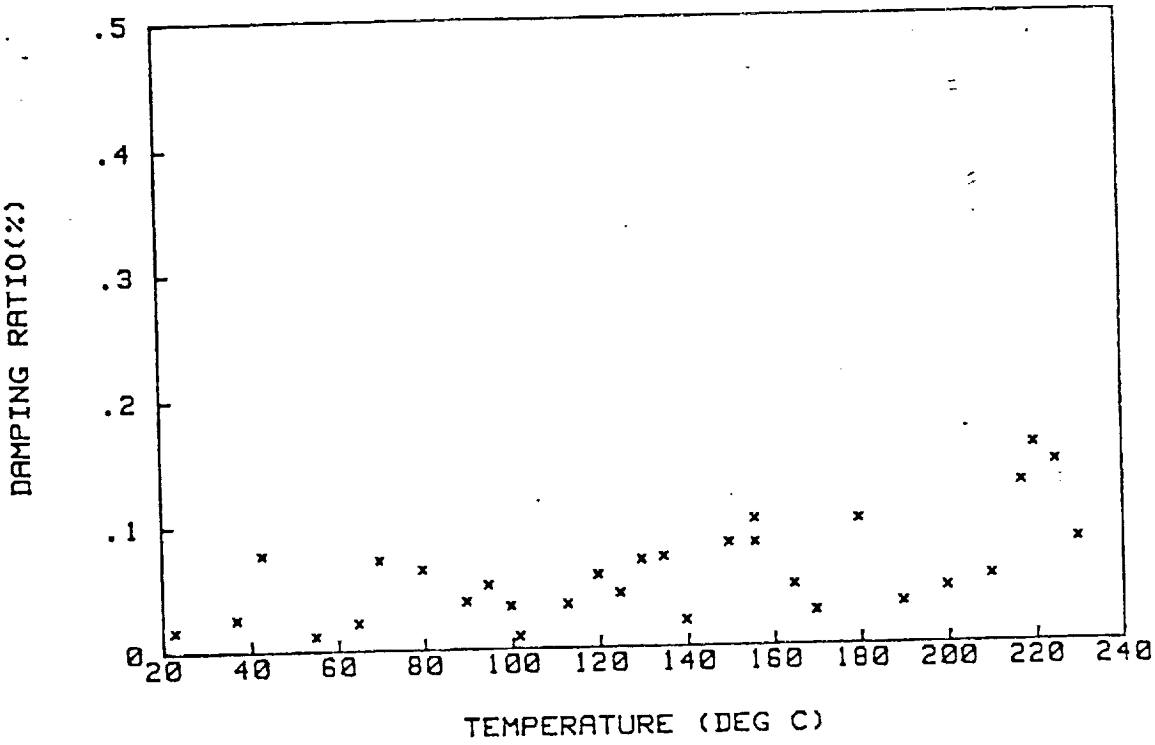

Figure 28. Plot of Damping Ratio of Stainless Steel Beam vs. Temperatures Below Ambient

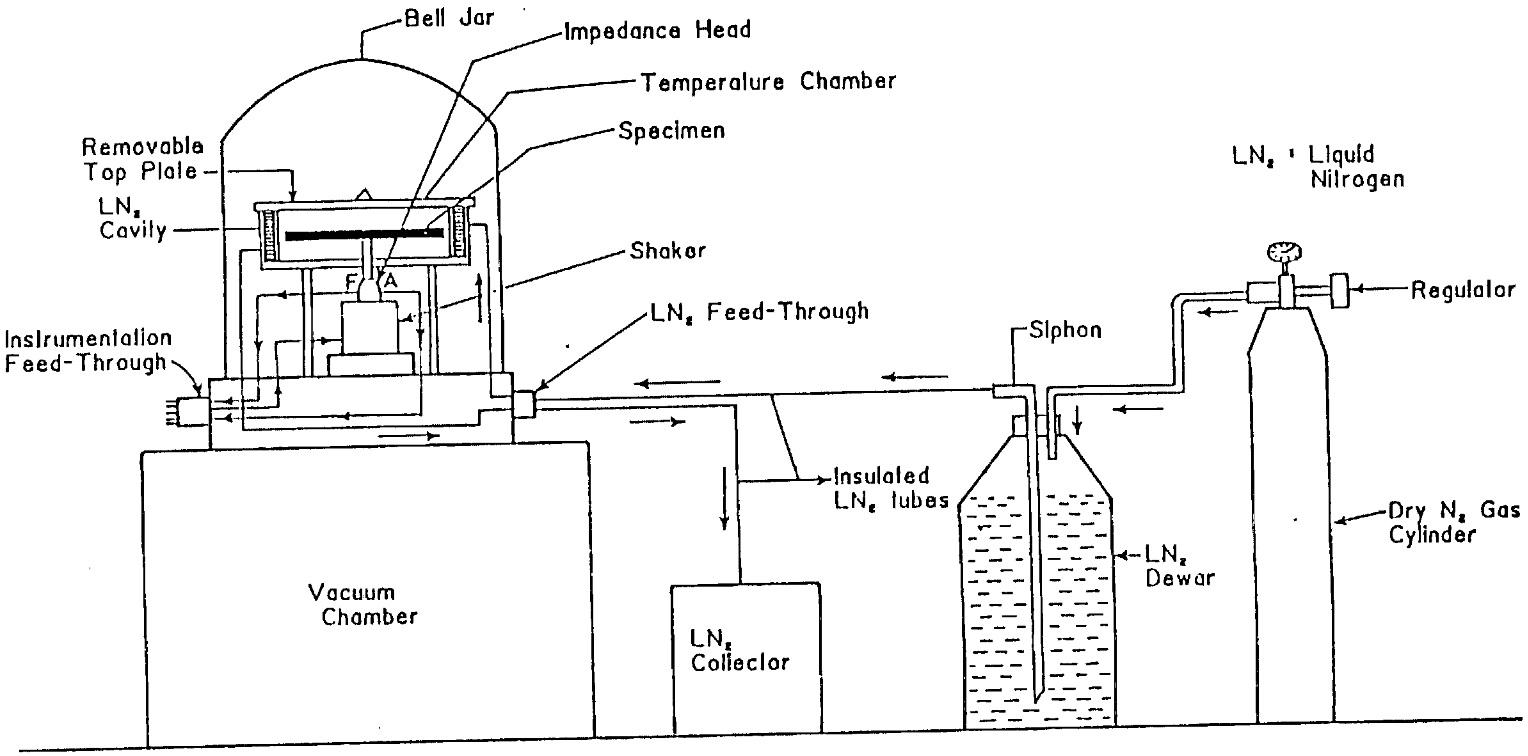

Figure 29. Experimental Set-up for Measuring Damping Under Low Temperatures

controlled by varying the pressure in the liquid nitrogen dewar. Dry nitrogen gas from a cylinder was sent into the dewar, increasing the pressure and thus forcing the liquid to flow out through the siphon into the chamber. The temperature in the chamber was controlled by adjusting the flow rate and also when required using the heating coil. All the hoses and tubes were insulated to minimize thermal losses. Efforts to maintain a vacuum and low temperature conditions inside the chamber were unsuccessful because of many experimental difficulties.

Hence all the experiments were conducted under atmospheric pressure. Experiments were done on the following four samples: 1) Graphite epoxy beam of dimensions 16.5 x 2.5 x 0.3 cm, 2) Graphite epoxy beam of dimensions 25.4 x 2.5 x 0.3 cm, 3) Aluminum beam of dimensions 25.4 x 2.5 x 0.3 cm and 4) Graphite epoxy beam of dimensions as in 1, with a simple lap joint having an overlap of 8.9 cm.

The procedure used in the experiment was as follows. The specimen was first carefully mounted inside the temperature chamber and was supported at the center by a steel rod as explained before. The force and acceleration signals from the impedance head were fed to the FFT Analyzer. First, damping measurements were made at atmospheric temperature. Then the sample was cooled to the desired temperature by feeding an appropriate amount of liquid nitrogen into the cooling chamber from the dewar. The temperature of the sample was monitored precisely by means of two chromel-alumel thermocouples attached at two different locations on the sample. The difference between the temperatures at the ends of the sample never exceeded 1 to 2°C during the experiment. The frequency response in terms of the receptance function (displacement/force) was measured on the FFT analyzer. Random signal excitation was used and 100 averages were taken for each measurement. The whole measurement process took only about 50 seconds. But more time was spent in achieving a stable temperature, since the temperature control was done manually by adjusting the rate of flow of liquid nitrogen. The experiments were quite consistent and the results were repeatable. The following paragraph describes the results.

Figures 30 and 31 show sample frequency response curves for the second specimen tested at temperatures of 24°C and -130°C respectively. The peak at 262 Hz corresponds to the first bending mode of vibration and the peak at 1330 Hz corresponds to the third bending mode. All the damping measurements were focused on these modes. It was not possible to excite even numbered modes since the beam was excited at its center which is a node point for even numbered modes.

Figures 32 through 36 show the variation of damping ratio with temperature for the four samples mentioned before. The curve-fitting method based on the half-power points method was used in each case to compute the damping ratio from the receptance plots. Figure 32 corresponds to the first graphite epoxy beam specimen. The damping ratio value of the sample was 0.23% at 24°C and was reduced to about half this value (0.12%) when the temperature was reduced to about -60°C. There was a small difference of 3 Hz in the modal frequency between the two readings. A somewhat similar trend can be found in the other plots as well. It is particularly clear from Figure 36 that there is a slow and gradual decrease in the damping ratio value from an atmospheric temperature to cryogenic temperatures. This is in agreement with some data available in the literature[66].

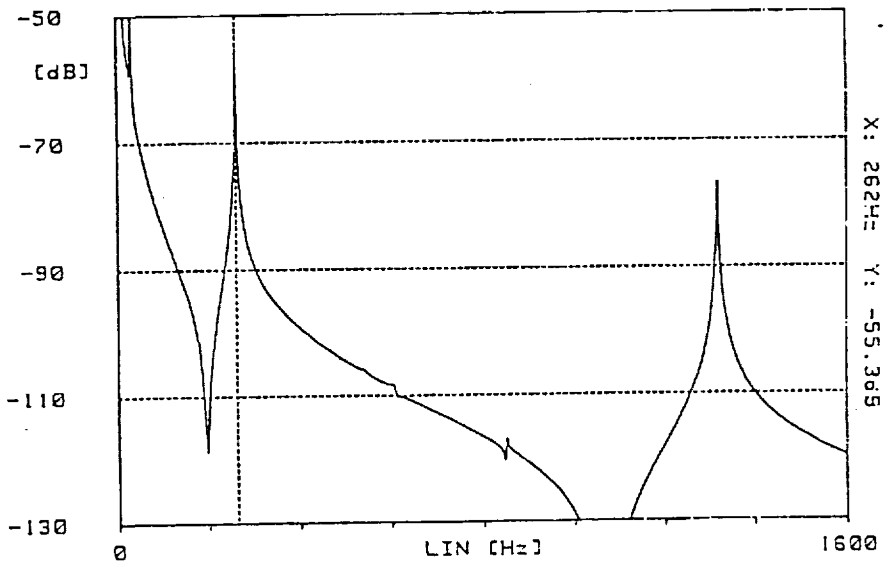

Figure 30. Frequency Response of the Graphite Epoxy Beam at Atmospheric Temperature

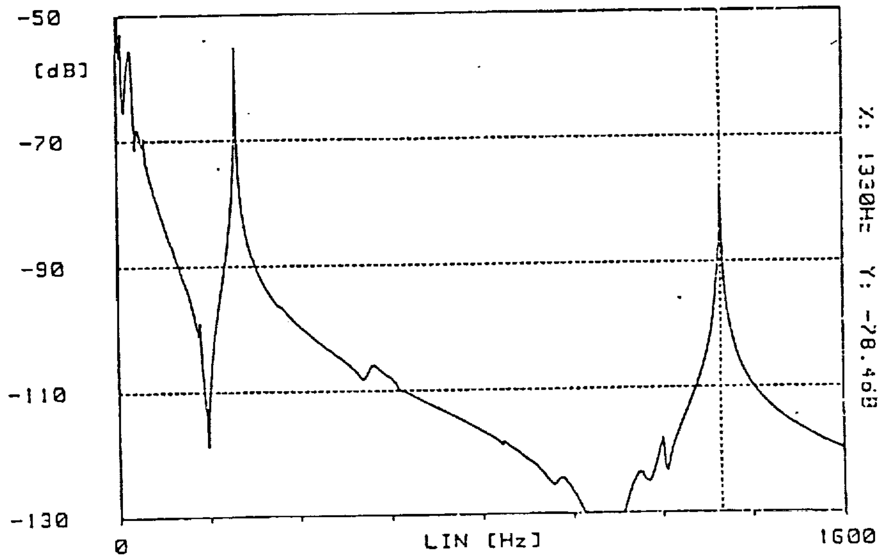

Figure 31. Frequency Response of the Graphite Epoxy Beam at -130^{0} C

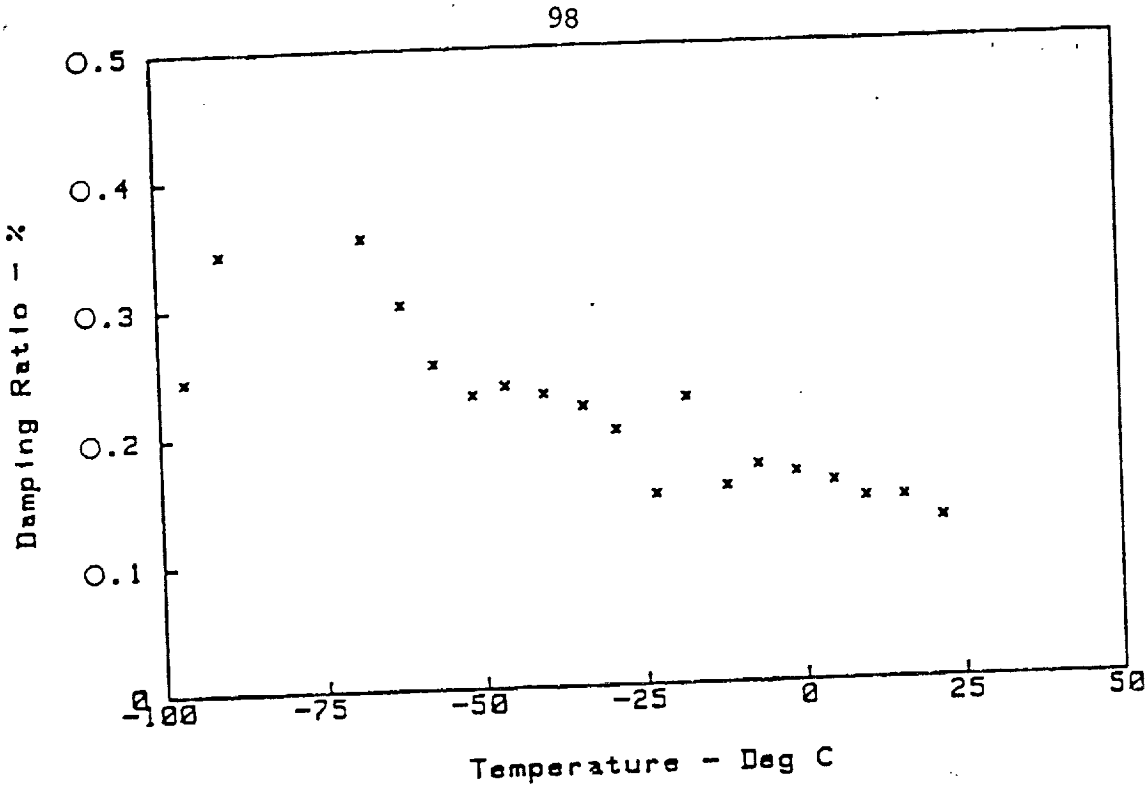

Figure 32. Plot of Damping Ratio of Graphite Epoxy Beam 1 vs. Temperatures Below Ambient

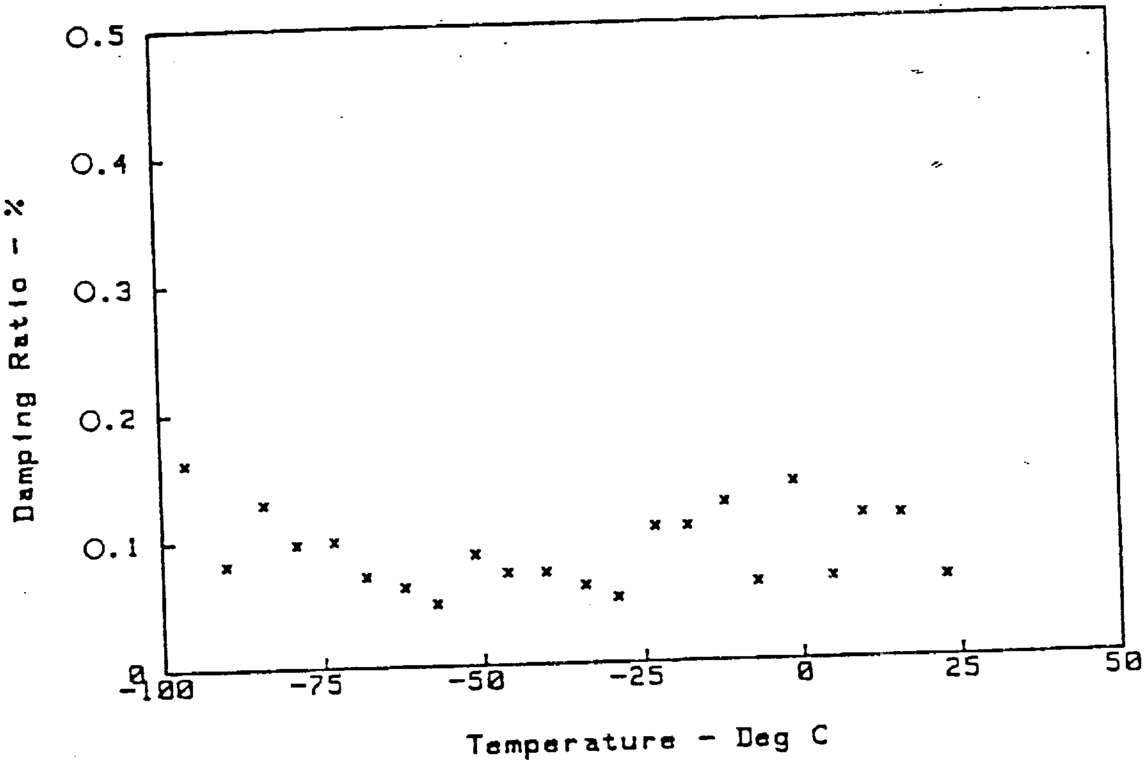

Figure 33. Plot of Damping Ratio of Graphite Epoxy Beam 2 vs. Temperatures Below Ambient (Mode 1)

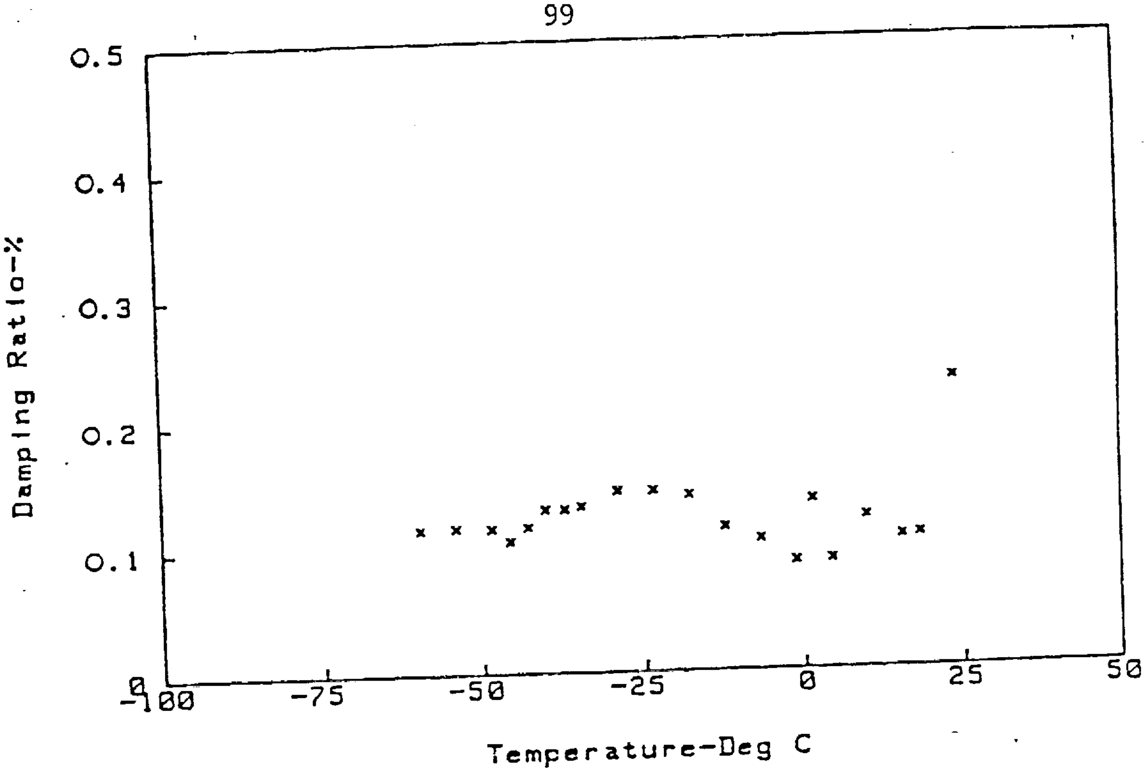

Figure 34. Plot of Damping Ratio of Graphite Epoxy Beam 2 vs. Temperatures Below Ambient (Mode 3)

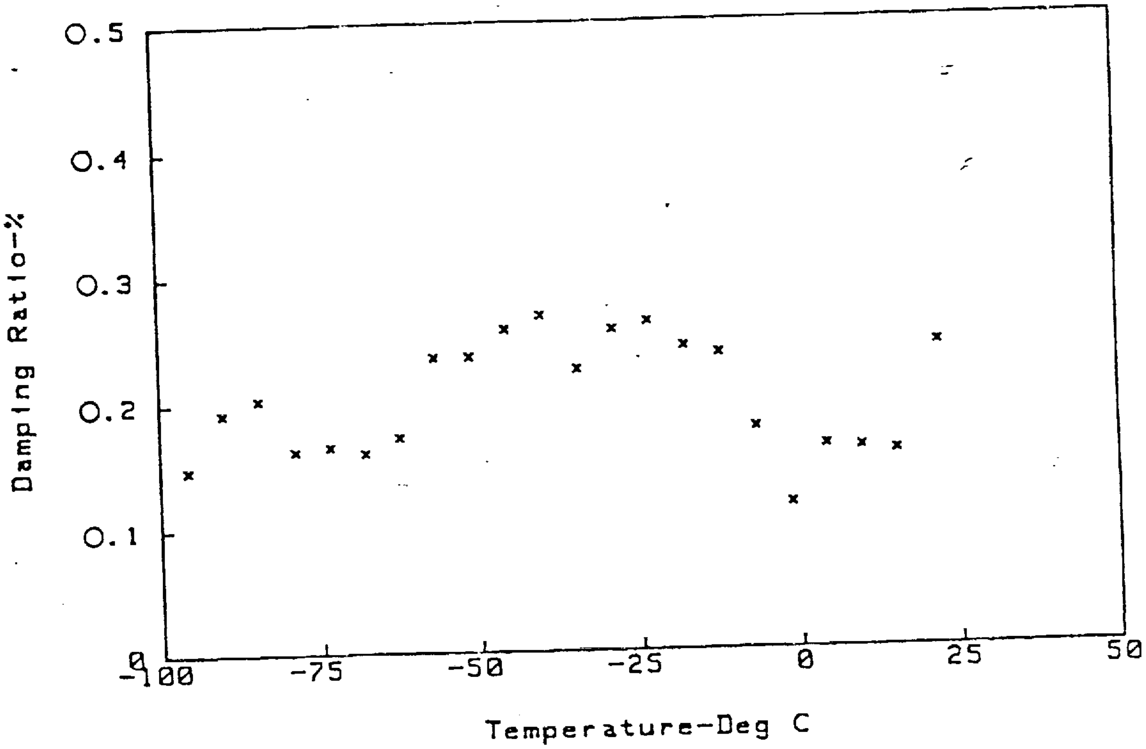

Figure 35. Plot of Damping Ratio of Aluminum Beam vs. Temperatures Below Ambient

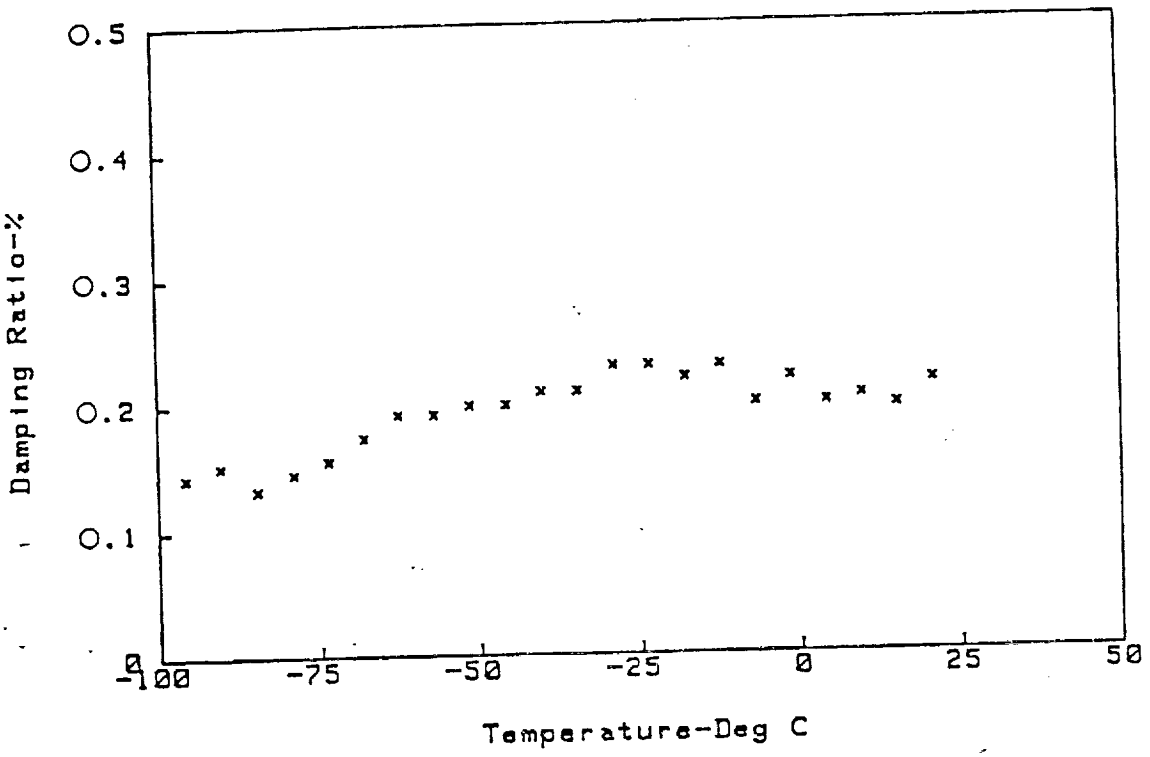

Figure 36. Plot of Damping Ratio of Stainless Steel Beam vs. Temperatures Below Ambient

V. DAMPING OF BONDED STRUCTURAL JOINTS

Structural adhesive bonding of composites to composites, as well as composites to metallic components, has developed rapidly due to advances in composite materials and adhesive bonding techniques. Structural composite bonded joints are primarily of the overlap type (single or double overlap). Scarf joints are structurally efficient, but are difficult or costly to manufacture. Butt joints although simple to process, are not considered for primary structural joints. This is because of their limited load carrying capacity due to the presence of cleavage stresses when the loading is not truly tensile. Angle joints are not usually preferred but are sometimes necessary. Tube joints are difficult and costly to manufacture.

The paper by Goland and Reissner [106] is regarded as a classic work in the area of static analysis of a simple lap joint. Goland and Reissner studied the stresses in bonded single lap joints for two different cases. In the first case, the bond layer was very thin and had no contribution to the joint flexibility. On the other hand, in the second case, the bond layer was so thick that it was the primary contributor to joint flexibility. In both cases, they derived equations for evaluating the shearing and normal stresses in the bond layer as well as those in the jointed plates. They found for equal thickness isotropic plates, that the bond layer shear stress has a nearly uniform distribution except for large concentrations near the ends of the joint. The peel stress (stress perpendicular to the bond layer) also had high values near the joint edges although not nearly as high as the inflexible bond case.

In the Goland and Reissner analysis, the peel and shear stresses were assumed constant across the adhesive thickness. In later works by Ojalvo and Eidinoff [107], Carpentor [108], Kline [109], attempts are made to incorporate a linear variation of these stresses across the thickness of the adhesive. Delale and Erdogan [110] have carried out the stress analysis of a bonded lap joint system assuming that the adherents are elastic and the adhesive is linearly viscoelastic. Renton and Vinson [111], and Delale, Erdogan, and Aydinoglu [112] have attempted to include anisotropic adherents in the mathematical model.

Hart-Smith [113-116] was the first investigator to advocate the use of continuum mechanics in the analysis of bonded joints. He has analyzed double-lap, single-lap, scarf, stepped-lap and tapered-lap configurations. Tensile, compressive and in-plane shear stresses in the system were considered based on an elastic-plastic analysis of the configuration. The author has also discussed joint efficiency and potential failure modes for each of the above configurations.

The above review indicates that much of the work done in this area has been confined to the static analysis of bonded joints. However, a lot of work has been done in the area of dynamics of sandwich beams and plates, consisting of a viscoelastic core material constrained between two elastic layers. The reader is referred to excellent review articles by Mead [117] and Nakra [118], for more information on this subject. Only recently, two papers have been published on the subject of vibrations of bonded joints. The one by Saito and Tani [119], deals with the vibrations of a bonded lap joint system and the other by Prucz [120] deals with a quasi-static analysis of a symmetrical double-lap configuration. The analytical model described by Prucz is similar to the one-dimensional model of Hart-Smith for the analysis of a fully elastic double lap joint. The author, however, has incorporated the viscoelastic behavior of the adhesive layers in the joint. A quasi-static analysis of constrained layer damping treatment is utilized to evaluate the joint damping properties. Saito and Tani [119] have derived equations for predicting the modal parameters of the coupled longitudinal and flexural vibrations of a system consisting of a pair of elastic beams lap-jointed over a certain length by a viscoelastic material. Numerical results are presented for the case of fixed-fixed boundary conditions at the ends. A simplified version of this model to include composite beams has been developed in the present investigation. The details of this analysis together with numerical and experimental results are presented in this chapter. Some experimental results on the damping of other types of bonded joints are also included in this chapter.

Analytical Modeling of the Flexural Vibrations of a Bonded Lap-Joint System

The system chosen for study is as shown in Figure 37. The objective is to arrive at a suitable mathematical model to evaluate the damping ratios and resonance frequencies of the system for free flexural vibration. The system consists of a pair of rectangular beams lap-jointed over a certain length. The bond between the two beams is achieved by means of an adhesive whose thickness is small compared with those of the beams. The unjointed ends of the beams may have any physically realizable boundary conditions, but, in this case are assumed to be simply-supported. Equations of motion are, first, derived assuming the beams to be made of composite materials using the complex modulus approach. The adhesive is assumed to be linearly viscoelastic and the widely used Kelvin-Voight model is used to represent the viscoelastic behavior of the adhesive. Both the complex modulus approach and the Kelvin Voight solid model approach are identical in that the constitutive relationship between stress and strain is similar to Hooke's law, but includes a complex rather than a real material constant. According to this approach, the deformation field induced in a material by a simple harmonic oscillating load contains an elastic or storage component, and a dissipative or loss component. This model is restricted to cyclic oscillations, and is believed to be closely associated with a simple physical interpretation of a viscoelastic behavior.

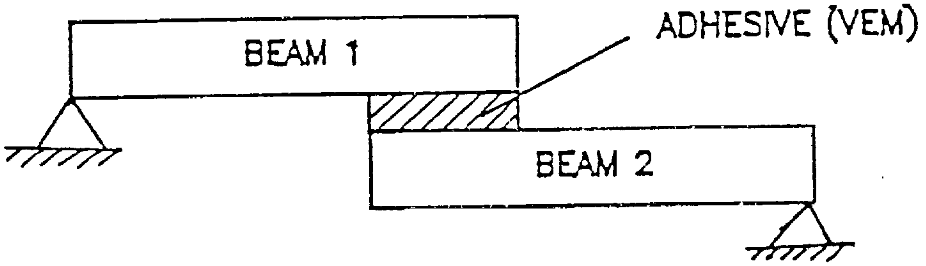

Figure 37. Two Parallel Beams with a Lap Joint

The starting point for the development of this model is the consideration of the dynamic equilibrium equations of the overlap (joint) region. The equations of motion in the joint region are derived using a differential element approach. The transverse displacements of the upper and the lower beams are considered to be different. The normal force between each beam and the adhesive layer is obtained from the Kelvin-Voight viscoelastic model of the adhesive. The shear force at the interface between the adhesive and the beam is obtained from the simple bending motion equations of the two beams. The resulting equations of motion are combined with the equations of transverse vibrations of the beams in the unjointed regions. These are later solved as a boundary value problem using a knowledge of the boundary conditions at the unjointed ends and motion continuity equations at the ends of the overlap. The eigenvalues and the eigenvectors of the system are obtained numerically by an iterative technique using a computer.

Derivation of the Mathematical Model

The system is hypothetically divided into three parts as shown in Figure 38. The coordinate system chosen for each part is also shown in the same figure.

Part 1 - Overlap Region

Although, this portion of the system is identical to a three-layer sandwich beam, the analysis here is somewhat different from that of a three-layer sandwich beam. This is because, in the vibration analysis of a three-layer sandwich beam, the displacements of the upper and lower beams are usually assumed to be identical. In the present case, however, the system configuration does not permit the inclusion of such an assumption. Several other assumptions are, however, made in the present analysis as follows: a) the analysis is carried out only for the free flexural vibrations of the system; the longitudinal and rotary inertia effects are neglected, b) there is no slip at the bond interfaces, c) all points on a plane normal to the longitudinal axis of the beam have the same transverse displacement, d) the longitudinal force in the adhesive layer may be neglected relative to those forces in the beams, e) since the thickness of the adhesive layer is small relative to the thickness of the beam, the mass (inertia) of the adhesive may be neglected, and the normal and shear forces in the adhesive are assumed to be constant.

A free-body diagram of a differential element of length dx of the composite three-layer part of the system is shown in Figure 39. N is the axial force in the beam, V represents the shear force in the beams, M is the bending moment in the beam, s is the shear force per unit length at the bond interfaces, and p is the transverse force per unit length between the beam and the adhesive. The above quantities with subscript 1 refer to the upper beam and subscript 2 refer to the lower beam. Furthermore, $y_1 = y_1(x,t)$ is the transverse displacement of the upper beam, and $y_2 = y_2(x,t)$ is that of the lower beam.

ANALYSIS

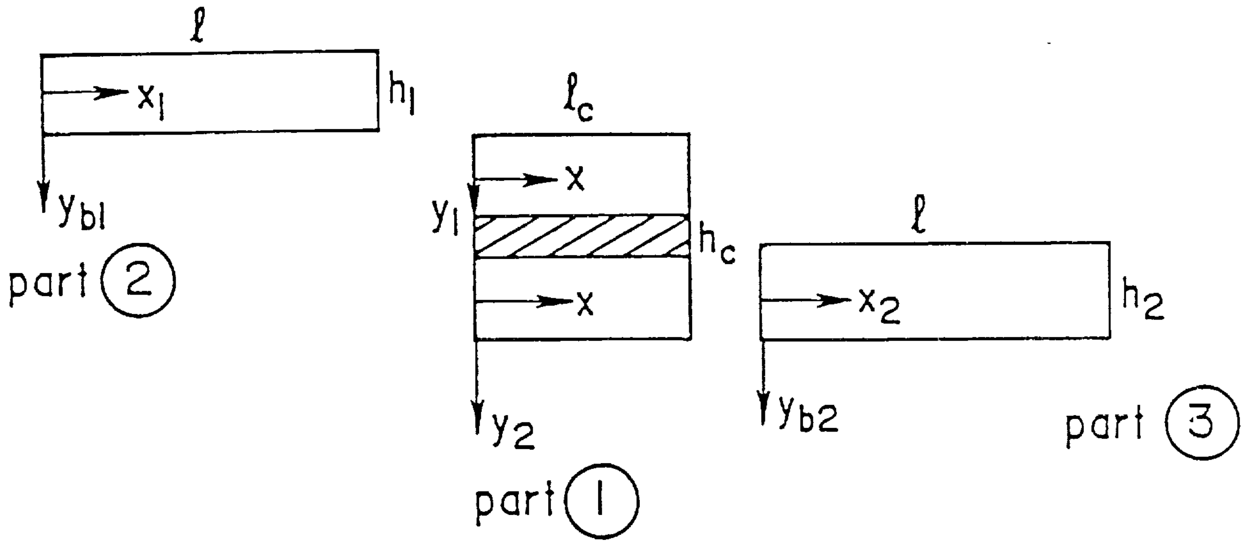

Figure 38. Hypothetical Division of the System Showing the Coordinates For Analysis

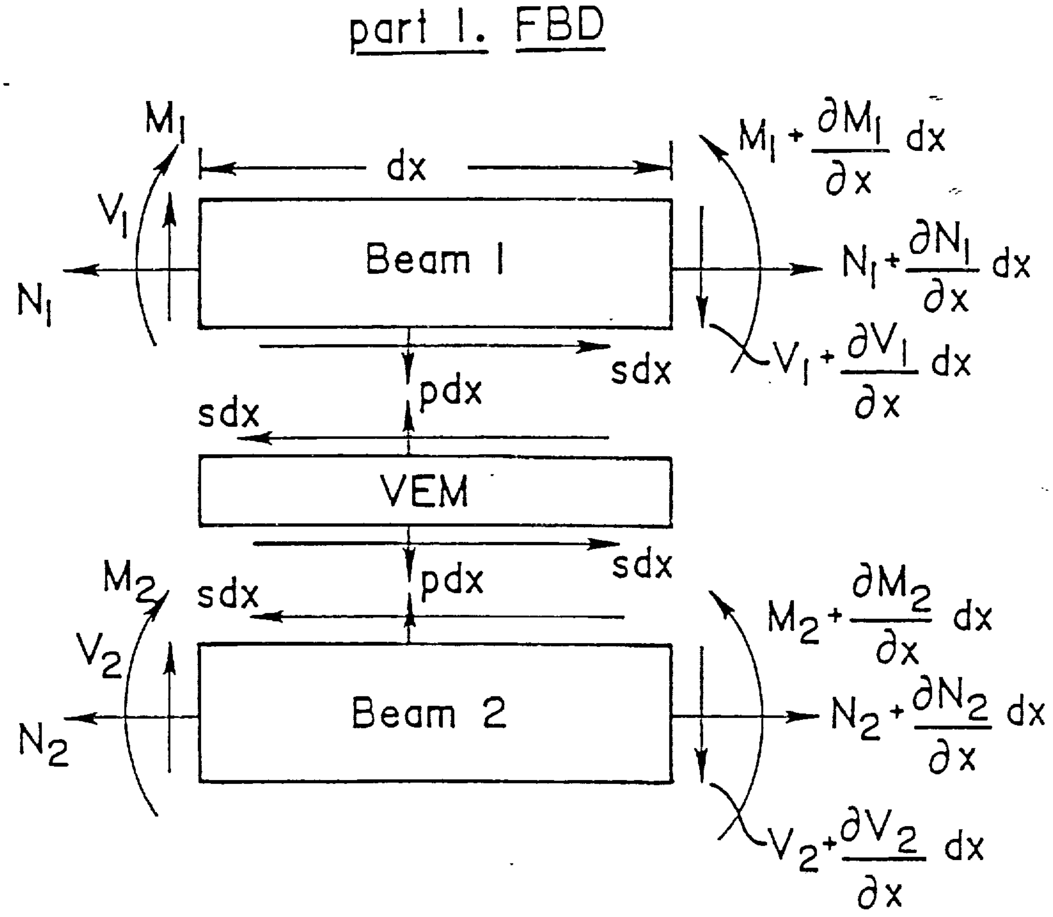

Figure 39. Free Body Diagram of a Differential Element in the Overlap Region

The sum of forces in the x-direction on beams 1 and 2 yields,

$$N_1 + \frac{\partial N_1}{\partial x} dx - N_1 + sdx = 0, \text{ and} \qquad (5.1)$$

$$N_2 + \frac{\partial N_2}{\partial x} dx - N_2 - sdx = 0. \qquad (5.2)$$

Equating the sum of forces in the y-direction to the corresponding inertia forces, we get for beam 1,

$$-V_1 + V_1 + \frac{\partial V_1}{\partial x} dx + pdx = \rho_1 A_1 dx \frac{\partial^2 y_1}{\partial t^2} , \qquad (5.3)$$

and for beam 2

$$-V_2 + V_2 + \frac{\partial V_2}{\partial x} dx - pdx = \rho_2 A_2 dx \frac{\partial^2 y_2}{\partial t^2} . \qquad (5.4)$$

The term ρA in Equations (5.3) and (5.4) is the mass per unit length, with ρ representing the density and A representing the cross sectional area of the beam. Summing the moments about the center of the right edge, for beam 1,

$$M_1 - (M_1 + \frac{\partial M_1}{\partial x} dx) - sdx \frac{h_1}{2} + V_1 dx = 0 , \qquad (5.5)$$

for beam 2,

$$M_2 - (M_2 + \frac{\partial M_2}{\partial x} dx) - sdx \frac{h_2}{2} + V_2 dx = 0 . \qquad (5.6)$$

The simplified versions of Equations (5.3) and (5.4) are:

$$\frac{\partial V_1}{\partial x} + p = \rho_1 A_1 \frac{\partial^2 y_1}{\partial t^2} , \qquad (5.7)$$

$$\frac{\partial V_2}{\partial x} - p = \rho_2 A_2 \frac{\partial^2 y_2}{\partial t^2} . \qquad (5.8)$$

Differentiating Equations (5.5) and (5.6) with respect to x, and simplifying we obtain,

$$\frac{\partial V_1}{\partial x} = \frac{\partial^2 M_1}{\partial x^2} + \frac{h_1}{2}\,\frac{\partial s}{\partial x}\,, \tag{5.9}$$

and

$$\frac{\partial V_2}{\partial x} = \frac{\partial^2 M_2}{\partial x^2} + \frac{h_2}{2}\,\frac{\partial s}{\partial x}\,. \tag{5.10}$$

From Equation (5.7) through (5.10), we have,

$$\frac{\partial^2 M_1}{\partial x^2} + \frac{h_1}{2}\,\frac{\partial s}{\partial x} + p = \rho_1 A_1\,\frac{\partial^2 y_1}{\partial t^2}\,, \tag{5.11}$$

and

$$\frac{\partial^2 M_2}{\partial x^2} + \frac{h_2}{2}\,\frac{\partial s}{\partial x} - p = \rho_2 A_2\,\frac{\partial^2 y_2}{\partial t^2}\,. \tag{5.12}$$

Equations (5.11) and (5.12) represent the equations of motion of the upper and lower beams respectively. From the classical theory of pure bending of beams, the bending moments M_1 and M_2 may be related to the corresponding transverse displacements, y_1 and y_2 through the flexural rigidity term EI, where E is the Young's modulus of the material of the beam, and I is the second moment of the cross-sectional area with respect to the centroidal axis. Noting that the y-axis is positive downwards, from beam theory,

$$M_1 = -\,E_1 I_1\,\frac{\partial^2 y_1}{\partial x^2} \text{ and } M_2 = -E_2 I_2\,\frac{\partial^2 y_2}{\partial x^2}\,. \tag{5.13}$$

It should be noted that Equation (5.13) is valid for elastic, homogeneous beams having a constant area of cross-section. It turns out, however, that an equation similar to the above can be written for the composite beams of the present problem, by simply replacing the real modulus by its complex counterpart. This analysis is valid only for harmonic time dependence [10]. With this in mind, we can write,

$$M_1 = -E_1^* I_1 \frac{d^2 y_1}{dx^2}, \text{ and } M_2 = -E_2^* I_2 \frac{d^2 y_2}{dx^2}, \qquad (5.14)$$

where $E_1^* = E_1 (1+i\alpha\omega)$, and $E_2^* = E_2 (1+i\beta\omega)$. (5.15)

α and β are some constants to be assumed depending on the material, and ω is the frequency, and $i = \sqrt{-1}$. The next objective is to find suitable expressions for p and s in terms of y_1 and y_2, so that Equations (5.11) and (5.12) can be solved.

Expression for p

As mentioned before, the adhesive layer is modeled as a Kelvin-Voight viscoelastic solid, because of the mathematical simplicity. A detailed derivation of a standard-linear model for a viscoelastic material and its reduction to a Kelvin-Voight model is shown in Appendix B. Accordingly, we can write,

$$p = K (y_1 - y_2) + c \left(\frac{\partial y_1}{\partial t} - \frac{\partial y_2}{\partial t}\right). \qquad (5.16)$$

K refers to the transverse stiffness per unit length, and c is the viscous damping coefficient. K may be related to the storage modulus E_c, the width b, and the thickness h_c of the adhesive by, $K = E_c b/h_c$.

Expression for s

The interfacial shear force s may be found by considering a small element of the viscoelastic layer as shown in Figure 40.

The element is deformed due to the axial displacements, u_1 and u_2 of the bonded surfaces of beams 1 and 2 respectively, caused by their bending moments. For small displacements, the shear stress τ, is related to shear strain in the adhesive by:

$$\tau = G_c\{ \frac{u_1 - u_2}{h_c} \} + \gamma \frac{\partial}{\partial t}\frac{(u_1 - u_2)}{h_c} . \qquad (5.17)$$

The expression on the right hand side excluding G_c is the shear strain. G_c is the real part of the shear modulus of the adhesive material. As before, γ is another constant which is included here to take care of the viscoelastic nature of the adhesive.

Assume that the axial deformations, u_1 and u_2 are caused only by the bending of the beams and that there are no external axial forces in the beams. Then, from the classical theory of pure bending of beams, it can be shown that,

$$u_1 = \frac{h_1}{2}\frac{\partial y_1}{\partial x} , \quad \text{and } u_2 = -\frac{h_2}{2}\frac{\partial y_2}{\partial x} \qquad (5.18)$$

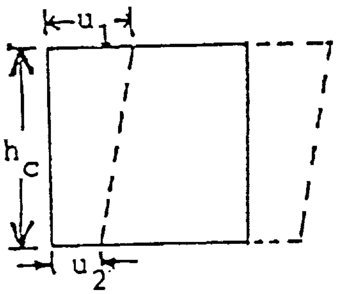

Figure 40. A Small Element of the Viscoelstic Layer

In deriving the above expressions, it is also assumed that the neutral axis of the upper beam always remains above that of the lower beam. Then,

$$u_1 - u_2 = \frac{h_1}{2}\frac{\partial y_1}{\partial x} + \frac{h_2}{2}\frac{\partial y_2}{\partial x}. \qquad (5.19)$$

From Equations (5.17) and (5.19), the interfacial shear force per unit length s is given by

$$s = \frac{G_c b}{2h_c}\left[\left(h_1\frac{\partial y_1}{\partial x} + h_2\frac{\partial y_2}{\partial x}\right) + \gamma\frac{\partial}{\partial t}\left(h_1\frac{\partial y_1}{\partial x} + h_2\frac{\partial y_2}{\partial x}\right)\right]. \qquad (5.20)$$

It is interesting to note here that for a simple harmonic time dependence of the form, $e^{i\omega t}$ for y_1 and y_2, Equations (5.16) and (5.20) can be written in a more familiar form as

$$p = K_c^* [y_1 - y_2], \text{ and} \qquad (5.21)$$

$$s = \frac{G_c^* b}{2h_c}\left[h_1\frac{dy_1}{dx} + h_2\frac{dy_2}{dx}\right], \qquad (5.22)$$

where, $K_c^* = K(1 + i\frac{c\omega}{K})$, and $G_c^* = G_c(1 + i\gamma\omega)$. (5.23)

K_c^* and G_c^* may be considered as the complex stiffness and complex shear modulus of the adhesive material respectively.

The next step is to obtain the final form of equations of motion (5.11) and (5.12) by making use of the relations developed so far for M_1, M_2, p and s. This is easily done by noting that $y_1 = Y_1 e^{i\omega t}$, and $y_2 = Y_2 e^{i\omega t}$, where Y_1 and Y_2 are now functions of x only. ω is the complex natural frequency, the real part ω_R representing the damped natural frequency and the ratio of the imaginary part ω_I to ω_R representing the modal loss factor η. The modal damping ratio ζ is simply equal to $\eta/2$. Now, from Equations (5.11), (5.14), (5.21) and (5.22), we obtain for the upper beam:

$$E_1^* I_1 \frac{d^4 Y_1}{dx^4} - \frac{G^* b h_1}{4h_c} [h_1 \frac{d^2 Y_1}{dx^2} + h_2 \frac{d^2 Y_2}{dx^2}] + K_c^* (Y_1 - Y_2) - \rho_1 A_1 \omega^2 Y_1 = 0, \tag{5.24}$$

and, similarly from Equations (5.12), (5.14), (5.21) and (5.22), we get for the lower beam:

$$E_2^* I_2 \frac{d^4 Y_2}{dx^4} - \frac{G_c^* b h_2}{4h_c} [h_1 \frac{d^2 Y_1}{dx^2} + h_2 \frac{d^2 Y_2}{dx^2}] - K_c^* (Y_1 - Y_2) - \rho_2 A_2 \omega^2 Y_2 = 0. \tag{5.25}$$

Here, $Y_1 = Y_1(x)$, $Y_2 = Y_2(x)$.

Equations (5.24) and (5.25) are coupled equations of motion of the system, the solution of which can be obtained by assuming a solution of the form $Y_1 = A_n e^{\lambda_n x}$, and $Y_2 = B_n e^{\lambda_n x}$.

Non-dimensionalization

The above equations of motion (5.24) and (5.25), should be expressed in a non-dimensional form so as to avoid overflow problems on the computer during the solution scheme. This is done in this section for the special case in which the two beams are assumed to be identical.

Let $E_1 = E_2 = E$, and $h_1 = h_2 = h$. The following non-dimensional parameters are used:

$$\bar{Y}_1 = \frac{Y_1}{\bar{h}}\ ,\ \bar{Y}_2 = \frac{Y_2}{\bar{h}}\ ,\ \bar{x} = \frac{X}{L}\ ,\ \bar{\ell} = \frac{\ell}{L}\ , \tag{5.26}$$

where $L = \ell + \ell_c$, ℓ = length of the beam and ℓ_c = length of the adhesive layer.

Also, let

$$\bar{G}_c = \frac{G_c}{E}\ ,\ \bar{E}_c = \frac{E_c}{E}\ ,\ \bar{h} = \frac{h}{L}\ ,\ \bar{\ell}_c = \frac{\ell_c}{L}\ . \tag{5.27}$$

The non-dimensional natural frequency is expressed as

$$\bar{\omega} = \frac{\omega}{\bar{\omega}_0},\ \text{where}\ \omega_0^2 = \frac{EI}{\rho A L^4}\ . \tag{5.28}$$

Using, Equations (5.26) through (5.28), Equations (5.24) and (5.25) written in non-dimensional form are:

$$\frac{d^4\bar{Y}_1}{d\bar{x}^4} - \frac{3\bar{G}_c^*}{\bar{h}\ \bar{h}_c}\left[\frac{d^2\bar{Y}_1}{d\bar{x}^2} + \frac{d^2\bar{Y}_2}{d\bar{x}^2}\right] + \frac{12\ \bar{E}_c^*}{\bar{h}_c\ \bar{h}^3}(\bar{Y}_1 - \bar{Y}_2) - \bar{\omega}^2\ \bar{Y}_1 = 0, \tag{5.29}$$

and

$$\frac{d^4\bar{Y}_1}{d\bar{x}^4} - \frac{3\bar{G}_c^*}{\bar{h}\ \bar{h}_c}\left[\frac{d^2\bar{Y}_1}{d\bar{x}^2} + \frac{d^2\bar{Y}_2}{d\bar{x}^2}\right] - \frac{12\ \bar{E}_c^*}{\bar{h}_c\ \bar{h}^3}(\bar{Y}_1 - \bar{Y}_2) - \bar{\omega}^2\ \bar{Y}_2 = 0, \tag{5.30}$$

$$\text{Here, }\ \bar{E}_c^* = \frac{E_c(1+i\eta_2)}{E(1+i\eta_1)}\ ,\ \text{and}\ \bar{G}_c^* = \frac{G_c(1+i\eta_3)}{E(1+i\eta_1)}. \tag{5.31}$$

η_1 may be considered as the modal loss factor of the beam material, and η_2 and η_3 as the modal loss factors of the adhesive material in bending and shearing motions respectively. η_1, η_2 and η_3 may be assumed suitably depending on the material, while computing the eigenvalues and eigenvectors for each mode.

As mentioned before, Equations (5.29) and (5.30) can be decoupled by a series solution of the form

$$\bar{Y}_1 = A_n e^{\lambda_n \bar{x}} \text{ , and } \bar{Y}_2 = B_n \, e^{\lambda_n \bar{x}} \text{ ,} \qquad (5.32)$$

where A_n and B_n are constants to be determined from the boundary conditions.

Substituting Equation (5.32) in (5.29) and (5.30), we obtain,

$$\lambda_n^4 \, A_n - \frac{3\bar{G}_c^*}{\bar{h}\,\bar{h}_c} [\, \lambda_n^2 \, A_n + \lambda_n^2 \, B_n] - \frac{12\bar{E}_c^*}{h_c \, \bar{h}^3} [B_n - A_n] - \bar{\omega}^2 \, A_n = 0 \qquad (5.33)$$

$$\lambda_n^4 \, B_n - \frac{3\bar{G}_c^*}{\bar{h}\,\bar{h}_c} [\, \lambda_n^2 \, A_n + \lambda_n^2 \, B_n] - \frac{12\bar{E}_c^*}{hc \, \bar{h}^3} [B_n - A_n] - \bar{\omega}^2 \, B_n = 0 \qquad (5.34)$$

The above equations written in a matrix form:

$$\begin{bmatrix} (\lambda_n^4 - C_1 \lambda_n^2 + C_2 - \bar{\omega}^2) & -(C_1 + C_2) \\ -(C_1 + C_2) & (\lambda_n^4 - C_1 \lambda_n^2 + C_2 - \bar{\omega}^2) \end{bmatrix} \begin{bmatrix} A_n \\ B_n \end{bmatrix} \qquad (5.35)$$

$$\text{where, } C_1 = \frac{3\,\overline{G}_c^*}{\overline{h}_c\,\overline{h}}\,, \qquad C_2 = \frac{12\,\overline{E}_c^*}{\overline{h}_c\,\overline{h}^3}\,. \tag{5.36}$$

For a non-trivial solution, the determinant of the above matrix set equal to zero yields eight roots of λ, i.e.,

$$(\lambda_n^4 - C_1\lambda_n^2 + C_2 - \overline{\omega}^2)^2 - (C_1 + C_2)^2 = 0. \tag{5.37}$$

This can be simplified as

$$(\lambda_n^4 - C_1\lambda_n^2 + 2\,C_2 + C_1 - \overline{\omega}^2) = 0 \tag{5.38}$$

and

$$(\lambda_n^4 - C_1\lambda_n^2 - \overline{\omega}^2 - C_1) = 0\,. \tag{5.39}$$

Equations (5.38) and (5.39) each yield four unique roots for λ. Furthermore, from the above matrix, the constants A_n and B_n are related by:

$$B_n = \phi_n\,A_n,$$

where,

$$\phi_n = \left[\frac{\lambda_n^4 - C_1\lambda_n^2 + C_2 - \overline{\omega}^2}{C_1 + C_2}\right]. \tag{5.40}$$

Finally, we have

$$\overline{Y}_1 = \sum_{n=1}^{8} A_n\,e^{\lambda_n \overline{x}}\,, \tag{5.41}$$

and

$$\bar{Y}_2 = \sum_{n=1}^{8} \phi_n A_n \, e^{\lambda_n \bar{x}} \, . \qquad (5.42)$$

Equations (5.41) and (5.42) now have only eight constants to be determined by applying the boundary and continuity conditions as described later in this chapter.

Analysis of Parts 2 and 3

The differential equations of motion for the transverse vibration of the beam portions of the system as shown in Figure 38 are:

$$D_j \frac{\partial^4 y_{bj}}{\partial x_j^4} + \rho_j A_j \frac{\partial^2 y_{bj}}{\partial t^2} = 0 \, , \qquad j = 1,2. \qquad (5.43)$$

For the special case of identical beams,

$D_1 = D_2 = E^* I$, and $\rho_1 A_1 = \rho_2 A_2 = \rho A$.

Assuming $y_{bj} = Y_{bj}(x) \, e^{i\omega t}$, $j=1,2$, Equation (5.43) becomes

$$\frac{d^4 Y_{bj}}{dx_j^4} - \left(\frac{\rho A}{E^* I}\right) \omega^2 \, Y_{bj} = 0, \; j = 1,2. \qquad (5.44)$$

In non-dimensional form,

$$\frac{d^4 \bar{Y}_{bj}}{d\bar{x}_j^4} - \bar{\omega}^2 \, \bar{Y}_{bj} = 0, \; j = 1,2 \, . \qquad (5.45)$$

The solutions of the above equations are obtained, as before by assuming a series solution of the form:

$$\overline{Y}_{b1} = \sum_{i=1}^{4} C_n \, e^{\beta_n \overline{x}} \, , \quad \text{and} \quad \overline{Y}_{b2} = \sum_{i=1}^{4} D_n \, e^{\beta_n \overline{x}} \, , \qquad (5.46)$$

where $\beta_n^4 = \overline{\omega}^2$, and C_n and D_n are constants to be found from the boundary conditions.

Equations (5.41), (5.42), and (5.46) have 16 unknown constants. The following boundary and continuity conditions are applied to determine those constants and to obtain the frequency equation.

Boundary Conditions

Considering simply-supported boundaries at the un-jointed ends of the two beams, at points 1 and 2 (see Figure 41), the transverse displacement and bending moment are zero.

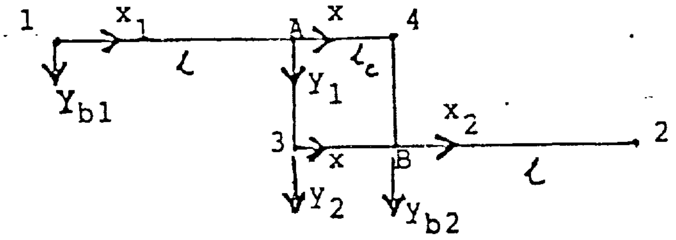

Figure 41. Illustration of the Locations of Boundary and Continuity Conditions

i.e., a) at $\bar{x}_1 = 0, \quad \bar{Y}_{b1} = 0, \quad \text{and} \quad \frac{d^2\bar{Y}_{b1}}{d\bar{x}_1^2} = 0, \qquad (5.47)$

b) at $\bar{x}_2 = \bar{\ell}, \quad \bar{Y}_{b2} = 0, \quad \text{and} \quad \frac{d^2\bar{Y}_{b2}}{dx_2^2} = 0. \qquad (5.48)$

Next, points 3 and 4 are free ends. Hence, the bending moments there are zero. Furthermore, the shear force at these points can be obtained from Equation (5.22). Hence, we obtain,

c) at $\bar{x} = 0$ (point 3),

$$\frac{d^2\bar{Y}_2}{d\bar{x}^2} = 0, \text{ and } \frac{d^3\bar{Y}_2}{d\bar{x}^3} = \frac{6\bar{G}_c^*}{\bar{h}^2}\left[\frac{d\bar{Y}_1}{d\bar{x}} + \frac{d\bar{Y}_2}{d\bar{x}}\right], \qquad (5.49)$$

d) at $\bar{x} = \bar{\ell}_c$ (point 4),

$$\frac{d^2\bar{Y}_1}{d\bar{x}^2} = 0, \text{ and } \frac{d^3\bar{Y}_1}{d\bar{x}^3} = \frac{6\bar{G}_c^*}{\bar{h}^2}\left[\frac{d\bar{Y}_1}{d\bar{x}} + \frac{d\bar{Y}_2}{d\bar{x}}\right]. \qquad (5.50)$$

Continuity Conditions

Referring to Figure 41, at points A and B, we equate the displacements, slopes, bending moments, and shear forces for the two hypothetical sections of the beams. These are mathematically expressed as:

At $\bar{x}_1 = \bar{\ell}$ and $\bar{x} = 0$ (point A),

$$\bar{Y}_1 = \bar{Y}_{b1} ,$$

$$\frac{d\bar{Y}_1}{d\bar{x}} = \frac{d\bar{Y}_{b1}}{d\bar{x}_1} ,$$

$$\frac{d^2\bar{Y}_1}{d\bar{x}^2} = \frac{d^2\bar{Y}_{b1}}{d\bar{x}_1^2} , \tag{5.51}$$

$$\frac{d^3\bar{Y}_1}{d\bar{x}^3} = \frac{d^3\bar{Y}_{b1}}{d\bar{x}_1^3} .$$

At $\bar{x}_2 = 0$ and $\bar{x} = \bar{\ell}_c$ (point B)

$$\bar{Y}_2 = \bar{Y}_{b2} ,$$

$$\frac{d\bar{Y}_2}{d\bar{x}} = \frac{d\bar{Y}_{b2}}{d\bar{x}_2} ,$$

$$\frac{d^2\bar{Y}_2}{d\bar{x}^2} = \frac{d^2\bar{Y}_{b2}}{d\bar{x}_2^2} , \tag{5.52}$$

$$\frac{d^3\bar{Y}_2}{d\bar{x}^3} = \frac{d^3\bar{Y}_{b2}}{d\bar{x}_2^3} .$$

Equations (5.47) through (5.52) yield 16 equations containing the 16 unknowns, viz., A_1, A_2, . . . A_8, C_1, C_2 . . . C_4, and D_1, D_2, . . . D_4. These equations can be expressed in matrix form as:

$$\begin{bmatrix} \\ \\ \text{16 x 16} \\ \text{complex matrix} \\ D \\ \\ \\ \end{bmatrix} \begin{bmatrix} A_1 \\ \bullet \\ \bullet \\ A_8 \\ C_1 \\ \bullet \\ \bullet \\ C_4 \\ D_1 \\ \bullet \\ \bullet \\ D_4 \end{bmatrix} = 0 \; . \tag{5.53}$$

The elements d_{ij} of the matrix D can be written in groups as follows:

1) $d_{ij} = 0$ for $i = 1 \ldots 4$ and $j = 1 \ldots 8$

$i = 1,2$ and $j = 13 \ldots 16$

$i = 3,4$ and $j = 9 \ldots 12$

$i = 5 \ldots 8$ and $j = 9 \ldots 16$

$i = 9 \ldots 12$ and $j = 13 \ldots 16$

$i = 13 \ldots 16$ and $j = 9 \ldots 12$

2) $d_{ij} = 1$ for $i = 1$ and $j = 9 \ldots 12$

for $i = 9$ and $j = 1 \ldots 8$

$d_{ij} = -1$ for $i = 13$ and $j = 13 \ldots 16$

3) $d_{2j} = \beta^2_{j-8}$ for $j = 9 \ldots 12$

4) $d_{3j} = e^{\beta_{j-12}\bar{\ell}}$ for $j = 13 \ldots 16$

5) $d_{4j} = \beta^2_{j-12}\, d_{3j}$ for $j = 13 \ldots 16$

6) $d_{5j} = \phi_j \lambda_j^2$ for $j = 1 \ldots 8$

7) $d_{6j} = [\phi_j \lambda_j^3 - \frac{6\bar{G}_c^*}{\bar{h}^2} (1+\phi_j)\lambda_j]$ for $j = 1 \ldots 8$

8) $d_{7j} = \lambda_j^2 \; e^{\lambda_j \bar{\ell}_c}$ for $j = 1 \ldots 8$

9) $d_{8j} = [\lambda_j^3 - \frac{6\bar{G}_c^*}{\bar{h}^2}(1 + \phi_j)\lambda_j]e^{\lambda_j \bar{\ell}_c}$ for $j = 1 \ldots 8$

10) $d_{10j} = \lambda_j$ for $j = 1 \ldots 8$

11) $d_{11j} = \lambda_j^2$ for $j = 1 \ldots 8$

12) $d_{12j} = \lambda_j^3$ for $j = 1 \ldots 8$

13) $d_{13j} = \phi_j e^{\lambda_j \bar{\ell}_c}$ for $j = 1 \ldots 8$

14) $d_{14j} = \lambda_j d_{13j}$ for $j = 1 \ldots 8$

15) $d_{15j} = \lambda_j^2 \, d_{13j}$ for $j = 1 \ldots 8$

16) $d_{16j} = e^{\lambda_j \bar{\ell}_c} \, d_{6j}$ for $j = 1 \ldots 8$

17) $d_{9j} = -e^{\beta_{j-8}\bar{\ell}}$ for $j = 9 \ldots 12$

18) $d_{10j} = \beta_{j-8} d_{9j}$ for $j = 9 \ldots 12$

19) $d_{11j} = \beta^2_{j-8} d_{9j}$ for $j = 9 \ldots 12$

20) $d_{12j} = \beta^3_{j-8} d_{9j}$ for $j = 9 \ldots 12$

21) $d_{14j} = -\beta_{j-12}$ for $j = 13 \ldots 16$

22) $d_{15j} = -\beta^2_{j-12}$ for $j = 13 \ldots 16$

23) $d_{16j} = -\beta^3_{j-12}$ for $j = 13 \ldots 16$

The determinant of the above matrix D, set equal to zero gives the frequency equation, i.e., for a non-trivial solution,

$$\text{Det } [D]_{16\times16} = 0. \qquad (5.54)$$

The roots of Equation (5.54) yield the complex natural frequencies (ω_ns) of the system.

$$\bar{\omega}_{nj} = \bar{\omega}_{Rj} + i\,\bar{\omega}_{Ij},$$

where j = 1, 2, . . . represents the mode number.

ω_{Rj} = modal resonance frequency, and

$\eta_j = \dfrac{\omega_{Ij}}{\omega_{Rj}}$ = modal loss factor.

Once the eigenvalues are evaluated, the corresponding eigenvectors needed to plot the mode shapes can be found by using any 15 of Equations (5.53) with one arbitrary constant.

Solution Procedure

The solution of Equation (5.54) was obtained numerically on a computer using an iteration method. A computer program has been developed on a Harris 800 system to obtain numerical solutions.

The complex eigenvalues $(\omega_R + i\,\omega_i)$ are solutions of the complex equation

$$D_R(\bar{\omega}_R + i\bar{\omega}_i) + i\,D_I(\bar{\omega}_R + i\,\bar{\omega}_i) = 0, \qquad (5.55)$$

where D_R and D_I are the real and imaginary parts of the determinant of the matrix D. The inputs to the program are the material constants and relevant geometric quantities expressed in non-dimensional forms, namely, $\bar{h}$, $\bar{h}_c$, $\bar{E}_c$, $\bar{G}_c$, η_1, η_2 and η_3. The solution procedure is as follows: Choose some initial value of $\bar{\omega}$, and compute the roots of $\beta_n^4 = \bar{\omega}^2$, and also find all of the λ_n by solving Equations (5.38) and (5.39). Construct the 16x16 complex D matrix and check to see whether

Equation (5.55) is satisfied. If not increment $\bar{\omega}$ and repeat the entire process till a zero crossing for the value of the determinant D is obtained.

The solution for the undamped system (i.e., $D_R(\omega_R) = 0$) is a good starting point for numerical iteration. This solution can later be used as an approximate solution for, $D_R(\omega_R+i0) + i\ D_i(\omega_R + i0) = 0$, and iteration is carried out by a bracketing method to arrive at the complex eigenvalue.

Numerical Results and Discussion

The length and thickness of the graphite epoxy beams chosen here for study were: $\ell = 12.25$ cm and $h = 0.25$ cm. The storage modulus of the beam material as supplied by the manufacturer was 124 Gpa. The material loss factor of the beam was taken as $\eta_1 = 0.004$, which was assumed to be a constant for all the modes. This corresponds to a damping ratio of 0.2% and is believed to represent closely the material damping of the graphite epoxy material as found from various experiments described previously in Chapter 3. The thickness of the adhesive layer was taken as 0.5 cm. The complex modulus of the adhesive material, which is epoxy resin in the present case was assumed to be 4(1+i0.04) Gpa which has a real part of 4 Gpa as supplied by the manufacturer. The complex shear modulus of the adhesive is assumed to be 1.4(1+i0.04) Gpa. Here $\eta_2 = \eta_3 = 0.04$, which corresponds to a constant damping ratio of 2% for the epoxy material.

The above quantities expressed in non-dimensional form were used in the numerical computation of the eigenvalues and eigenvectors. The ratio of the length of overlap to the beam length is called the overlap ratio. The Numerical results were obtained for overlap ratios of 0.2, 0.4, 0.6, and 0.8. Figure 42 shows the variation of natural frequency with overlap ratio for the first three modes of vibration. From this plot, it is clear that the natural frequency of the system increases with an increase in the overlap ratio for all modes. Figure 43 is a similar plot showing the variation of the system damping (total loss factor of the system) with overlap ratio. For the case of overlap ratio = 0.2, the non-dimensional frequencies $\bar{\omega}$ are: 2.86, 13.12, and 27.24 for the first three modes. The corresponding system damping ratios are ζ_1, = 0.534%, ζ_2 = 0.120%, and ζ_3 = 0.054%. It should be noted that the above values were obtained by assuming constant values of 0.2% and 2.0% for the material damping of the beam and the adhesive respectively. It is seen that, for this case, the system damping is higher than the material damping of the beam only for the first mode. For the other two modes, the system damping ratio appears to be lower than the material damping of the beam. This observation, however, is true only for the above case and cannot be generalized. To substantiate this point, let us consider a different case in which the damping ratio of the adhesive was assumed to be 5%, and the material damping of the beam was kept the same. The system damping ratios computed for this case are: ζ_1 = 1.66%, ζ_2 = 0.33%, and ζ_3 = 0.16%. There were no significant changes in the natural frequencies of the system. As can be seen, the system damping ratios in this case are totally different from the previous case considered. Hence, in order to predict the system damping ratios, using the present model, accurate knowledge about the material damping ratios (of the beam and adhesive) and their dependence on frequency is mandatory.

Figures 44 through 46 show the predicted mode shapes of the first three bending modes for different overlap ratios. These were obtained by solving the homogeneous algebraic Equations (5.53) for each eigenvalue.

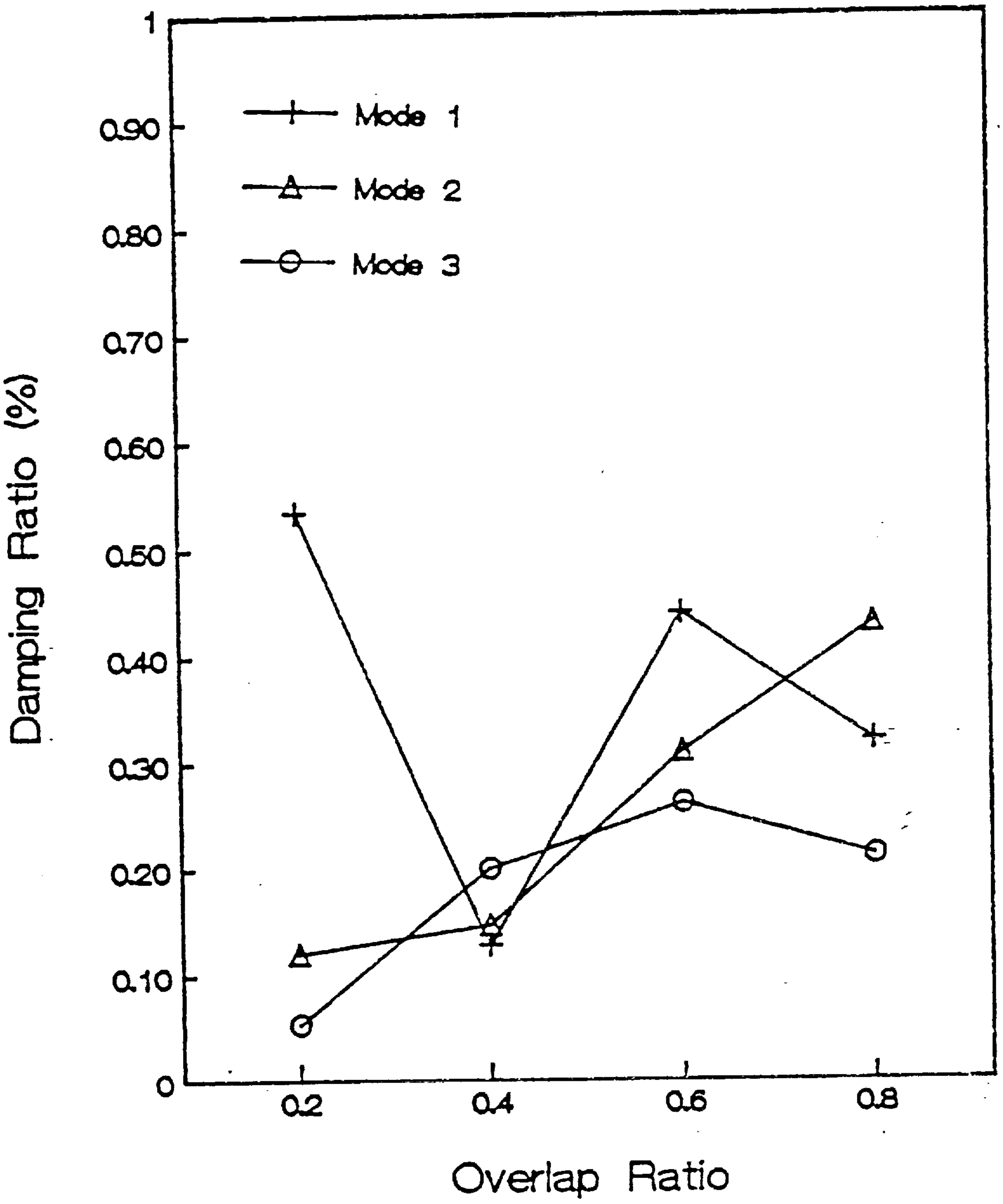

Figure 42. Plot of Natural Frequency vs. Overlap Ratio

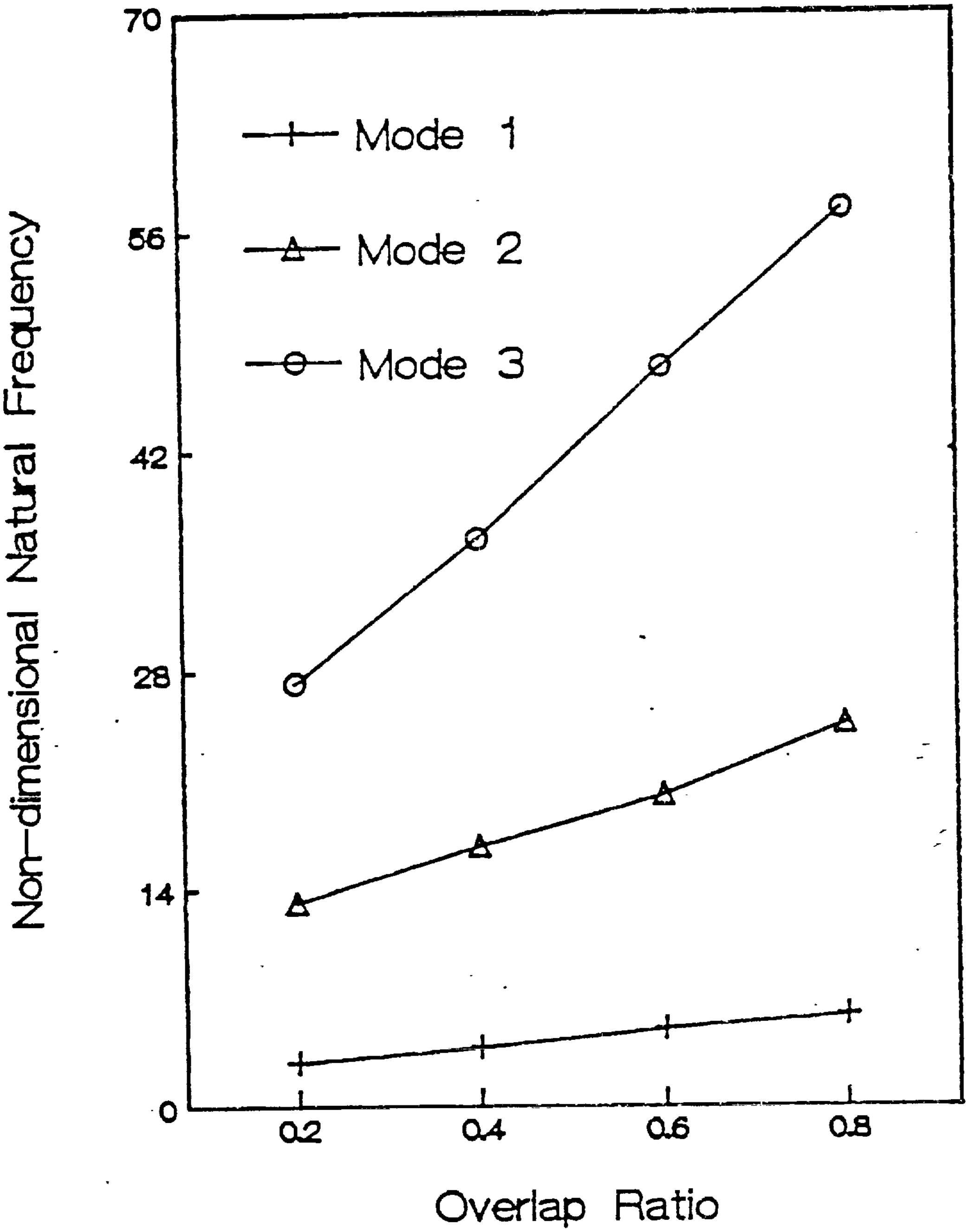

Figure 43. Plot of Damping Ratio vs. Overlap Ratio

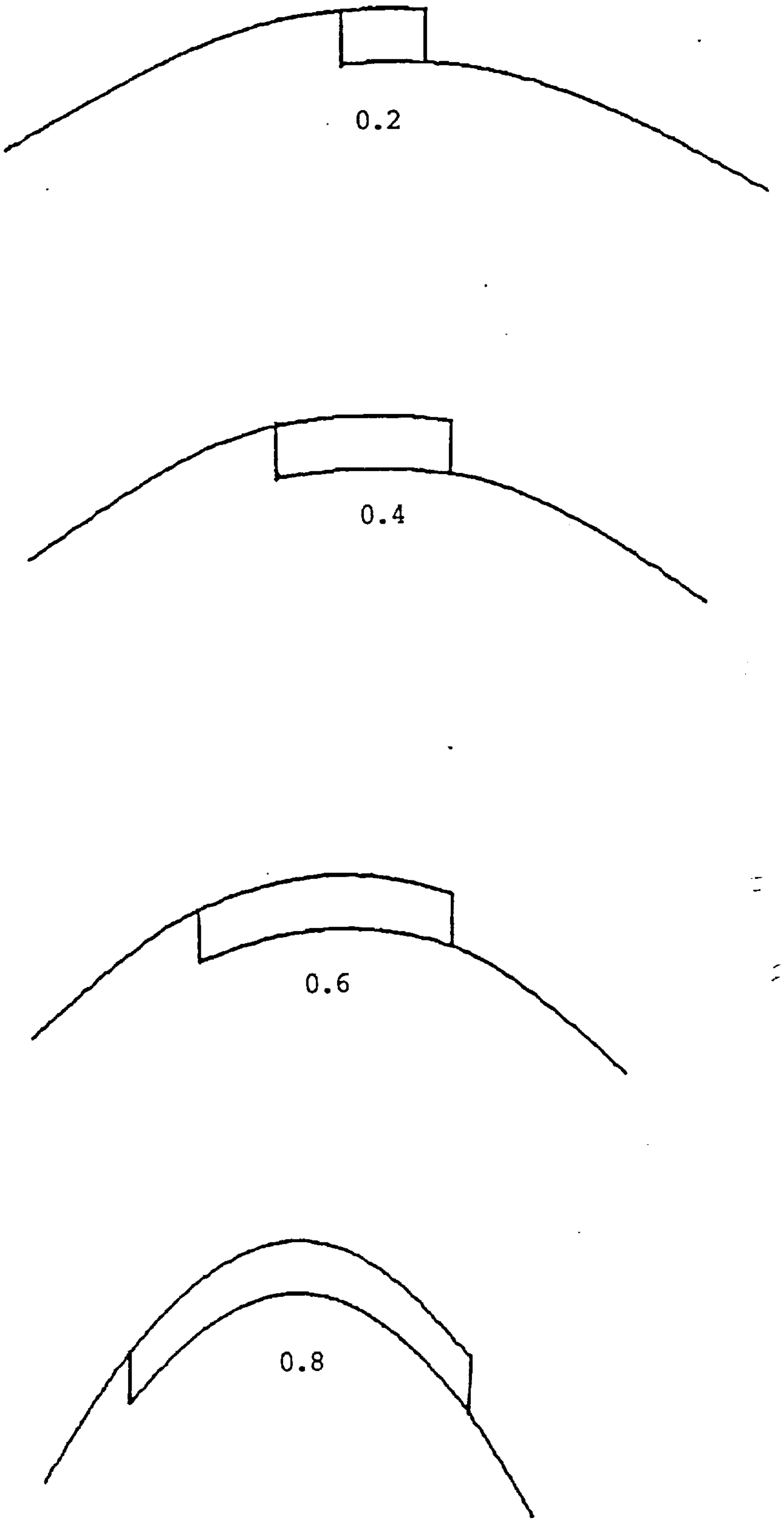

Figure 44. Theoretical Mode Shapes For Mode 1

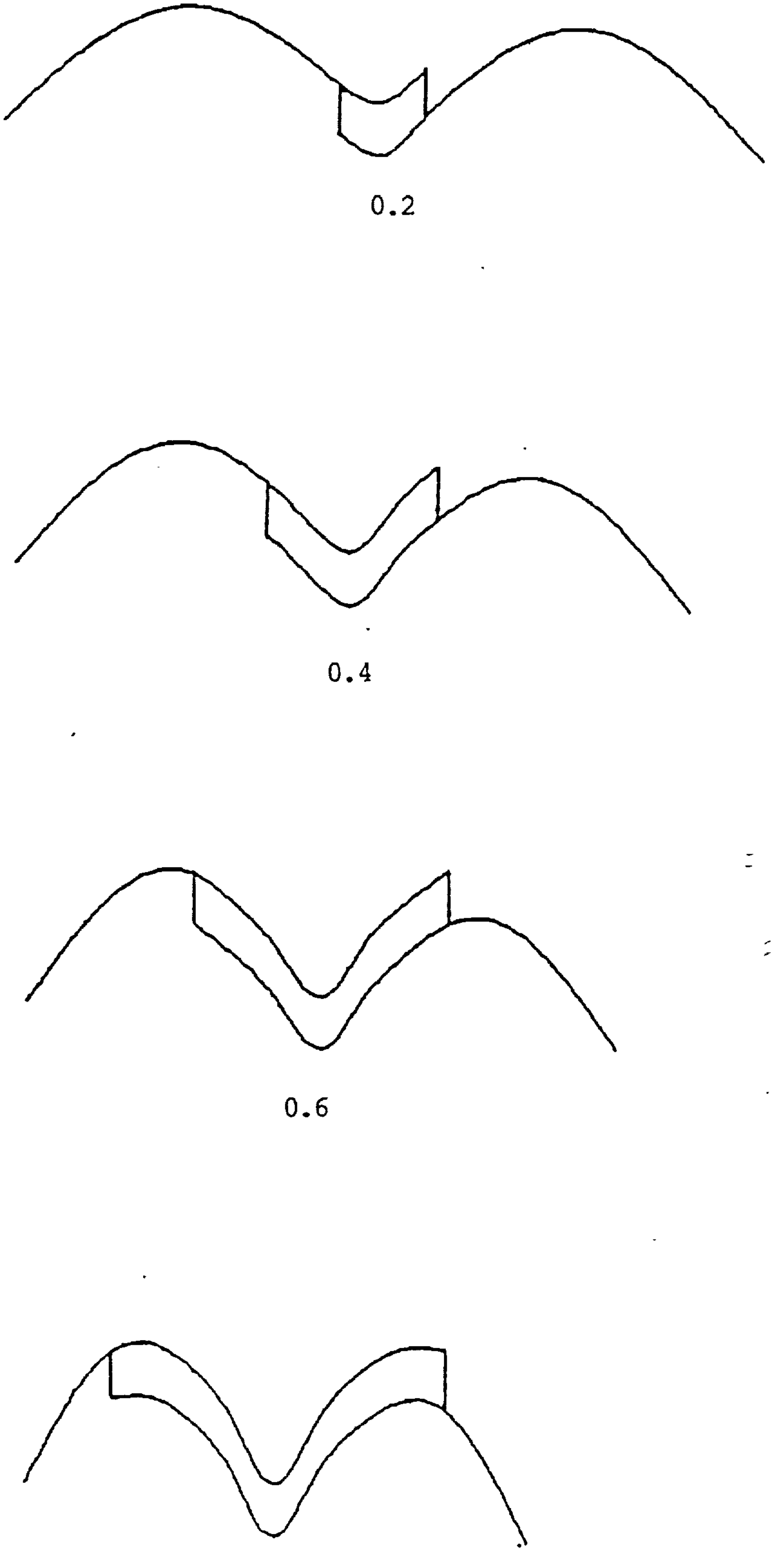

0.2

0.4

0.6

0.8

Figure 45. Theoretical Mode Shapes for Mode 2

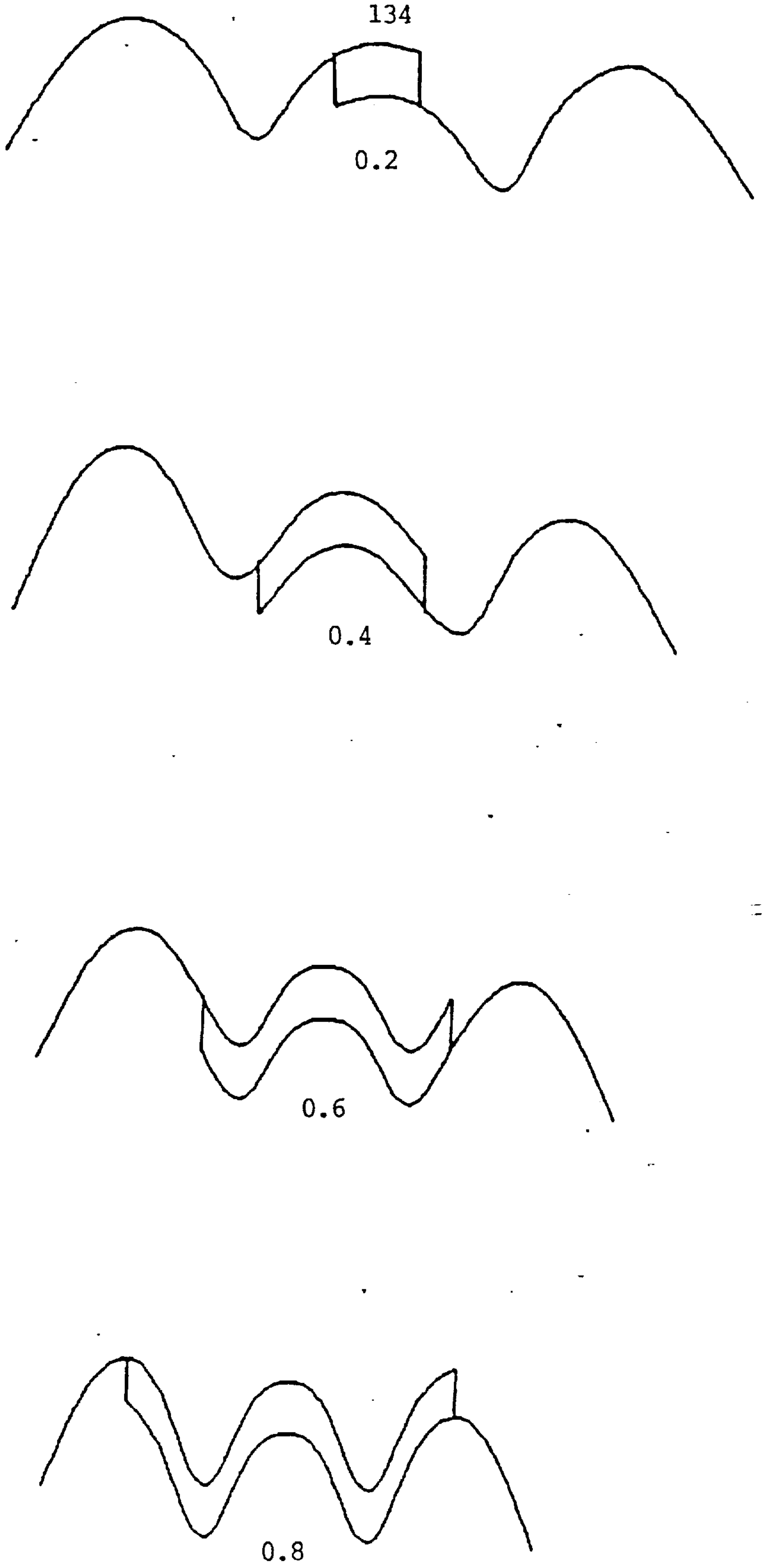

Figure 46. Theoretical Mode Shapes for Mode 3

Comparison with Experimental Results

Table 5 shows both theoretical and experimental results of two graphite epoxy lap joint systems with overlap ratios of 0.2 and 0.5. All of the theoretical results were generated by considering simply-supported boundary conditions at the ends.

Table 5

Comparison of Theoretical and Experimental Results of the Graphite Epoxy Lap Joint Systems

Overlap Ratio	Mode No.	Natural Frequency(Hz)			Damping Ratio(%)		
		Theory[1]	Expt.[1]	%Error	Theory[1]	Expt.[1]	Expt.[2]
0.2	1	195.9	207.0	5	0.53	1.51	0.20
	2	898.5	986.2	9	0.12	1.63	0.16
	3	1864.5	1984.0	6	0.05	2.29	0.10
0.4	1	263.5	270.6	3	0.13	0.68	0.43
	2	1148.4	1075.5	-6	0.15	1.43	0.12
	3	2492.7	2684.4	7	0.20	0.83	0.15

[1] Using Simply-Supported boundary conditions

[2] Using Free Free boundary conditions.

The specimens were prepared by bonding two similar graphite epoxy beams over the desired length of overlap using an epoxy adhesive. The epoxy resin was procured from CIBA-GEIGY Corporation. Much care was taken to obtain a good bond by properly curing the joint system in an oven. The dimensions of the unbonded beams were: length = 12.25 cm, width = 2.8 cm, and thickness = 0.25 cm. These dimensions and the material constants (Young's Modulus and Shear Modulus) were input to the computer program to predict the theoretical natural frequencies, modal damping ratios and mode shapes.

The supports to simulate simply-supported boundaries at the ends were specially fabricated in the form of two separate triangular blocks with a knife edge on each, to support the beam, one from the top, and the other from the bottom. The two blocks were then clamped to a rigid base. In order to evaluate the experimental simulation of these supports, a trial test was first conducted on an aluminum beam. Excellent agreement was obtained between the theoretical natural frequencies (computed using simply-supported boundary conditions) andmeasured values. In fact, the percentage difference between the two results never exceeded 2% for the first four modes. Having established the validity of the above text fixtures, experiments were later conducted on graphite epoxy lap-jointed beams. An impact hammer with an attached force transducer was used for exciting the specimen and the response was measured using a mini-accelerometer (Bruel & Kjaer 4375). The frequency response (ratio of acceleration to force signals) was immediately computed and recorded on an FFT analyzer

(Bruel & Kjaer 2032). The modal parameters were then computed using the Structural Measurement Systems (SMS) modal analysis software.

Referring to Table 5 it is seen that there is good agreement between the predicted values of natural frequencies and experimental data. The percentage difference between the two results is in the range of 3 to 9%. The measured damping ratio values in column 7 (Table 5) are larger than the predicted values. This is presumably due to additional damping contributions at the end supports in the experimental data. In order to substantiate this, damping measurements were made on the same samples without the end fixtures. Column 8 of Table 5 shows these results. In this case, testing was done by simply mounting the sample directly on a shaker using a thin layer of wax. The resonance frequencies in this case were, of course, somewhat different from those obtained previously using the simply-supported boundary conditions. It is interesting to notice, however, that the predicted damping values in column 6 and the measured data in column 8 are of the same order. Next, theoretical mode shape is compared with experimental mode shape in Figures 47 for mode 1. Note that no attempt has been made to normalize the different amplitudes in the theoretical and experimental results. There is excellent agreement between the two mode shapes for the first mode as seen in Figure 47. The small discrepancies in the two results can be attributed to several assumptions made in the theoretical analysis. The major assumption is the use of a constant value with frequency of vibration for the modulus of the beam material. Also, in the theoretical model it was assumed that the adhesive is flexible and that the damping is caused by both shering and transverse motions of the adhesive. In practice, however, it is very difficult to fabricate specimens to satisfy exactly the above requirements.

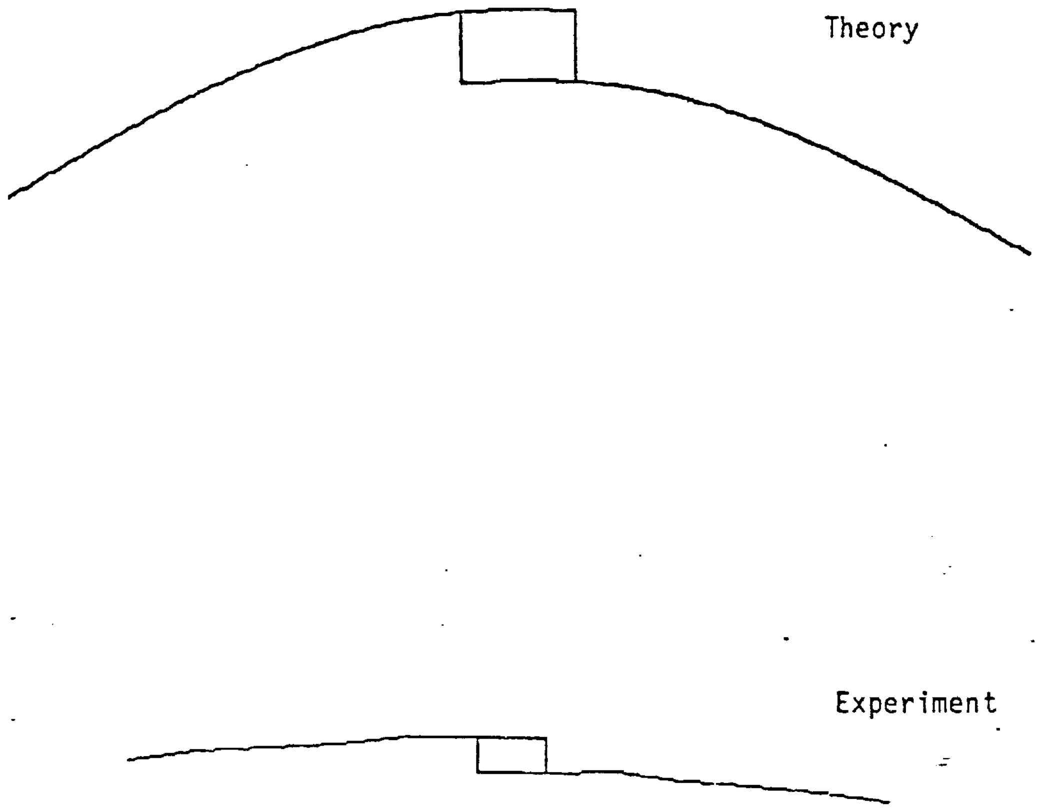

Figure 47. Comparison of Theoretical and Experimental Mode Shapes for Overlap Ratio = 0.2, Mode 1

Experimental Study of Damping of Bonded Double-Butt Joint Specimens

This section contains the results of experiments conducted on beam and jointed specimens in a vacuum chamber. Damping measurements were made on the following ten graphite epoxy samples which were procured from Sikorski Aircraft Company:

i) Five identical graphite epoxy beam specimens with a double-butt joint in the middle as shown in Figure 48 and ii) Five identical graphite epoxy beam specimens of dimensions as in 1 but with no joints.

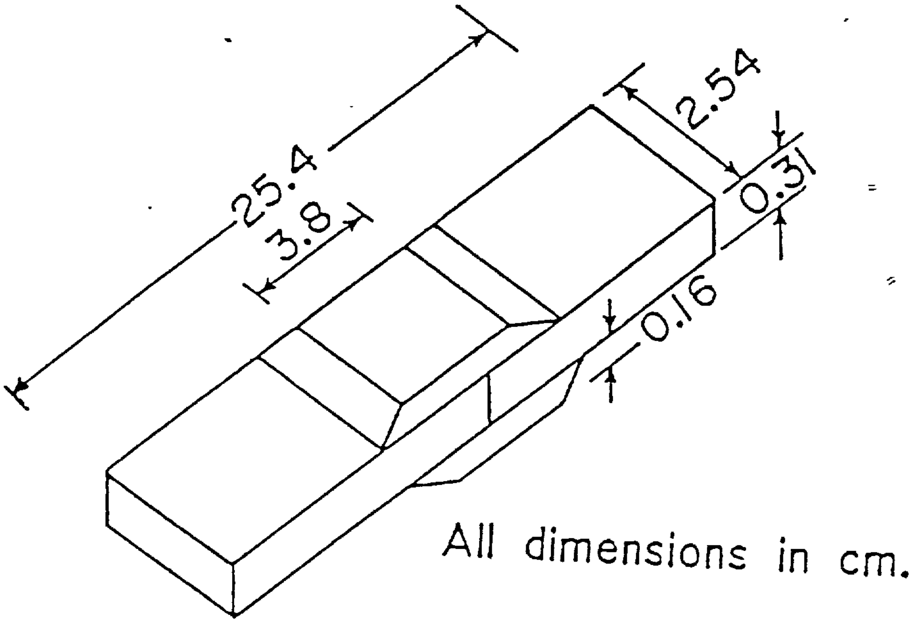

Figure 48. Double-Butt-Jointed Specimen

In each of the above experiments, the specimen was mounted at its center directly on the shaker using a thin layer of wax. This closely simulated free-free boundary conditions at the edges. Only odd numbered modes were excited, since the specimen was mounted at the center, which happens to be a node point for all even numbered modes for free-free boundary conditions. All the damping measurements were made using the usual improved half-power points method.

First, measurements were made on the double-butt-jointed (DBJ) specimens. In each case, the specimen with the shaker was kept inside the vacuum chamber and damping ratios and resonance frequencies were measured for the first and third mode of vibration, before the air was pumped out. Then the measurements were repeated in a vacuum when the pressure inside the chamber was about 0.1 mm of Hg. The test temperature remained ambient in both cases. Table 6 shows a summary of results for the five DBJ specimens tested under vacuum conditions. No significant change in the values of the damping ratio was noticed between the experiments conducted under normal atmospheric pressure and in a vacuum. This difference in the values of the damping ratio was in fact in the range of 0.01-0.02% during most of the trials.

From Table 6, it is seen that the average value for the damping ratio of the DBJ specimen for the first mode is 0.114% and that for the third mode is 0.155%. The small discrepancies in the values of the resonance frequencies in the five samples could be attributed to a) slight differences in their dimension and/or b) slight differences in the exact location of the excitation point during mounting.

The next set of experiments was conducted on the five beam specimens with no joints (having the same dimensions as the DBJ samples) under identical environmental conditions as maintained with the DBJ specimens. The results are tabulated in Table 7. Here, it is seen that the beam has an average value for the damping ratio of 0.107% for the first mode and 0.138% for the third mode.

By comparing the results of Table 6 and 7, it is seen that, although the damping ratio values for the jointed specimens appear somewhat higher than those of the beam specimens, this difference is very small. This observation is also true for the previous damping results of lap-jointed specimens with free-free boundary conditions.

Much care was exercised in maintaining identical environmental and other conditions in all of the above experiments. The damping measurements were made precisely by zooming in on each mode thus increasing the frequency resolution of the analyzer and minimizing the influence of external noise. Figure 49 is a plot of the frequency response data for a DBJ specimen for baseband excitation in the frequency range 0-1.6 kHz. The corresponding zoom frequency response plots for modes 1 and 3 are shown in Figures 50 and 51 respectively. Figures 52 through 54 show similar baseband and zoom frequency response plots for a beam sample.

Table 6

Experimental Results of Double-Butt-Jointed Specimens

Sample No.	Mode 1		Mode 3	
	f_n(Hz)	ζ_n(%)	f_n(Hz)	ζ_n(%)
1	258.2	0.11	1371.2	0.14
2	257.0	0.10	1375.9	0.13
3	260.0	0.13	1381.7	0.17
4	256.3	0.10	1368.5	0.17
5	261.3	0.12	1380.1	0.16
Average	258.6	0.11	1375.5	0.15

Table 7

Experimental Results of Beam Specimens with No Joints

Sample No.	Mode 1		Mode 3	
	f_n(Hz)	ζ_n(%)	f_n(Hz)	ζ_n(%)
1	341.1	0.11	1800.0	0.15
2	337.3	0.13	1782.2	0.15
3	340.5	0.11	1794.3	0.12
4	330.4	0.11	1749.2	0.12
5	334.5	0.10	1769.0	0.15
Average	336.8	0.11	1778.9	0.14

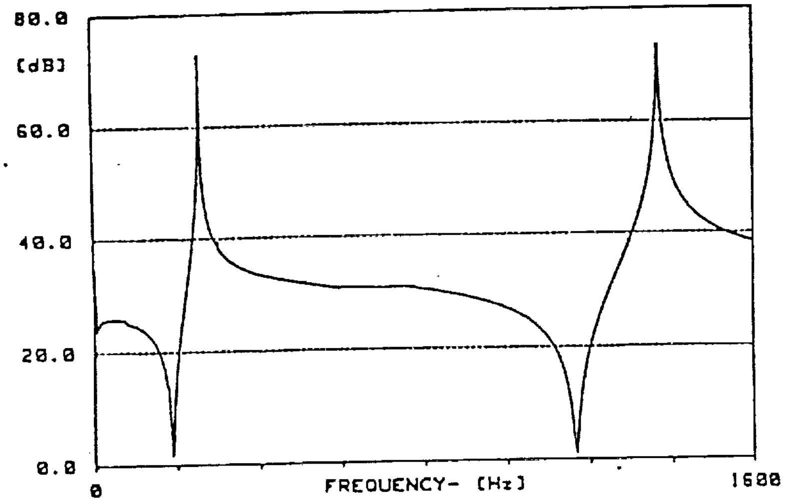

Figure 49. Frequency Response Plot of the Double-Butt-Jointed Specimen Using Baseband Analysis

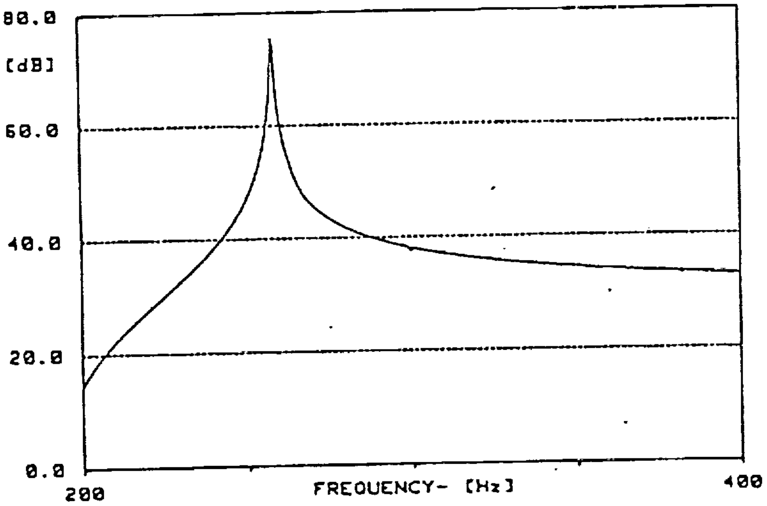

Figure 50. Frequency Response Plot of the Double-Butt-Jointed Specimen Using Zoom Analysis for Mode 1

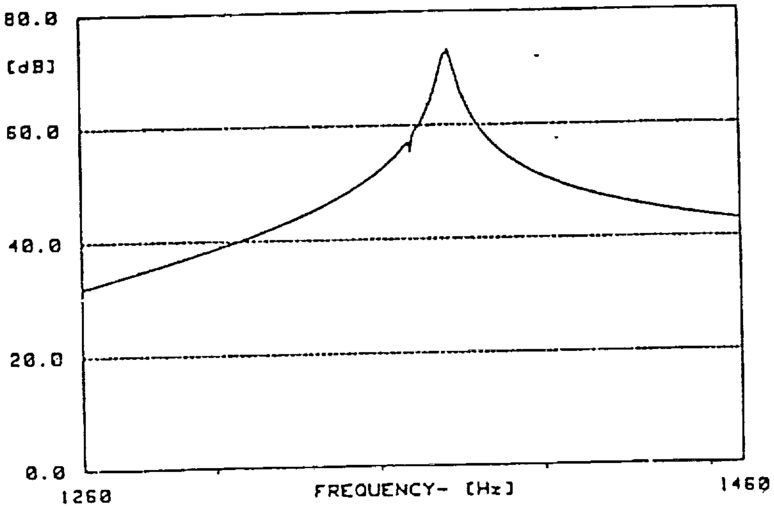

Figure 51. Frequency Response Plot of the Double-Butt-Jointed Specimen Using Zoom Analysis for Mode 3

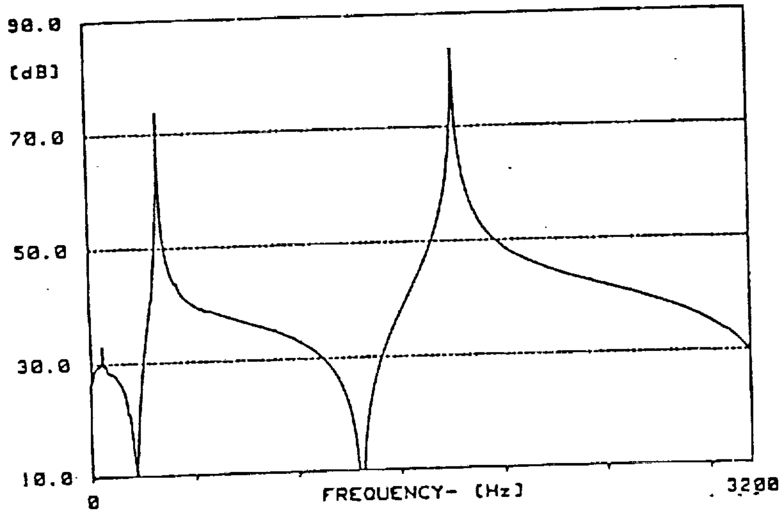

Figure 52. Frequency Response Plot of the Beam Specimen Using Baseband Analysis

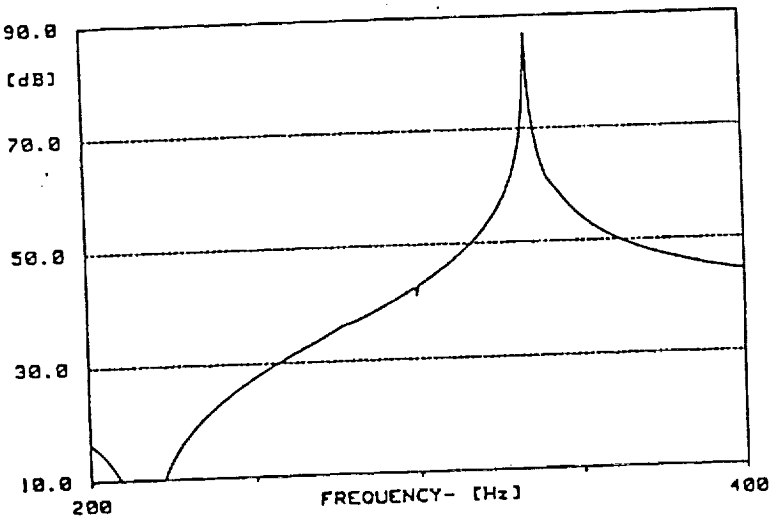

Figure 53. Frequency Response Plot of the Beam Specimen Using Zoom Analysis for Mode 1

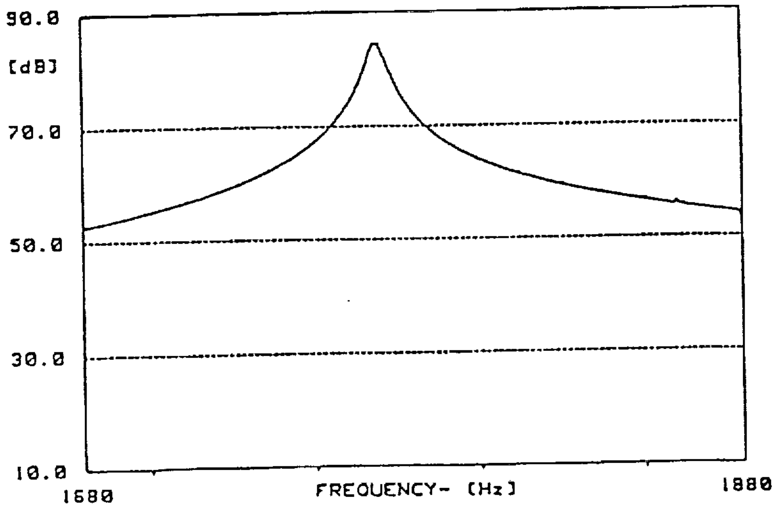

Figure 54. Frequency Response Plot of the Beam Specimen Using Zoom Analysis for Mode 3

ORIGINAL PAGE IS OF POOR QUALITY

VI. SUMMARY AND CONCLUSIONS

In this project an attempt has been made to evaluate the damping capacity of graphite epoxy materials and structural joints. The project ~~was sponsored~~ by the NASA George C. Marshall Space Flight Center, Huntsville, Alabama under contract No. NAS8-36146. The work involved a systematic investigation of the damping ratio of different composite specimens and bonded joints under normal atmospheric conditions and in a vacuum environment. Free and forced vibration test methods were employed for measuring the damping ratios. The effect of edge support conditions on the damping value of a composite tube specimen was studied by using a series of experiments performed on the specimen with different edge supports. It was finally found that simulating a free-free boundary conditions by having no constraints at the ends gives the lowest value of the material damping of the composite. The accuracy of the estimation of the damping ratio value was improved by using a curve-fitting technique on the response data obtained through measurement.

was evaluat

were

[illegible]

The effect of outgassing (moisture desorption) on the damping capacity was determined by measuring the damping ratio of the tube specimen in a vacuum environment before and after outgassing had occurred. The effects of high and low temperatures on the damping was also investigated by using a series of experiments on tube and beam specimens. Special experimental set-ups were developed to accomplish this objective. An analytical model to study the vibrations of a bonded lap joint system was formulated. Numerical results were generated for different overlap ratios of the system. These were compared with experimental results.

In order to determine the influence of bonded joints on the material damping capacity, experiments were conducted on bonded lap-jointed and double-butt-jointed specimens. These experimental results were compared with simple beam specimens with no joints.

The following conclusions may be drawn from the results of this investigation.

1) The damping ratio value is strongly dependent on the end support conditions used to support the specimens. It was observed that the end fixtures usually offer a large contribution to the damping capacity of the material.

2) The material damping ratio value of the composite tube is in the range of 0.1% - 0.15% for a frequency range of 500 Hz to 560 Hz under normal atmospheric conditions. The first bending mode of the specimen occurs in this frequency range. The damping ratio value seems to increase with higher modes and has a value of about 0.36% for a modal frequency of about 2840 Hz.

3) From the experiments conducted on the tube specimen in a vacuum, it may be concluded that the contribution of air damping to the material damping is between about 0.03% and 0.04%. The material damping ratio of the tube specimen in a vacuum is thus in the range of 0.06% and 0.11%. The effect of outgassing or moisture

desorption on the damping ratio value of the specimen is not very significant. The change in damping ratio value due to outgassing of the tube specimen for a period of about one month was observed to be 0.016%. The percentage change in the weight of the tube from its original weight was 0.9%. No significant change in the damping ratio with the vacuum pressure inside the chamber was observed.

4) It is observed that changes in temperature have a significant influence on the damping capacity of the composite material. From the experiments conducted on tube and beam specimens, it is observed that the damping of the material increases with temperatures above the atmospheric temperature and has a value of about 3% near the material glass transition temperature. There is, however, a small decreasing trend in the values of the damping with temperatures below the normal atmospheric temperature. This is in agreement with the data available in the literature on other types of composite materials.

5) The analytical model described in Chapter 4 can be used to predict the natural frequencies and the modes shapes of a bonded lap joint system for free vibration. The model can also be used to predict the system modal damping values by properly choosing the material damping values of the beam and the adhesive. Good agreement between numerical and experimental results for the modal frequencies and mode shapes was obtained. The percentage

differrence between the values of the theoretical and experimental natural frequencies is in the range of 3 to 9%.

6) From the numerical and experimental results obtained on lap-jointed beams, it is clear that the natural frequencies of the system increase with an increase in the length of overlap.

7) The increase in the value of the damping ratio due to the presence of bonded joints in the system does not appear to be very significant.

VII. RECOMMENDATIONS FOR FUTURE WORK

The material damping of the graphite epoxy specimens determined so far appears to be very low. This low value of damping may result in a significant truss system displacement amplitude of the telescope truss system, which, in turn may lead to a blurring of the optical system image. The total truss system damping, of course, will be be slightly higher because of the effect of the joints. But the precise effects of the bonded joints on the system damping is not known. Unbonded joints are known to provide significant contributions to the damping. More work is thus needed in this area to determine if the bonded joints can be relied on to increase the value of damping. This work should include both analytical and experimental work on other types of joints as encountered in space structures. Some of these joints are tubular joints, bolted joints etc. Typical configurations of tubular joints are shown in Figure 55.

Another area which needs attention is the dependence of damping with frequency. The material damping at very low frequencies must be determined since many large space structures are found to possess very low fundamental resonance frequencies which are generally less than about 10 Hz. The dependence of damping with displacement amplitude is also important when the system vibrates at such low frequencies.

The study on the effect of moisture content on the damping capacity of these materials is not complete in many aspects. The moisture absorption and desorption capacity of these materials is not well known. The percentage moisture content of the material with respect to time, and the exact glass transition temperature need to be determined. The moisture absorption capacity of these materials is expected to be different if the material is soaked in water or exposed to humid air. These two approaches are expected to produce entirely different results. It is thus important to examine both the approaches in the future to determine the exact influence of moisture absorption and desorption on the damping capacity of these materials.

Work is also needed in the prediction of damping of the graphite epoxy material. Some work has been done by other investigators in predicting the damping of laminated composite plates using a finite element approach. There is a considerable scope for research in this area.

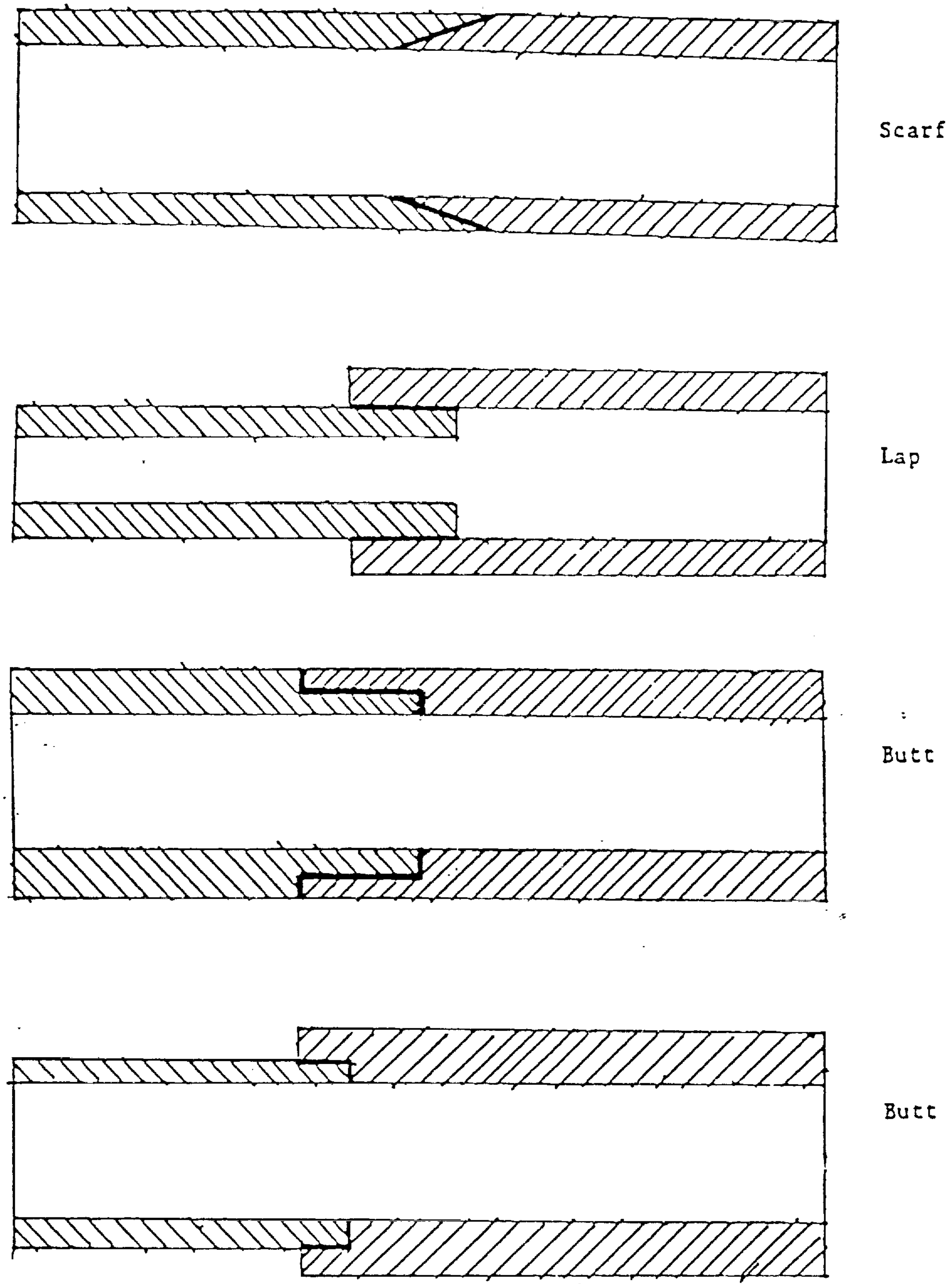

Figure 55. Different Types of Bonded Tube Joints

APPENDICES

APPENDIX A

ILLUSTRATION OF THE CURVE-FITTING TECHNIQUE

ILLUSTRATION OF THE CURVE-FITTING TECHNIQUE

The half-power points method of estimation of the damping ratio is not always accurate. It relies on how well one can read the frequency values for the half-power points from the frequency response data. It is seldom possible to estimate the half-power points without making any interpolation in the frequency values. The curve-fitting technique described in Chapter 2 can be used to overcome the above problem with the half-power points method. In the curve-fitting method, the entire data near a resonance are used for the estimation of the damping ratio, as opposed to three points in the half-power points method. Thus, a more accurate estimation of the damping ratio can be obtained. This method has been found to be especially well-suited and more accurate than the half-power points method for the case in which the frequency response curve is contaminated with noise.

In the present illustration, the damping ratio of the tube specimen was estimated by both the methods and the results are compared. In the curve-fitting technique, all three quantities, namely, the magnitude, the real part, and the imaginary part of the receptance function were utilized separately to estimate the damping ratio value. Figure 56 shows a comparison of the plots for the magnitude of the frequency response function obtained from both the measurement and the curve-fitting algorithm. Figures 57 and 58 show similar plots for the real part and the imaginary part of the frequency response function. All these data are for the tube specimen with a half ring as the connecting element. It may be recalled that the damping ratio value for the data using the half-power points method is 0.130% and the resonance frequency is 552.50 Hz. Now, using the curve-fitted response the damping ratio is estimated to be 0.128% and the resonance frequency to be 551.45 Hz. From the real part of the receptance curve using the curve-fitting method the damping ratio value is estimated to be 0.129& and the resonance frequency to be 551.36 Hz. From the imaginary part of the frequency response function and the curve-fitting method the damping ratio value is found to be 0.121% and the resonance frequency is 551.63Hz. All of the above results are summarized in Table 8. It is clear that there is excellent agreement in the results from the different approaches used.

In the present illustration the measured frequency response curve is close to an 'ideal' response plot of a single degree of freedom system. It shows a well-defined peak and the frequency range chosen is small. It was thus possible to easily locate the resonance frequencies and the half-power points. Hence, the damping ratio estimated from the half-power points agrees well with that of the curve-fitting method. But, in cases where the frequency response curve is not so 'ideal' as in the present case, it is always advantageous to estimate the damping ratio value using the curve-fitting method than the half-power points method.

Table 8

Comparison of Damping Data from Different Estimation Methods

	Curve-fitting data			Measured data
	From magnitude plot of receptance	From real part plot of receptance	From imaginary part plot of receptance	From half-power points method
Damping ratio	0.128%	0.129%	0.121%	0.130%
Resonance frequency (Hz)	551.45	551.36	551.63	551.50

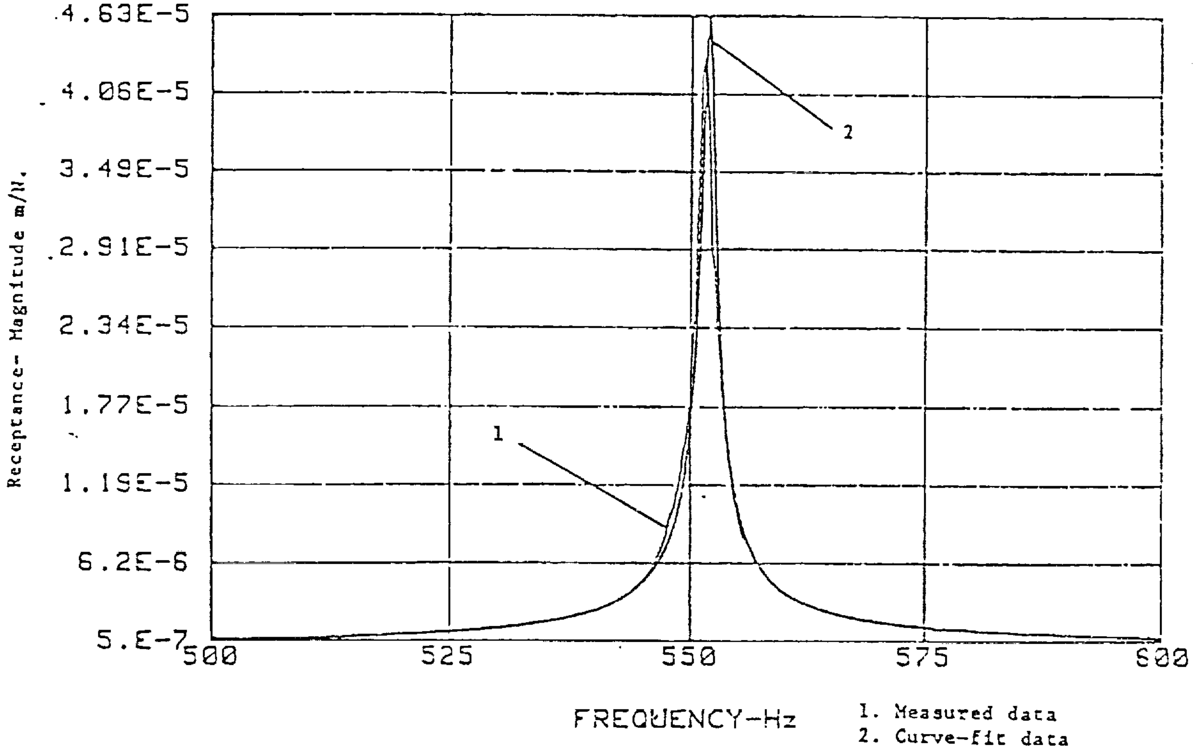

Figure 56. Comparison of the Curve-Fit and Experimental Data of the Magnitude of the Receptance

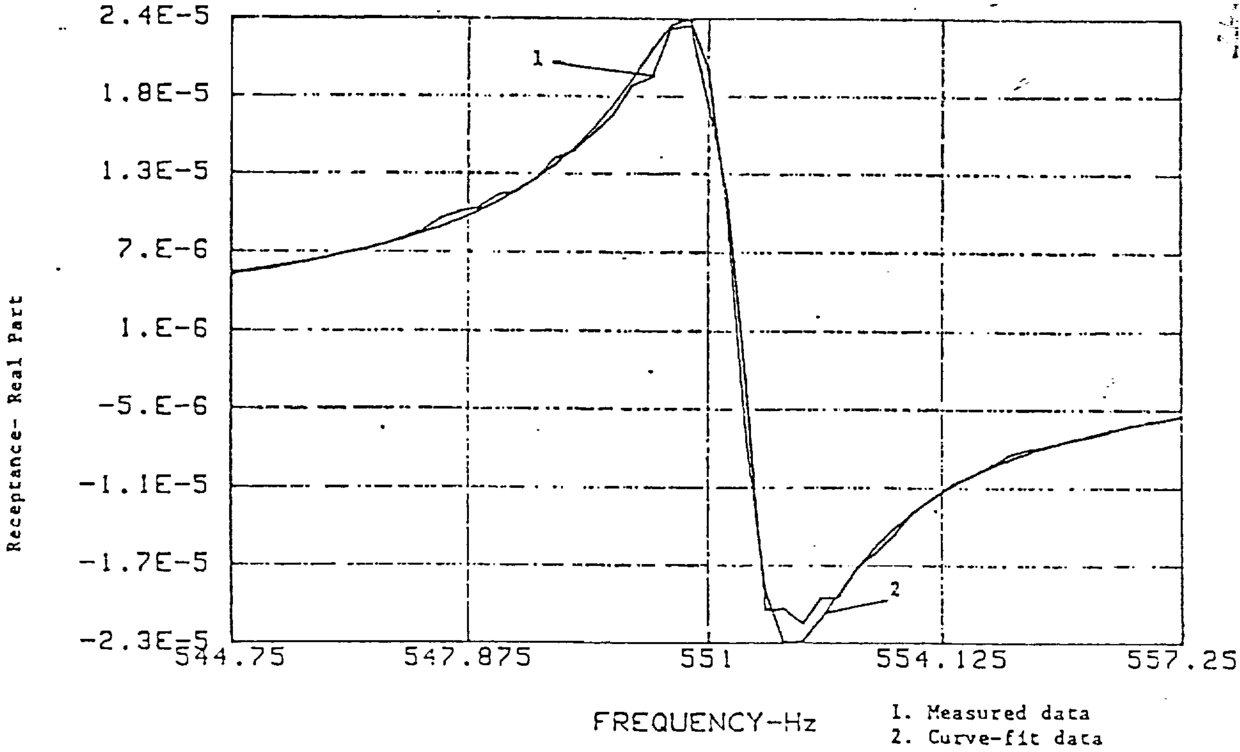

Figure 57. Comparison of the Curve-Fit and Experimental Data of the Real Part of the Receptance

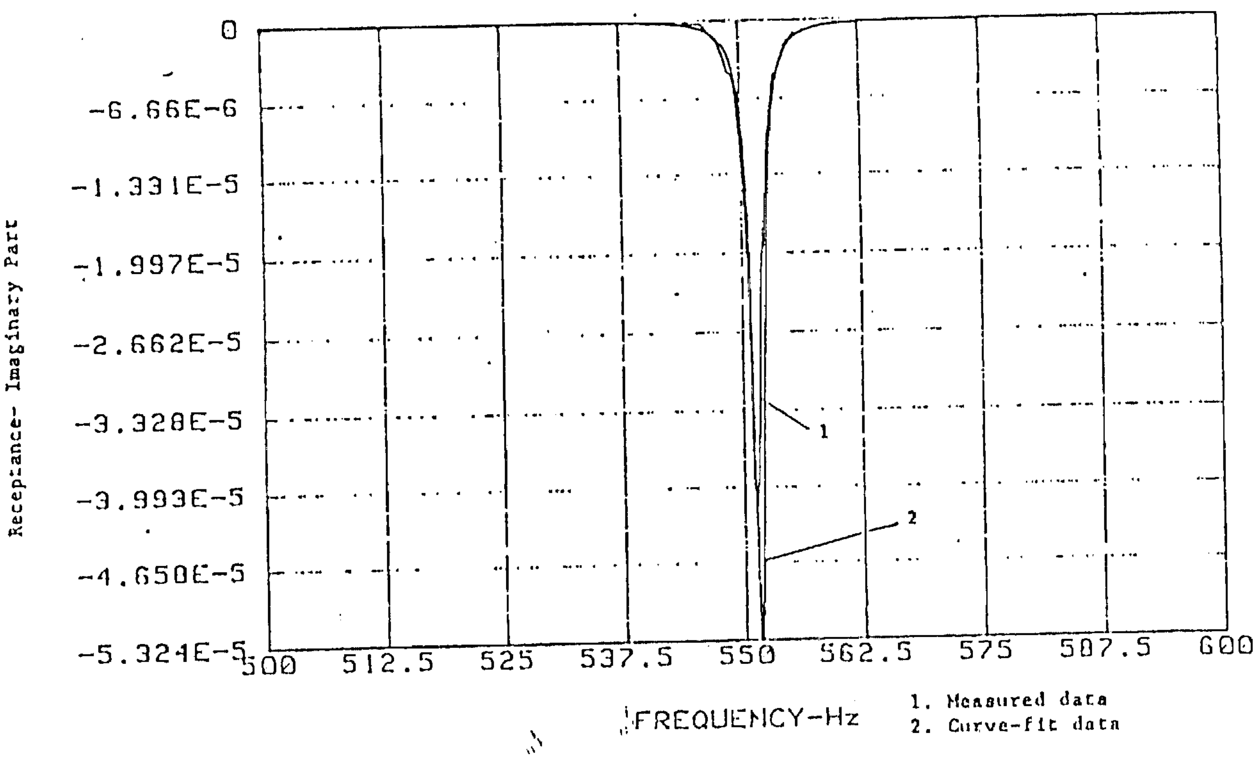

Figure 58. Comparison of the Curve-Fit and Experimental Data of the Imaginary Part of the Receptance

APPENDIX B

EQUATION OF MOTION OF STANDARD LINEAR SOLID MODEL

EQUATION OF MOTION OF STANDARD LINEAR SOLID MODEL

The standard linear solid model is shown in Figure 59 (a). It consists of a series combination of an elastic spring K_1, and viscous dashpot c, connected in parallel with another elastic spring K. When K_1 approaches infinity, the standard model reduces to the well-known Kelvin-Voight model as shown in Figure 59(b). In the other special case, when K is identically zero, the standard model reduces to the Maxwell model. The equation of motion for the standard linear model is developed as follows.

Let P_1 and P_2 be the forces in springs K_1 and K, such that

$$P = P_1 + P_2 \ . \tag{B1}$$

Referring to Figure 59(a), Let y_3 be the displacement of the node connecting K_1 and c. The forces P_1 and P_2 are given by

$$P_1 = K_1 \ (y_1 - y_3), \text{ and} \tag{B2}$$

$$P_2 = K \ (y_1 - y_2) \ . \tag{B3}$$

Differentiating Equation (B2) w.r.t. time t, we get,

$$\frac{\partial P_1}{\partial t} = K_1 \ \left(\frac{\partial y_1}{\partial t} - \frac{\partial y_3}{\partial t}\right) \ . \tag{B4}$$

The force in the dashpot is,

$$P_1 = c \ \left(\frac{\partial y_3}{\partial t} - \frac{\partial y_2}{\partial t}\right) \ . \tag{B5}$$

From Equations (B4) and (B5),

$$\frac{\partial y_1}{\partial t} = \frac{1}{K_1}\frac{\partial P_1}{\partial t} + \frac{P_1}{c} + \frac{\partial y_2}{\partial t} \quad , \tag{B6}$$

$$\text{i.e.,} \quad \frac{\partial y_1}{\partial t} - \frac{\partial y_2}{\partial t} = \frac{1}{K_1}\frac{\partial P_1}{\partial t} + \frac{P_1}{c} \quad . \tag{B7}$$

From Equation (B1) we have $P = P_1 + P_2$. therefore,

$$\frac{\partial P}{\partial t} = \frac{\partial P_1}{\partial t} + \frac{\partial P_2}{\partial t} \quad . \tag{B8}$$

Hence Equation (B7) becomes,

$$\frac{\partial y_1}{\partial t} - \frac{\partial y_2}{\partial t} = \frac{1}{K_1}[(\frac{\partial P}{\partial t} - \frac{\partial P_2}{\partial t}) + \frac{1}{c}(P-P_2)]. \tag{B9}$$

Substituting for P_2 and $\frac{\partial P_2}{\partial t}$ from Equation (B3), we obtain,

$$\frac{\partial y_1}{\partial t} - \frac{\partial y_2}{\partial t} = \frac{1}{K_1}[\frac{\partial P}{\partial t} - K(\frac{\partial y_1}{\partial t} - \frac{\partial y_2}{\partial t})] + \frac{1}{c}[P - K(y_1-y_2)]. \tag{B10}$$

Rearranging,

$$\frac{1}{K_1}\frac{\partial P}{\partial t} + \frac{P}{c} = (\frac{\partial y}{\partial t} - \frac{\partial y_2}{\partial t})[1 + \frac{K}{K_1}] + \frac{K}{c}(y_1 - y_2) \quad . \tag{B11}$$

This is the equation for the general linear solid model. In the limit when K_1 approaches infinity, the standard linear solid model becomes the Kelvin-Voight model as shown in Figure 59 (b). Taking the limit of Equation (B11) as K_1 approaches infinity, we get

$$P = c\,(\frac{\partial y}{\partial t} - \frac{\partial y}{\partial t}) + K\,(y_1-y_2). \tag{B12}$$

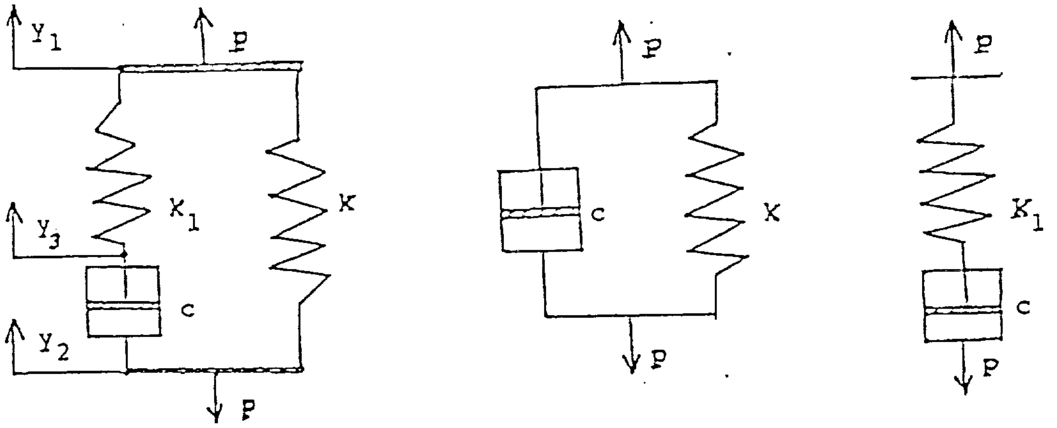

(a) Standard Linear Model

(b) Kelvin-Voight Model

(c) Maxwell Model

Figure 59. Viscoelastic Models

VIII. IMPROVEMENTS IN DAMPING MEASUREMENTS

In this chapter some improvements that have been considered in making accurate damping measurements are discussed. Since our main aim is to measure the damping of the graphite epoxy material, the damping from the supports of the specimen and other damping, such as that from the connecting cables and surrounding air are to be avoided. As discussed in the previous chapters, the best way to avoid damping from supports is to use a free-free support condition for the beam and excite it at its center through an impedance head mounted on a shaker. The input force signal to the beam and the output acceleration signal from it are fed through two charge amplifiers to the Dual Channel Signal Analyzer. Then the frequency response either inertance A/F, mobility V/F or receptance Y/F is obtained.

Preliminary Check of the Measured Results

The accuracy of the measured results may be evaluated from an observation of the frequency response curve and the measured resonance frequency by comparing them with the values obtained by theoretical analysis.

The Shape of Frequency Response Curve

A mathematical analysis is described herein which would help in predicting the frequency response curve for simple beams studied (the beams without joints).

For a simple beam with material and air damping as mentioned above, its displacement y can be obtained by superposition of displacements y_i corresponding to its infinite normal modes of vibration $X_i(x)$.

$$y(x,t) = \sum_{i=0}^{\infty} y_i = \sum_{i=0}^{\infty} \phi_i(t)\; X_i(x) \tag{8.1}$$

where normalized displacement function [121, 122]

$$X_o(x) = \frac{1}{\sqrt{l}} \text{ (rigid-body mode)} \tag{8.2}$$

and

$$X_i(x) = \frac{1}{\sqrt{l}} \left[\left(\cosh\frac{\lambda_i}{l}x + \cos\frac{\lambda_i}{l}x\right) - \sigma_i\left(\sinh\frac{\lambda_i}{l}x + \sin\frac{\lambda_i}{l}x\right)\right]$$

$$\left(i = 1,2,3 \ldots\infty \qquad \sigma_i = \frac{\cosh\lambda_i - \cos\lambda_i}{\sinh\lambda_i - \sin\lambda_i}\right) \tag{8.3}$$

are the solutions for the differential equation (8.4) with boundary conditions as given in Eq. (8.5).

$$EI\frac{\partial^4 y}{\partial x^4} + \rho A\frac{\partial^2 y}{\partial t^2} = 0 \tag{8.4}$$

$$\begin{aligned} \frac{\partial^2 y}{\partial x^2}\Big|_{x=0} &= \frac{\partial^2 y}{\partial x^2}\Big|_{x=l} = 0 \\ \frac{\partial^3 y}{\partial x^3}\Big|_{x=0} &= \frac{\partial^3 y}{\partial x^3}\Big|_{x=l} = 0 \end{aligned} \tag{8.5}$$

According to W.E. Baker et al [123], for a beam with material and air damping and with small amplitude vibration, its differential equation of motion for free vibration analysis is

$$EI\,\frac{\partial^4 y}{\partial x^4} + \beta EI\,\frac{\partial^5 y}{\partial x^4 \partial t} + \frac{C}{l}\,\frac{\partial y}{\partial t} + \rho A\frac{\partial^2 y}{\partial t^2} = 0 \tag{8.6}$$

Where the meaning of β can be found from Eq. (5.15) of this report. From Eqs. (8.1) and (8.3), $X_i(x)$ can be separated from Eq. (8.6) and the differential equation for the time function $\phi_i(t)$ $(i\neq 0)$ is obtained.

$$\ddot{\phi}_i + 2\alpha_i\,\dot{\phi}_i + \omega_i^2\,\phi_i = 0 \ (i\neq 0) \tag{8.7}$$

where

$$\omega_i^2 = \left(\frac{\lambda_i}{l}\right)^4 \frac{EI}{\rho A} \tag{8.8}$$

$$2\alpha_i = \omega_i^2 \beta E + \frac{C}{\rho A l} \tag{8.9}$$

By using the principle that the total virtual work should be zero, an equation similar to Eq. (8.7) can be written for a free-free beam with damping, supporting and exciting conditions as mentioned above.

$$\ddot{\phi}_i + 2\alpha_i\dot{\phi}_i + \omega_i^2\,\phi_i = \frac{F_o}{\rho A}\,X_i\left(\frac{l}{2}\right)\cos\omega t + g l X_i\left(\frac{l}{2}\right) \ (i\neq 0) \tag{8.10}$$

where $F_o\cos\omega t$ is the exciting force and g is the acceleration due to gravity.

However, for the rigid-body mode, the differential equation is

$$\rho A l\,\frac{\partial^2 y_o}{\partial t^2} = F_o\cos\omega t - C\,\frac{\partial y_o}{\partial t} \tag{8.11}$$

because there is no elastic force applied on the beam. From Eq. (8.11) the differential equation for ϕ_o is written as

$$\ddot{\phi}_o + a\dot{\phi} = \frac{F_o}{\rho A l X_o}\cos\omega t = \frac{F_o}{\rho A\sqrt{l}}\cos\omega t, \tag{8.12}$$

where

$$a = \frac{C}{\rho A l} \text{ .} \tag{8.13}$$

According to S. Timoshenko et al [122], the solution with the initial conditions

$$\begin{aligned} y|_{t=0} &= 0 \\ \frac{\partial y}{\partial t}\Big|_{t=0} &= 0 \end{aligned} \tag{8.14}$$

for Eqs. (8.12) and (8.10) are respectively as follows

$$\phi_\circ(t) = \frac{F_\circ}{\rho A \sqrt{l}} \left[- \frac{\cos(\omega t+\psi)}{\omega\sqrt{(\omega^2+a^2)}} + \frac{e^{-at}}{\omega^2+a^2}\right], \tag{8.15}$$

$$\phi_i(t) = \frac{g}{\omega_i^2} l X_i(\tfrac{l}{2})\left[1 - \frac{\omega_i}{\omega_d} e^{-\alpha_i t} \cos(\omega_d t-\gamma_i)\right] + \frac{F_\circ X_i(\frac{l}{2})\cos(\omega t-\theta_i)}{\rho A\sqrt{[(\omega_i^2-\omega^2)^2+(2\alpha_i\omega)^2]}}$$

$$- \frac{F_\circ X_i(\frac{l}{2}) e^{-\alpha_i t}}{\rho A\left[(\omega_i^2-\omega^2)^2+(2\alpha_i\omega)^2\right]} \left[(\omega_i^2-\omega^2)\cos w_d t + (\omega_i^2 \div \omega^2)\frac{\alpha_i}{\omega_d}\sin\omega_d t\right] \; (i\neq 0) \tag{8.16}$$

where

$$\psi=\tan^{-1}(\frac{a}{\omega}), \tag{8.17}$$

$$\gamma_i=\tan^{-1}(\frac{\alpha_i}{\omega_d}) \quad (i\neq 0), \tag{8.18}$$

$$\theta_i= \tan^{-1} (\frac{2\alpha_i\omega}{\omega_i^2-\omega^2}) \; (i\neq 0), \tag{8.19}$$

and

$$\omega_d = \sqrt{(\omega_i^2-\alpha_i^2)} \quad (i\neq 0). \tag{8.20}$$

Since $X_i(\frac{l}{2}) = 0$ $(i=2,4.6,\ldots\infty)$, for the center of the beam, the displacement and the steady-state displacement of the above beam are as follows

$$y(\tfrac{l}{2},t) = \phi_\circ(t)X_\circ(\tfrac{l}{2}) + \sum_{i=1,3,5}^{\infty} \phi_i(t)X_i(\tfrac{l}{2}) \qquad (8.21)$$

and

$$y(\tfrac{l}{2},t) = -\frac{F_\circ}{\rho Al}\frac{\cos(\omega t+\psi)}{\omega\sqrt{(\omega^2+a^2)}} + \sum_{i=1,3,5}^{\infty}\left\{\frac{g}{\omega_i^2} l X_i^2(\tfrac{l}{2}) + \frac{F_\circ X_i^2(\frac{l}{2})\cos(\omega t-\theta_i)}{\rho A\sqrt{[(\omega_i^2-\omega^2)^2+(2\alpha_i\omega)^2]}}\right\} \qquad (8.22)$$

Where the first term is the displacement for the rigid-body mode due to the exciting force, and after the summation sign the first term is the static displacement due to gravity and support, and the last term is the steady-state displacement due to the exciting force.

The corresponding velocity and acceleration at the center of the beam are written as

$$\frac{\partial}{\partial t} y(\tfrac{l}{2},t) = \frac{F_\circ}{\rho Al}\left\{\frac{\sin(\omega t+\psi)}{\sqrt{(\omega^2+a^2)}} - \sum_{i=1,3,5\ldots}^{\infty}\frac{l X_i^2(\frac{l}{2})\omega\sin(\omega t-\theta_i)}{\sqrt{\left[(\omega_i^2-\omega^2)^2+(2\alpha_i\omega)^2\right]}}\right\} \qquad (8.23)$$

$$\frac{\partial^2}{\partial y^2} y(\tfrac{l}{2},t) = \frac{F_\circ}{\rho Al}\left\{\frac{\omega}{\sqrt{(\omega^2+a^2)}}\cos(\omega t+\psi) - \sum_{i=1,3,5\ldots}^{\infty}\frac{l X_i^2(\frac{l}{2})\omega^2\cos(\omega t-\theta_i)}{\sqrt{\left[(\omega_i^2-\omega)^2+(2\alpha_i\omega)^2\right]}}\right\} \qquad (8.24)$$

By expressing Eqs. (8.23) and (8.24) in the complex form we have

$$\frac{\partial}{\partial t} y(\tfrac{l}{2},t) = \frac{F_\circ}{\rho Al}\left\{\frac{e^{j\psi}}{\sqrt{(\omega^2+a^2)}} - \sum_{i=1,3,5\ldots}^{\infty}\frac{l X_i^2(\frac{l}{2})\omega\; e^{-j\theta_i}}{\sqrt{\left[(\omega_i^2-\omega^2)^2+(2\alpha_i\omega)^2\right]}}\right\} e^{j(\omega t-\frac{\pi}{2})} \qquad (8.25)$$

$$\frac{\partial^2}{\partial y^2} y(\tfrac{l}{2},t) = \frac{F_\circ}{\rho Al}\left\{\frac{\omega e^{j\psi}}{\sqrt{(\omega^2+a^2)}} - \sum_{i=1,3,5\ldots}^{\infty}\frac{l X_i^2(\frac{l}{2})\omega^2\; e^{-j\theta_i}}{\sqrt{\left[(\omega_i^2-\omega^2)^2+(2\alpha_i\omega)^2\right]}}\right\} e^{j\omega t} \qquad (8.26)$$

or

$$\frac{\partial}{\partial t}\, y(\tfrac{l}{2},t) = \frac{F_\circ}{\rho A l}\sqrt{(A_\circ^2 + B_\circ^2)}\, e^{j(\omega t - \frac{\pi}{2} + \tan^{-1}\frac{A_\circ}{B_\circ})} \tag{8.27}$$

$$\frac{\partial^2}{\partial t^2}\, y(\tfrac{l}{2},t) = \frac{F_\circ \omega}{\rho A l}\sqrt{(A_\circ^2 + B_\circ^2)}\, e^{j(\omega t + \tan^{-1}\frac{A_\circ}{B_\circ})} \tag{8.28}$$

where

$$A_\circ = \frac{\cos\psi}{\sqrt{(\omega^2+a^2)}} - \sum_{i=1,3,5\ldots}^{\infty} \frac{lX_i^2(\frac{l}{2})\omega\cos\theta_i}{\sqrt{[(\omega_i^2-\omega^2)^2 + (2\alpha_i\omega)^2]}} \tag{8.29}$$

$$B_\circ = \frac{\sin\psi}{\sqrt{(\omega^2+a^2)}} + \sum_{i=1,3,5\ldots}^{\infty} \frac{lX_i^2(\frac{l}{2})\omega\sin\theta_i}{\sqrt{[(\omega_i^2-\omega^2)^2 + (2\alpha_i\omega)^2]}} \tag{8.30}$$

or

$$A_\circ = \frac{\omega}{\omega^2+a^2} - \sum_{i=1,3,5\ldots}^{\infty} \frac{lX_i^2(\frac{l}{2})\omega\,(\omega_i^2-\omega^2)}{(\omega_i^2-\omega^2)^2 + (2\alpha_i\omega)^2} \tag{8.31}$$

$$B_\circ = \frac{a}{\omega^2+a^2} + \sum_{i=1,3,5\ldots}^{\infty} \frac{lX_i^2(\frac{l}{2})\omega(2\alpha_i\omega)}{(\omega_i^2-\omega^2)^2 + (2\alpha_i\omega)^2} \tag{8.32}$$

Then the magnitude of the frequency response, the mobility and inertance are respectively as follows:

$$\left|\frac{V}{F_\circ}\right| = \left|\frac{1}{F_\circ}\frac{\partial}{\partial t}\, y(\tfrac{l}{2},t)\right| = \frac{1}{M}\sqrt{(A_\circ^2 + B_\circ^2)} \tag{8.33}$$

and

$$\left|\frac{A}{F_\circ}\right| = \left|\frac{1}{F_\circ}\frac{\partial^2}{\partial t^2}\, y(\tfrac{l}{2},t)\right| = \frac{\omega}{M}\sqrt{(A_\circ^2 + B_\circ^2)} \tag{8.34}$$

where

$$M=\rho A l \tag{8.35}$$

Figs. 60 and 61 respectively show the theoretical frequency response (mobility and inertance) of a graphite epoxy beam with the following parameters.

$l = 2.54\text{x}10^{-1}\text{m}$ (length of beam)

$b = 2.84\text{x}10^{-2}\text{m}$ (width of beam)

$h = 2.65\text{x}10^{-3}\text{m}$ (thickness of beam)

$E = 1.2\text{x}10^{11}$ Pa (storage modulus of elasticity for graphite epoxy)

$\rho = 1.6\text{x}10^{3}\ \text{kg/m}^{3}$ (density of graphite epoxy)

$\varsigma = 0.001$ (damping ratio of beam)

$a = \omega_1 \varsigma$

$\alpha_i = \omega_i \varsigma$ $(i \neq 0)$

When plotting these frequency response curves from Eqs. (8.33) and (8.34), only four leading odd modes of vibration were used in Eqs. (8.31) and (8.32).

By comparing the experimental frequency response of the mobility and inertance shown in Figs. 62 and 63 with the theoretical ones shown in Figs. 60 and 61 respectively, it is possible to estimate the accuracy of the measured results. Otherwise, if there are significant variations between the two curves, it is better to check the problem before the next measurements are made.

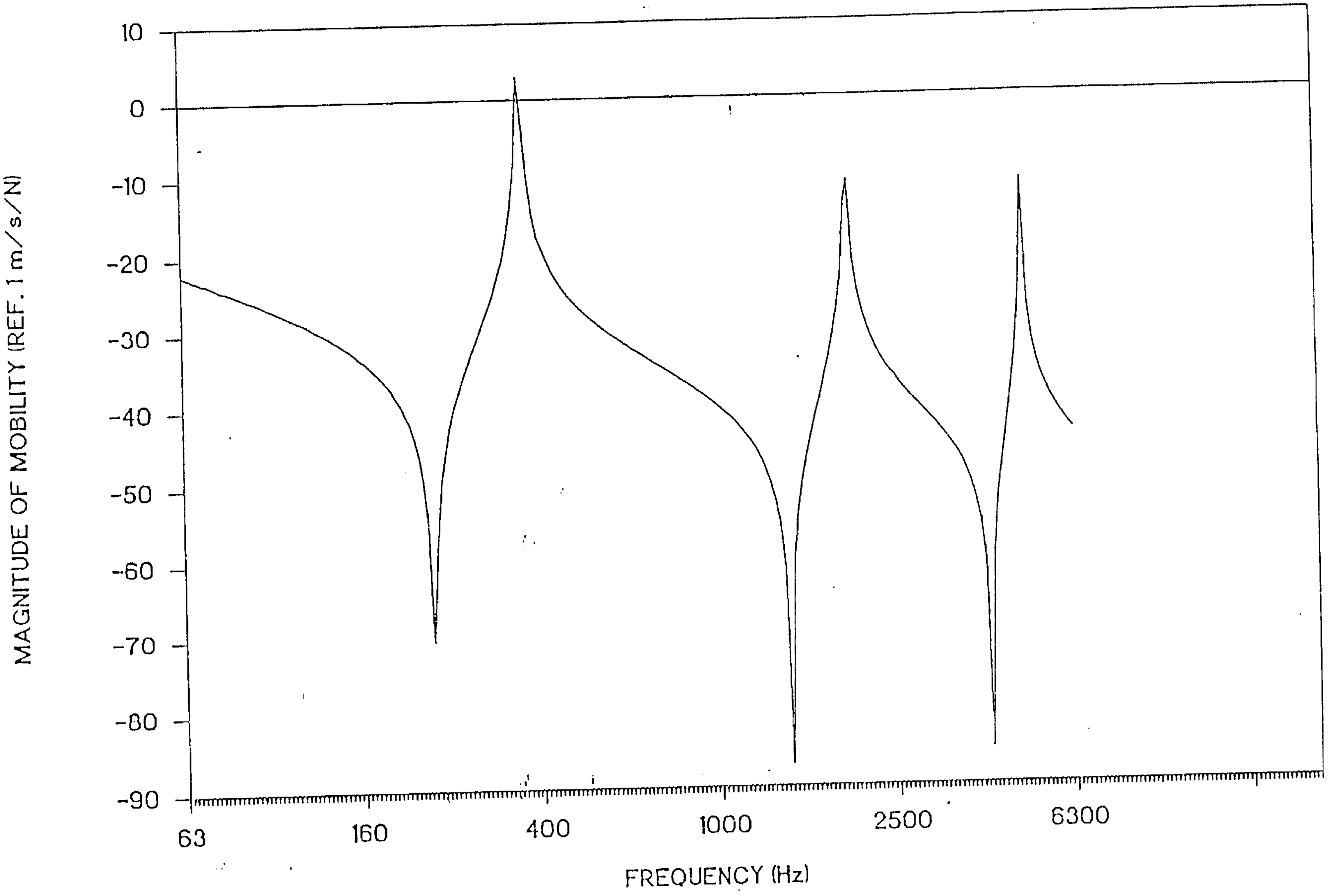

Figure 60. Theoretical Frequency Response of Mobility of the Beam

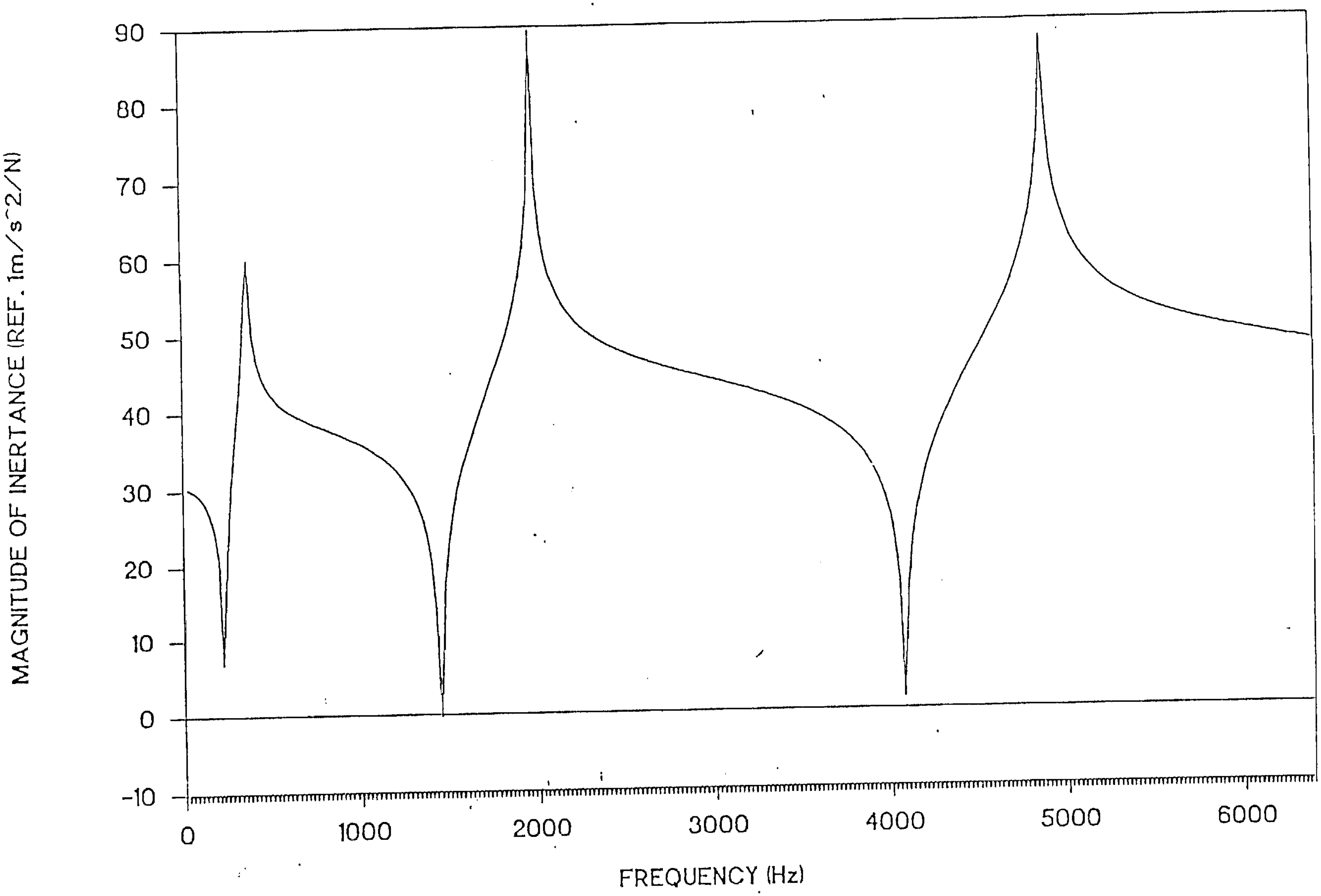

Figure 61. Theoretical Frequency Response of Inertance of the Beam

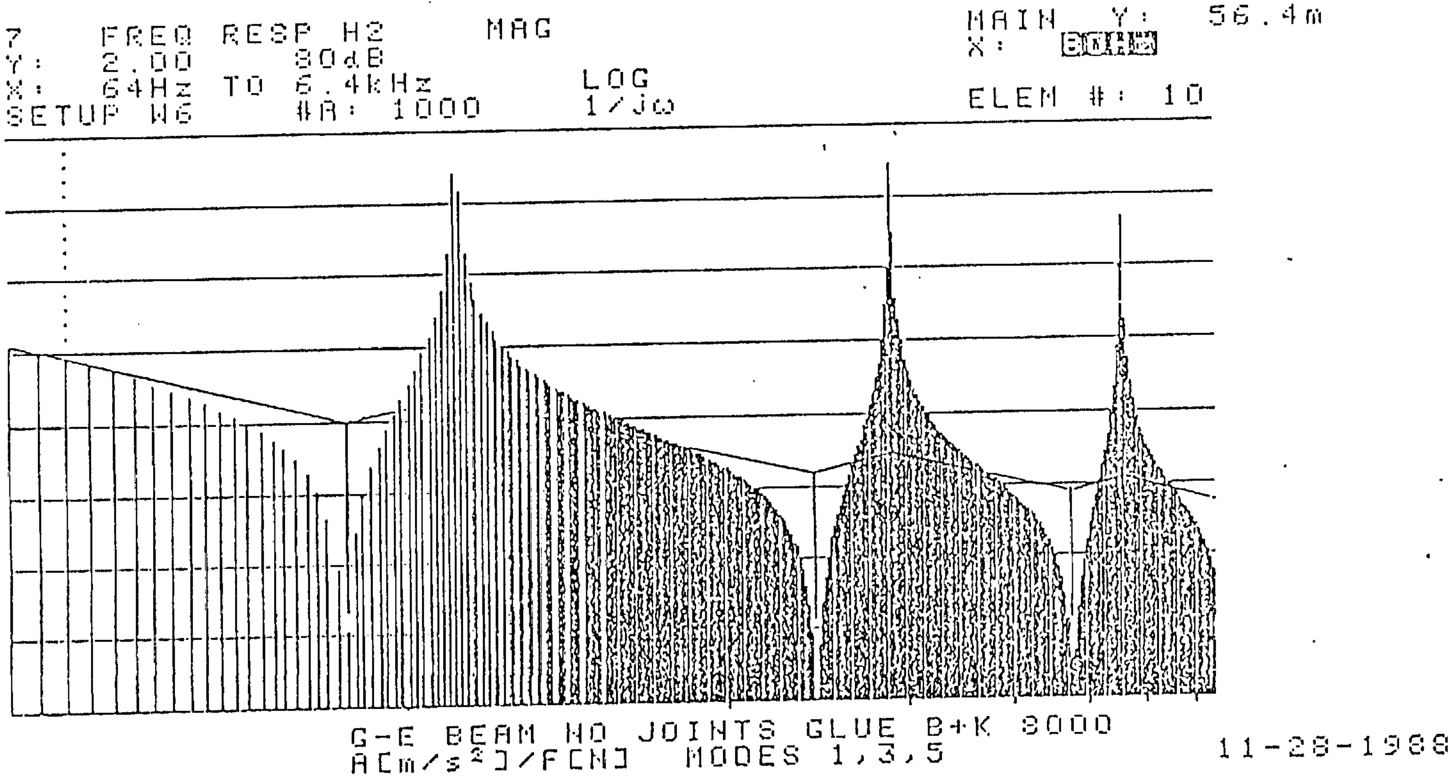

Figure 62. Experimental Frequency Response of Mobility of the Beam and Skeleton Check

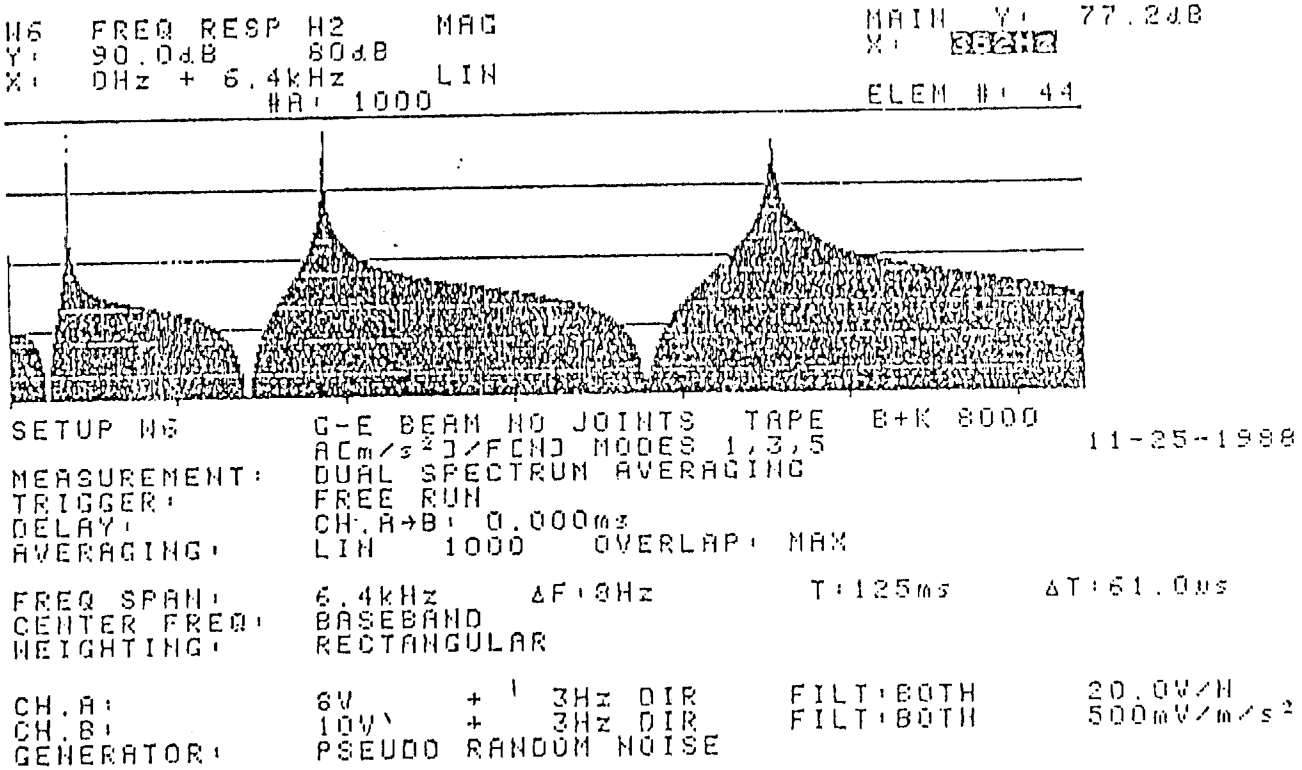

```
H6   FREQ RESP H2      MAG                         MAIN   Y:  77.2dB
Y:   90.0dB     80dB                               X:  [illegible]
X:   0Hz + 6.4kHz      LIN
             #A: 1000                              ELEM #: 44

SETUP H6          G-E BEAM NO JOINTS  TAPE  B+K 8000
                  A[m/s²]/F[N] MODES 1,3,5                  11-25-1988
MEASUREMENT:      DUAL SPECTRUM AVERAGING
TRIGGER:          FREE RUN
DELAY:            CH.A→B: 0.000ms
AVERAGING:        LIN   1000   OVERLAP: MAX

FREQ SPAN:        6.4kHz    ΔF:8Hz        T:125ms     ΔT:61.0us
CENTER FREQ:      BASEBAND
WEIGHTING:        RECTANGULAR

CH.A:             6V     +   3Hz DIR    FILT:BOTH      20.0V/N
CH.B:             10V    +   3Hz DIR    FILT:BOTH      500mV/m/s²
GENERATOR:        PSEUDO RANDOM NOISE
```

Figure 63. Experimental Frequency Response of Inertance of the Beam

The Skeleton of Mobility Plot [25]

For a structure more complicated than a simple beam, it is difficult to predict its frequency response. Therefore, the utility of observing the shape of the frequency response curve is limited. Another technique used for checking the measured results is called skeleton check and is shown in Fig. 62. It is suitable for any structure with free-free support condition, and it should be used for the frequency response curves which are plotted in logarithmic scales. If there is a tendency that the ±6dB/Oct straight lines go down with an increase in frequency, the measured results may be all right. We can find our results to agree very well with this method of checking.

The Accuracy of the Resonance Frequency

For a lightly damped simple beam it is easy to predict its natural frequency. Hence, a good agreement of the measured resonance frequencies with the predicted natural frequencies also indicates a good measurement. Obviously if the measured resonance frequencies are found to be lower than the calculated ones there must be a load effecting the beam vibration.

Improving the Mounting of Beams

It is found that the mounting of the beam specimens under test play an important role in damping measurements. Hence time and effort has been spent for selecting the best mounting method. The advantage of supporting the beam at its center is that it prevents excessive damping from the supports as in the case of a cantilevered or a simply supported beam. Unfortunately, the disadvantage for a center supported beam is that the center point is the antinode of the odd mode vibration of the beam, and that a load at the antinode will produce a notable impact. If the load is a mass, it will only lower the resonance frequencies; if it is a resistance, it will not only lower the resonance frequencies but also increase the damping [124].

After extensive trials with wax, stud, glue and tape, the double sided adhesive thin tape has been chosen for mounting the specimens. Wax is not ideal, because a mounting with less wax tends to be too loose while the specimen is vibrating, and if too much wax is used, the measured damping ratio will be very high. Although the stud mounting is stable enough, it tends to decrease the resonance frequencies and increase the damping ratio value significantly. Glue mounting is also stable, but the surface area of contact between the beam and the impedance head is often too large, hence the measured damping ratio value will tend to be higher than that of the specimen under test.

In order to get a rather stable and minimally damped support for making damping measurements, a narrow piece of carpet tape about 1 mm in width was stuck at the center of the beam perpendicular to the length of the beam. Since the tape is very thin, it was necessary to keep the beam balanced. This was done by ensuring that the gap between the beam and the impedance head on either side of the tape mounting is the same.

Selection of Excitation

There are several kinds of signals generated by the B&K Dual Channel Signal Analyzer Type 2032. Pseudo-random noise is a self-windowing function, and it is often used as the excitation in measuring the frequency response of fairly linear systems, particularly for lightly damped resonances, because the self-windowing functions generate no leakage while obtaining the Fast Fourier Transform. Without a self-windowing excitation, even with a Hanning Window, energy could leak from a lightly damped resonance into adjacent spectrum lines. The resulting spectrum would show greater damping than it actually exists. Furthermore, pseudo-random noise gives the frequency response much faster when compared to the random noise excitation. Because the latter is a true noise, it must be averaged for several time records before an accurate frequency response can be determined [125].

Another aspect of the excitation is its amplitude. The rule of thumb for selecting a suitable amplitude is that the excitation must be strong enough to get the needed signal to noise ratio, and must not be so strong as to damage the stability of mounting and linearity of the system.

Elimination of Noise in Measurements

Electrical Noise

Electrical noise may be eliminated by properly grounding the measuring instruments according to their specifications. It is necessary to point out that the housing of the impedance head should be isolated from the grounded shaker with a specially made electrically isolated stud and a mica washer.

There is often an electrical noise at the center frequency of the frequency span in the frequency response measurements made by B & K 2032 Analyzer. In order to avoid this type of noise, it is suggested that the resonance frequency of the specimen be not selected as the center frequency of zoom measurements.

Mechanical Noise

Sometimes vibration coming from the foundation of the shaker very much effects the measurements. A piece of soft foam may be inserted beneath the shaker. This acts as a cushion and was found to be quite helpful in preventing such disturbance. But in the case of measurements taken inside a vacuum chamber, since the foam is often full of dust which is harmful for the vacuum pump, a vibration isolater with very low resonance frequency (just a few Hertz) was used in place of soft foam.

Another problem is the force or vibration coming from the cables connected to the impedance head. Compared with the weight of the specimen, the disturbance of the cables is rather heavy, although the cables are soft and light. Keeping the cables as straight as possible to prevent them from bending and putting the cables on a cushion to damp out their vibration may solve this problem. But when working inside the vacuum chamber, it was found difficult to do so, because the space in the bell jar was very restricted. Therefore, it is suggested that softer and lighter cables be used while making measurements in a vacuum chamber.

Further Check of the Measured Results

After the above problems having been considered, the accuracy of the measured results improved to a great extent. In order to make sure that the experimental results were reliable, further check was always conducted during the measurement procedure. The signal to noise ratio and coherence between the two channels were observed for each measurement. The optimum requirements were found to be a signal to noise ratio of over 20dB, a coherence of over

0.91, and a very small difference between the frequency responses H2 and H1 measured by the B&K Analyzer. At the same time, the repeatability of several successive results was also observed. It was found that as the signal to noise ratio, coherence and the value of the damping ratio decreased, the difference between H2 and H1 and the resonance frequency increased quickly. The reason was most often found to be related to the mounting of the beam which probably got slack.

Experimental Study of Damping of Jointed Specimens

This section contains the results of experiments conducted on beam type specimens with and without joints. The joints studied herein were made from pieces of graphite epoxy beam type specimens. Damping measurements were made on the following type of jointed specimens. 1. Bolted Single Lap Joint (Fig. 64), 2. Bonded Double Lap Joint (Fig. 65), 3. Bolted Double Lap Joint (Fig. 66), 4. Bonded-Bolted Double Lap Joint (Fig. 66), 5. Bonded Scarf Joint (Fig. 67), and 6. Bolted Butt Joint (Fig. 68). The measured damping ratios for these jointed specimens are shown in Table 9. The damping ratio value of specimens without joints was also measured under identical conditions when measurements were made on each of the jointed specimens. All the values of damping ratio reported in Table 9 were obtained after conducting about ten trial runs on each specimen. This was done to ensure repeatability of the results. Also each time a measurement was made it was checked for accuracy using the methods described earlier.

The following conclusions may be drawn from the summary of results presented in Table 9.

The damping ratio of a graphite epoxy beam without joints is of the order of 0.05% to 0.06%. Compared to the earlier results listed in Tables 3,4 and 7, the latest data are about one half of the previous ones. According to Plunkett [128], if measurements are taken on similar specimens, at the same stress level and by comparable methods, usually the lowest reported value of damping is most likely to be closer to the correct value. The actual material damping will probably be lower than any of the values that are measured. Also, there might have been some little differences in the material used for making the specimens whose damping values are reported in Tables 3,4 and 7 and those values reported in Table 9.

The damping ratio value of jointed beams is found to be higher than that of the specimens without joints. This conclusion also differs from the earlier one described in pages 142 and 149.

It appears that the damping ratio values tend to increase when the beams are bolted together than when they are just bonded together. The damping ratio value for a double lap joint is higher than that of a single lap joint.

Lastly the difference in the damping ratio values measured under atmospheric conditions and in a vacuum (0.1mm Hg) seems to be not very significant. The possible reason is that the damping measurements might have been affected by the connecting cables used for the impedance head.

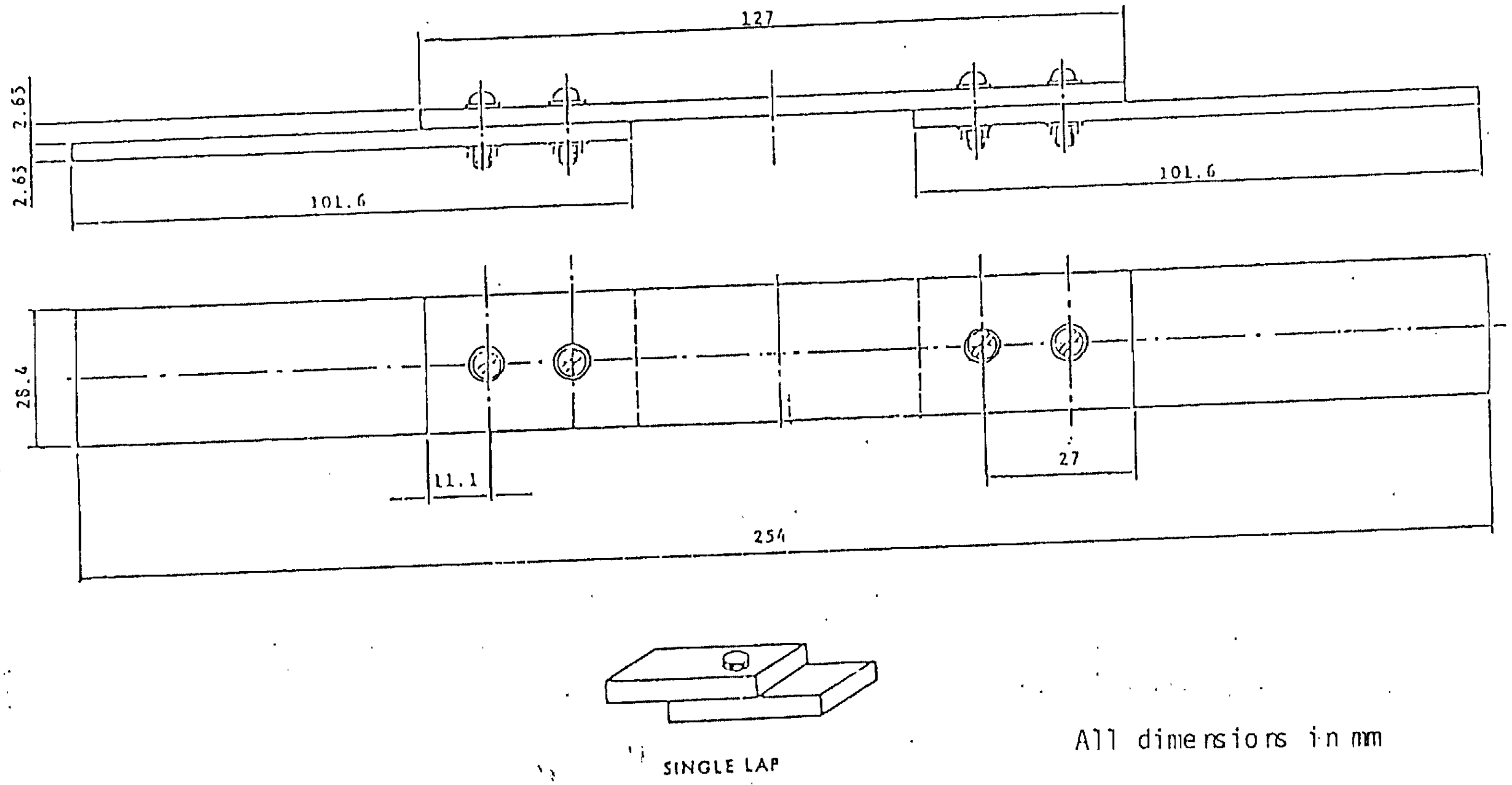

All dimensions in mm

Figure 64. Graphite Epoxy Beam with Bolted Single Lap Joints

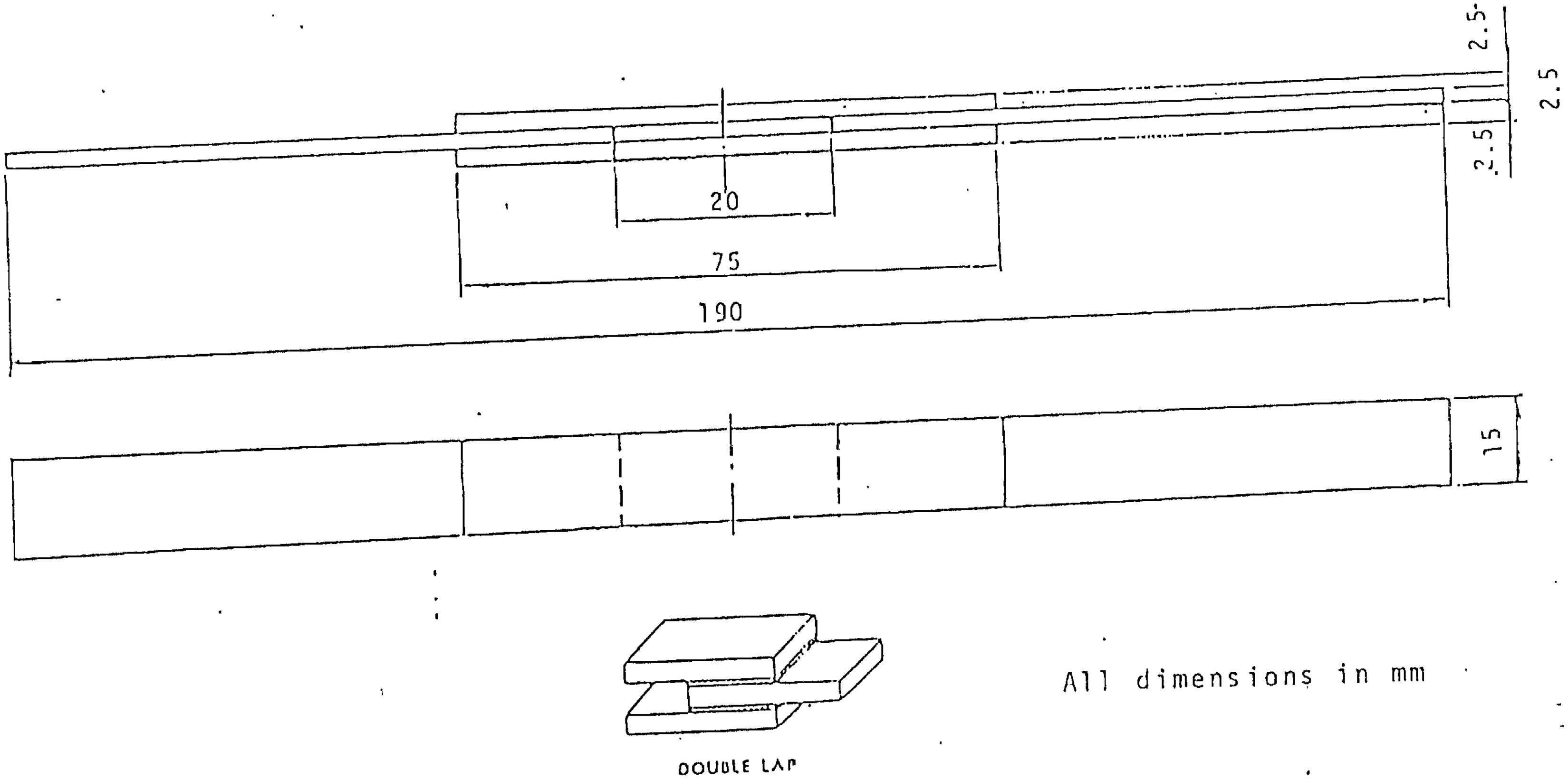

All dimensions in mm

Figure 65. Graphite Epoxy Beam with Bonded Double Lap Joints

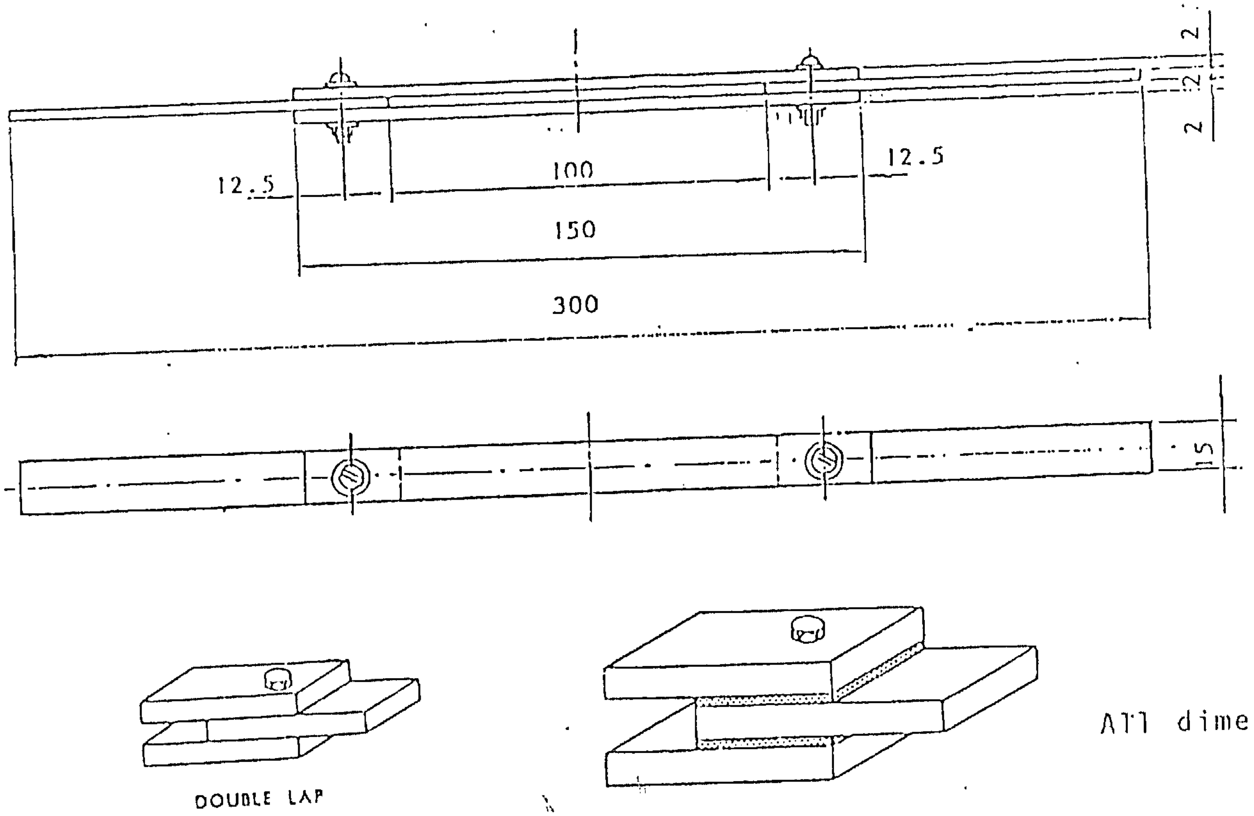

All dimensions in mm

Figure 66. Graphite Epoxy Beam with Bolted Double Lap Joints (left) and Graphite Epoxy Beam with Bonded-Bolted Double Lap Joints (right)

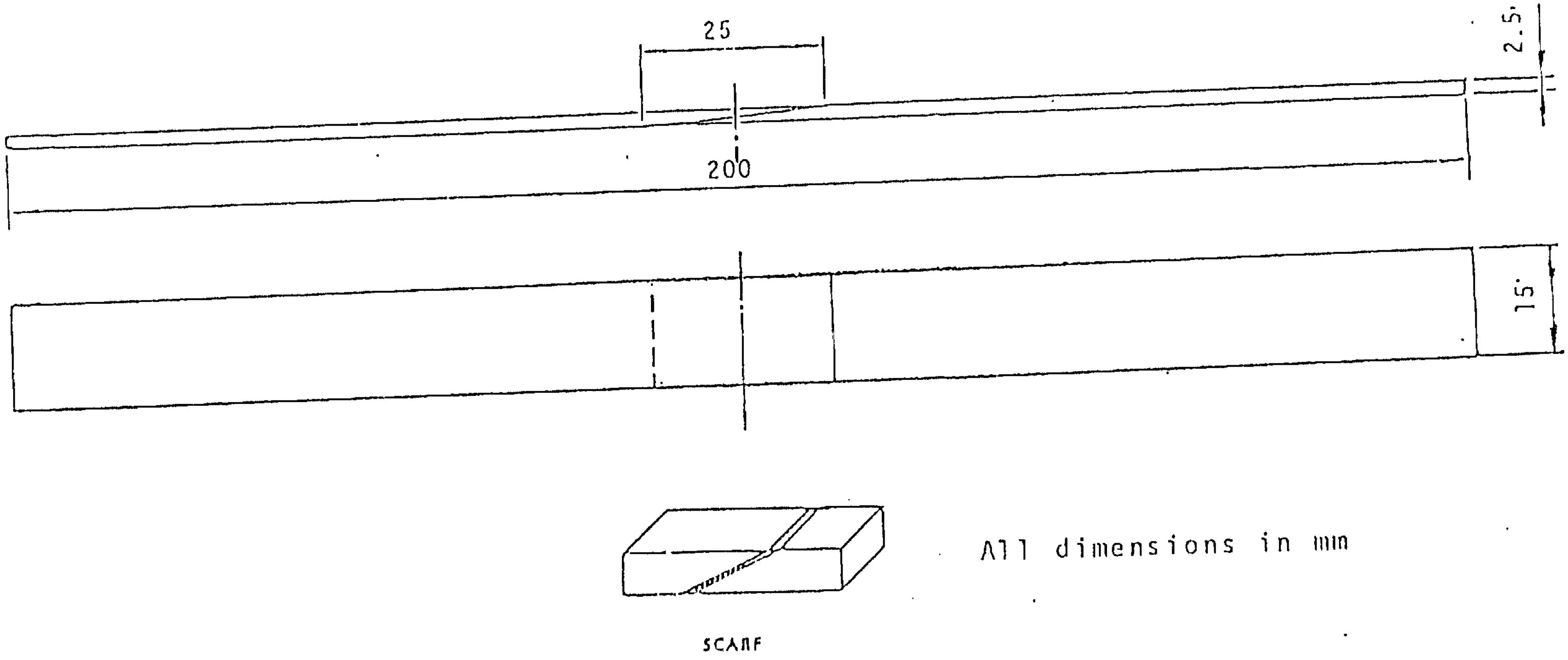

All dimensions in mm

Figure 67. Graphite Epoxy Beam with Bonded Scarf Joint

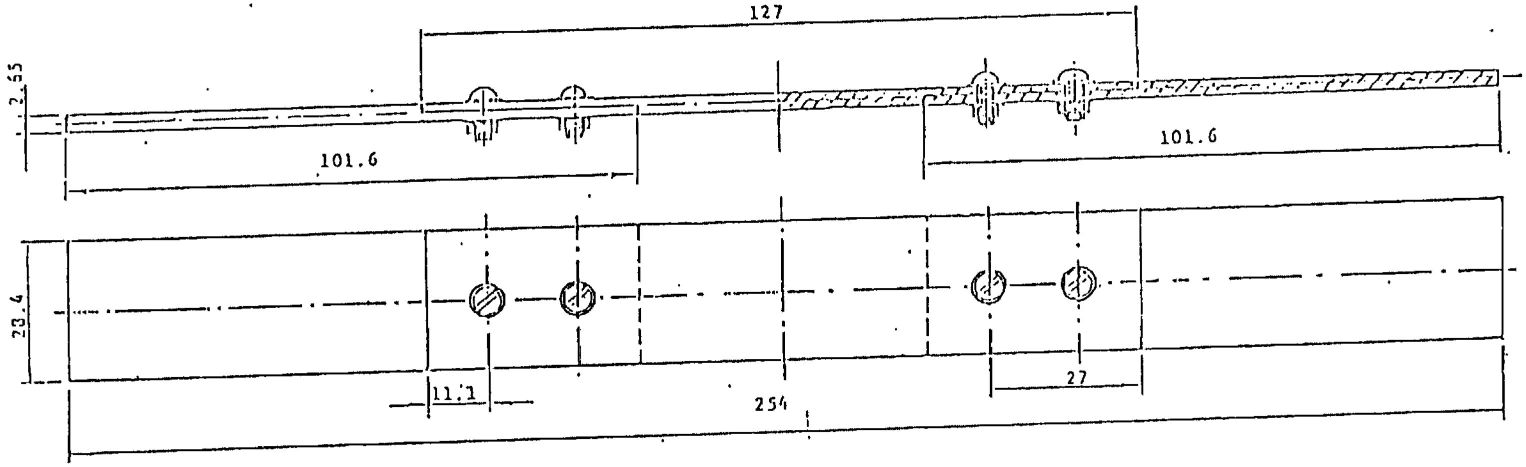

All dimensions in mm

Figure 68. Graphite Epoxy Beam with Bolted Butt Joints

Table 9

Damping of Various Graphite Epoxy Beams

Beam		Mode	Resonance Frequency		Damping Ratio	
No.	Type & Size	No.	Atmospheric	0.1 mm Hg	Atmospheric	0.1 mm Hg
1	Without Joints 254x28.4x2.65mm	1	352Hz		0.06%	
			356Hz	357Hz	0.05%	0.04%
		3	1871Hz		0.04%	
2	Without Joints 200x15x2.5mm	1	472Hz		0.06%	
3	Bolted Single Lap Joint 254x28.4mm Fig. 64	1	343Hz		0.11%	
			344Hz	344Hz	0.11%	0.10%
		3	1618Hz		0.12%	
4	Bonded Double Lap Joint 190x15mm, Fig. 65	1	1028Hz		0.09%	
5	Bolted Double Lap Joint 300x15mm, Fig. 66	1	1020Hz		0.11%	
6	Bonded-Bolted Double Lap Joint 300x15mm, Fig. 66	1	1021Hz		0.22%	
7	Bonded Scarf Joint 200x15x2.5mm Fig. 67	1	509Hz		0.16%	
8	Bolted Butt Joint 254x28.4mm Fig. 68	1	222		0.51%	
		3	1259		0.11%	

C-3

BIBLIOGRAPHY

1. McRoberts, J.J., Space Telescope, NASA EP-166, Pub. by NASA, Washington, D.C.

2. Davis, L.P., Wilson, J.F., Jewell, R.E., and Roden, J.J., "Hubble Space Telescope Reaction Wheel Assembly Vibration Isolation System," Paper presented at the Damping 86 Workshop, Las Vegas, NV, AFWAL-TR-86-3059, Vol 1, PP. BA1-BA22.

3. Ghitelman, D., The Space Telescope, Gallery Books, N.Y., 1987.

4. Bert, C.W., "Material Damping: An Introductory Review of Mathematical Models, Measures and Experimental Techniques," Journal of Sound and Vibration, 29(2), 1973, pp. 129-153.

5. Lazan, B. J., Damping of Materials and Members in Structural Mechanics, Oxford, Pergamon press, 1968.

6. Scanlan, R.H., "Linear Damping Models and Causality in Vibrations," Journal of Sound and Vibration, 13, 1970, pp. 499-503.

7. Crandall, S.H., "The Role of Damping in Vibration Theory," Journal of Sound and Vibration, 11, 1970, pp. 3-18.

8. Pinsker, W., "Structural Damping," Journal of the Aeronautical Sciences, 16, 1949, p. 699.

9. Naylor, V. D., "Some Fallacies in Modern Damping Theory," Journal of Sound and Vibration, 11, 1970, pp. 278-280.

10. Nashif, A. D., Jones, D.I.G., and Henderson, J.P., Vibration Damping, John Wiley & Sons, New York, 1985.

11. Plunkett, R., "Friction Damping," Damping Application for Vibration Control, Torvik, P. J., ed., ASME Winter Annual Meeting, Chicago, 1980, pp. 65-74.

12. Bert, C.W., and Clary, R.R., "Evaluation of Experimental Methods for Determining Dynamic Stiffness and Damping of Composite Materials," Composite Materials-Testing and Design (third conference), ASTM STP 546, 1974, pp. 250-265.

13. Chu, F. H., and Wang, B. P., "Experimental Determination of Damping in Materials and Structures," Damping Application for

Vibration Control, Torvik, P.J., ed, ASME Winter Annual Meting, Chicago, 1980, pp. 113-122.

14. Crawley, E.F., and Mohr, D.G., "Experimental Measurements of Material Damping in Free-Fall with Tunable Excitation," Paper No. 83-0858, Proc. AIAA/ASME/ASCE/AHS Structures, Structural Dynamics, and Materials Conference, Lake Tahoe, May 1983.

15. Sheen, R.F., and Crawley, E.F., "Experimental Measurement of Material Damping for Space Structures in Simulated Zero-G," M.I.T. Space Systems Laboratory, No. 1-84, December 1983.

16. Asher, G.W., "A Method of Normal Mode Excitation Utilizing Admittance Measurements," Proceedings of the National Specialists Meeting on Dynamics and Aeroelasticity, Fortworth, TX, Institute of Aeronautical Sciences, 1959, pp. 69-76.

17. Zhu, G.H., Crocker, M.J., and Rao, M.D., "Data Processing and Accuracy Analysis of Damping Measurement," Submitted to the Journal of The Acoustical Society of America.

18. Harris, C.M., and Crede, C.E., Shock and Vibration Handbook McGraw Hill, New York, Second edition, 1976.

19. Richardson, M., "Modal Analysis Using Digital Test Systems-Seminar on Understanding Digital Control and Analysis in Vibration Test Systems," Shock and Vibration Information Center Publication, NRL, Washington, D.C., May 1975.

20. Brown, D.L., Allemang, R.J., Zimmerman, Ray and Mergeay, M., "Parameter Estimation Techniques for Modal Analysis," SAE paper No. 790221, 1979.

21. Ramsey, K.A., "Effective Measurements for Structural Dynamics Testing - part II," Sound and Vibration, April 1976, pp. 18-31.

22. Brown, D.L., Carbon, G. and Ramsey, K., "Survey of Excitation Techniques Applicable to the Testing of Automotive Structures," SAE paper No. 770029 1977.

23. Pendered, J.W., and Bishop. R.E.D., "A Critical Introduction to Some Industrial Resonance Testing Technique," Journal of Mechanical Engineering Science, 5(4), 1963, pp. 345-367.

24. Kennedy, C.C., and Pancu, C.D., "Use of Vectors in Vibration Measurement and Analysis," Journal of Aerospace Science, 14(11), 1975, pp. 603-625.

25. Ewins, D.J., Modal Testing - Theory and Practice, John Wiley and Sons, Inc., 1984.

26. Klosterman, A.L., "On the Experimental Determination and Use of Modal Representations of Dynamic Characteristics," Ph.D. Thesis, University of Cincinnati, 1971.

27. Gaukroger, D.R., Skingle, C.W., and Heron, K.H., "Numerical Analysis of Vector Response Loci," Journal of Sound and Vibration, 29(3), 1973, pp. 341-353.

28. Marples, V., "The Derivation of Modal Damping Ratios from Complex - Plane Response Plots," Journal of Sound and Vibration, 31(1), 1973, pp. 105-117.

29. Woodcock, D.L., "On the Interpretation of the Vector Plots of Forced Vibrations of a Linear System with Viscous Damping," Aeronaut. Quart., 14(1), 1963, pp. 45-62.

30. Manetje, J.J., "Transfer Function Identification Using a Complex-Plane Response Plots," Journal of Mechanical Engineering Science, 15(5), 1973, pp. 339-345.

31. Richardson, M.H., and Formenti, D.L., "Parameter Estimation from Frequency Response Measurements Using Rational Fraction Polynominals," Proc. of 1st Intl. Modal Analysis Conference, published by Union College, Schenectady, New York, 1982, p. 167.

32. DMTA - Dynamic Mechanical Thermal Analyzer, Instruction Manual Polymer Laboratory, England.

33. Read, B.E., and Dean, G.D., The Determination of Dynamic Properties of Polymers and Composites, John Wiley and Sons, Inc., NY 1978, Chapter 2.

34. Fahy, F., "Measurements of Input Power to a Structure," Journal of Sound and Vibration, 10(3), 1969, pp 517-518.

35. Nakayama, K., and Crocker, M.J., "Prediction of Vibration Energy Flow in a Rectangular Box with Application to Operator Enclosures," Report No. 2, R.W. Herrick Laboratories, Purdue University, Report No. HL 79-11 1979.

36. Lyon, R.H., Statistical Energy Analysis of Mechanical Systems, M.I.T. press, 1975.

37. Cremer, L., Heckl, M., Ungar, E.E., Structureborne Sound Springer-Verlag, New York, 1973.

38. Clarkson, B.L., and Pope, R.J., "Experimental Determination of Modal Densities and Loss Factors of Flat Plates and Cylinders," Journal of Sound and Vibration, 77(4), pp. 535-549.

39. Ranky, M. F., and Clarkson, B.L., "Frequency Average Loss Factors of Plates and Shells," Journal of Sound and Vibration, 89(3), 1983, pp. 309-323.

40. Clarkson, B.L., and Brown, K.T., "Acoustic Radiation Damping," ASME publication, 85-DET-24 1985.

41. Oberst, H. and Frankenfeld, K., "Uber die Dampfung der Biegeschwin-gurgen dunner Bleche durch festhaltende Belage," Acoustica, 2, Leaflet 4, AB, 1952, 181-194, part I, and Vol. 4, part 2, 1954, p. 433.

42. ASTM Std. E756-83, Standard Method for Measuring Vibration-Damping Properties of Materials.

43. Nashif, A.D., "New Method for Determining Damping Properties of Viscoelastic Materials," Shock and Vibration Bulletin, 36(4), 1967, pp. 37-47.

44. Jones, D.I.G., "An Alternative System for Measuring Complex Dynamic Moduli of Damping Materials," Shock and Vibration Bulletin, 45(5), 1975, pp. 99-106.

45. Cannon, C.M., Nashif, A.D., and Jones, D.I.G., "Damping Measurements on Soft Viscoelastic Materials Using a Tuned Damper Technique," Shock and Vibration Bulletin," 38(3), 1968, pp. 154-163.

46. Richter, H.P.H., "Photographic Method for Measuring Material Damping and Dynamic Young's Modulus at low Frequencies Applied to a Fiberglas Reinforced Resin Structure," Proceedings of the 18th Annual Technical and Management Conference, Soc. of Plastics Industry, Inc. Sect. 4-D 1963.

47. Rodden, W.P., and Whittier, J.S., "Damping of Shaker-Excited Beams Calculated Solely from Displacement Amplitude Measurements, J. Acoust. Soct. of Am., 34(4), April 1962, p. 469.

48. Bland, D.R., and Lee, E.H., "Calculation of Complex Modulus of Linear Viscoelastic Materials from Vibrating Reed Measurements," J. Appl. Phys.,26(12), Dec. 1955, p. 1497.

49. Granick, N., and Stern, J.E., "Material Damping of Aluminum by a Resonant - Dwell Technique," NASA TN D-2893, 1965.

50. Wambsganss, M.W., Jr., Boers, B.L., and Rosenberg, G.S. "Method for Identifying and Evaluating Linear Damping Models in Beam Vibrations," Shock and Vibration Bulletin, 36, 1967, pp. 65-74.

51. Gibson, R.F., Yau, A., and Riegner, D.A., "An Improved Forced-Vibration Technique for Measurement of Material Damping," Experimental Techniques 6(2), April 1982, pp. 10-14.

52. Gibson, R.F., and Plunkett, R., "A Forced Vibration Technique for Measurement of Material Damping," Experimental Mechanics, 17(8), August 1977, pp. 297-302.

53. Sekiguchi, H., and Asami, T., "Measurement of Large Damping," Bulletin of JSME, 25(204), 1982, pp. 986-993.

54. Hillier, K.W., "The Measurement of Damping Elastic Properties," Progress in Solid Mechanics 2, North-Holland Publishing Co., Amsterdam, 1961, pp. 201-243.

55. Bert, C.W., "Composite Materials: A Survey of the Damping Capacity of Fiber Reinforced Composites," Damping Application for Vibration Control, ed. Torvik, P.J., ASME publication, AMD-Vol. No. 38, 1980, pp. 53-63.

56. Gibson, R.F., and Wilson, D.G., "Dynamic Mechanical Properties of Fiber-Reinforced Composite Materials," Shock and Vibration Digest, 1979, pp. 3-11.

57. Gibson, R.F., "Recent Research on Dynamical Properties of Fiber Reinforced Composite Materials and Structures," Shock and Vibration Digest, 15(2), 1983, pp. 3-15.

58. Schultz, A.B., and Tsai, S.W., "Dynamic Moduli and Damping Ratios in Fiber-Reinforced Composites," Journal of Composite Materials, 2(3), 1968, pp. 368-378.

59. Jones, E.R., et al., "Damping Measurement of a Controlled Composite Material," J. Acoust. Soc. Am. (57), 1975, pp. 1465-

60. Rehfield, L.W., Briley, R.P., and Putter, S., "Dynamic Tests of Graphite/Epoxy Composites in Hygrothermal Environments," Composites for Extreme Environment, ASTM, STP 768, 1982, pp. 148-160.

61. Leung, C.L., "Space Environmental Effects on Graphite Epoxy Composites," Composites for Extreme Environments, ASTM STP 768, 1982, pp. 110-117.

62. Shen, Chi-Hung, and Springer, G.S., "Moisture Absorption and Desorption of Composite Materials," J. Comp. Materials, 10(1), 1976, pp. 2-20.

63. Loos, A.C., and Springer, G.S., "Moisture Absorption of Graphite-Epoxy Composites Immersed in Liquids and in Humid Air," J. Comp. Materials, 13(4), 1979, pp. 131-147.

64. Loos, A.C., and Springer, G.S., "Moisture Absorption of Polyester-E. Glass Composites," J. Comp. Materials, 14(4), 1980, pp. 142-153.

65. Jones, D.I.G., "Viscoelastic Materials for Damping Applications," Damping Application for Vibration Control, ed. Torvik, P.J., ASME publication, AMD-Vol. 38, 1980, pp. 27-51.

66. Yakovlev, A.P., and Bykovskii, A.I., "Study of the Damping Properties of Certain Types of Glass Textolites at Various Temperatures," Strength of Materials, 4(6), 1972, pp. 681-685.

67. Clary, R.R., "Vibration Characteristics of Unidirectional Filamentary Composite Material Panels," Composite Materials: Testing and Design (2nd Conf.) ASTM STP 497, 1972, pp. 415-438.

68. Mazza, L.T., Paxson, E.B., and Rodgers, R.L., "Measurement of Damping Coefficients and Dynamic Modulus of Fiber Composites," U.S. Army Aviation Materials Laboratories, USAAV LABS-TN-2 (NTIS Document AD-869025, 1970).

69. Paxson, E.B., Jr., "Real and Imaginary Parts of the Complex Viscoelastic Modulus for Boron Fiber Reinforced Plastics," J. Acoust. Soc. Am., 57(4), 1975, pp. 891-898.

70. Adams, R.D., and Bacon, D.G.C., "Effect of Fiber Orientation and Laminate Geometry on the Dynamic Properties of Carbon-Fiber-Reinforced Plastics," J. Comp. Materials, 7(4), 1973, 402-428.

71. Schultz, A.B., and Tsai, S.W., "Measurement of Complex Dynamic Moduli for Laminated Fiber-Reinforced Composites," J. Comp. Materials Vol. 3, 1969, p. 434.

72. Suarez, S.A., "Optimization of Internal Damping in Fiber Reinforced Composite Materials," Ph.D. Dissertation, University of Idaho, Dec. 1984.

73. Suarez, S.A., Gibson, R.G., Sun, C.T., and Chaturvedi, S.K., "The Influence of Fiber Length and Fiber Orientation on Damping and Stiffness of Polymer Composite Materials," presented at the "Damping 86" workshop, March 5-7, 1986, Las Vegas, NV.

74. Kishore, N.N., Ghosh, A., and Agarwal, B.D., "Damping Characteristics of Fiber Composites with Imperfect bonding, Part 1," Journal of Reinforced Plastics and Composites, Vol. 1, Jan. 1982, pp. 40-63.

75. Kishore, N.N., Ghosh, A., and Agarwal, B.D., "Damping Characteristics of Fiber Composites with Imperfect Bonding, Part II," Journal of Reinforced Plastics and Composites, Vol. 1, Jan. 1982, pp. 64-81.

76. Nelson, D.J., and Hancock, J.W., "Interfacial Slip and Damping in Fiber Composites," Journal of Materials Science, Vol. 13, 1978, pp. 2429-2440.

77. Nelson, D.J., "Dynamic Testing of Discontinuous Fiber Reinforced Composite Materials," Journal of Sound and Vibration, 64(3), 1979, pp. 403-419.

78. Gibson, R.F. and Plunkett, R., "Dynamic Mechanical Behavior of Fiber Reinforced Composites: Measurement and Aalysis," J. Comp. Materials, 10, 1976, pp. 325-341 (1976).

79. Adams, R.D., et al., "A Vibration Technique for Non-Destrutively Assessing the Integrity of Structures," Journal of Mechanical Engineering Science, 1978, 2(2).

80. Cawley, P., and Adams, R.D., "A Vibration Technique for Non-Descructive Testing of Fiber Composite Structures," J. Comp. Materials, Vol. 13, 1979, p. 161.

81. Cawley, P., and Adams, R.D., "The Location of Defects in Structures from Measurements of Natural Frequencies," Journal of Strain Analysis, 1979, 14(2),.

82. Schultz, A.B., and Warwick, D.N., "Vibration Response: A Non-Destructive Test for Fatigue Crack Damage in Filament - Reinforced Composites," J. Comp. Materials, 5(3), 1971, pp. 394-404.

83. DiBenedetto, A.T., et al., "Non-Destructive Determination of Fatigue Crack Damage in Composites Using Vibration Tests," Journal of Materials, 7(2), 1972, pp. 211-215.

84. Kim, H.C., and Mattews, F.L., "Hysteresis Behaviors in Carbon Fiber-Reinforced Plastics," Journal of Physics, Series 2, Vol.6D, No. 15, 1973, pp. 1755-1761.

85. Hashin, Z., "Complex Moduli of Viscoelastic Composite: II, Fiber Reinforced Materials," Int. J. Solids Struc., 6(6), 1970, pp. 797-807.

86. Chang, S., and Bert, C.W., "Analysis of Damping for Filamentary Composite Materials," Composite Materials in Engineering Design, Metals Park, OH, 1973, pp. 51-62.

87. Ni, R.G., and Adams, R.D., "the Damping and Dynamic Moduli of Symmetric Laminated Composite Beams - Theoretical and Experimental Results," J. Comp. Materials, 18, 1984, pp. 104-121.

88. Lin, D.X., Ni, R.G., and Adams, R.D., "Prediction and Measurement of the Vibration Damping Parameters of Carbon and Glass - Fiber Reinforced Plastic Plates," J. Comp Materials, 18(3), 1984, pp. 132-152.

89. Cawley, P., and Adams, R.D., "The Predicted and Experimental Natural Modes of Free Free CFRP Plates," J. Comp. Materials, 12(10), 1978, p. 336.

90. Hwang, S.L., and Gibson, R.F., "Micromechanical Modeling of Damping in Discontinuous Fiber Composites Using a Strain Energy/Finite Element Approach," Paper presented at ASME Winter Annual Meeting, Miami Beach, FL, 85-WA/MATS-3 Nov. 1985.

91. Hwang, S.J., "Finite Element Modeling of Damping in Discontious Fiber Reinforced Composites," M.S. Thesis, University of Idaho, April 1985.

92. Johnson, C.D., and Kienholz, D.A., "Finite Element Prediction of Damping in Structures with Constrained Viscoelastic Layers," AIAA Journal, 20(9), 1982, pp. 954-957.

93. Beards, C.F., "Damping in Structural Joints", Shock Vib, Dig. 11(9), Sept. 1979, pp. 35-41.

94. Beards, C.F., and Williams, E.J., "The Damping of Structural Vibration by Rotational Slip in Joints," J. Sound Vib., 53(3) 1977, pp 33-34.

95. Beards, C.F., and Imam, I.M.A., "The Damping of Plate Vibration by Interfacial Slip between Layers," Intl. J. Mach. Tool Des. Res., 18, 1973, pp. 131-137.

96. Earles, S.W.E. and Mansoori, F.S., "Frictional Damping Applied to a Cantilever Beam Structure: A Theoretical and Experimental Response Comparison." Int. J. Mach. Tool Des. 14, 1974, pp. 111-124.

97. Tomlinson, G.R. and Hibbert, J.H., "Identification of the Dynamic Characteristics of a Structure with Coulomb Friction," J. Sound Vib., 64, 1979, p. 3.

98. Earles, S.W.E., "Theoretical Estimation of the Frictional Energy Dissipation in a Simple Lap Joint," J. Mech. Engr. Sci., 8, 1966, pp 207-214.

99. Williams, D., "Method of Damping out Bending Vibration of Beam-like Structures by Dry or Coulomb Friction," J. Mech. Engr. Sci., 2, 1960, pp. 77-87.

100. Maidinik, G., "Energy Dissipation Associated with Gas-pumping at Structural Joints," JASA, 40, 1966, pp. 1064-

101. Ungar, E.E., and Carbonell, J.R., "On Panel Vibration Damping Due to Structural Joints," AIAA J. 1966, pp. 1385-1390.

102. Earles, S.W.E., and Williams, E.J., "A Linearlized Analysis for Frictionally Damped Systems," J. Sound Vib., 1972, pp 445-458.

103. Richardson, R.S.H., and Nolle, H., "Energy Dissipation in Rotary Structural Joints," J. Sound Vib., 54(4), 1977, pp 577-588.

104. Crawley, E.F., and O'Donnell, K.J., "Identification of Nonlinear System Parameters in Joints Using the Force-State Mapping Technique," AIAA Paper 86-1013-CP, 27th Structures, Structural Dynamics and Materials Conference, San Antonio, TX, 1986.

105. O'Donnell, K.J., and Crawley, E.F., "Identification of System Parameters in Space Structure Joint Elements Using the Force-State Mapping Technique," M.I.T. Space Systems Laboratory Report No. 16-85.

106. Goland, M., and Reissner, E., "The Stresses in Cemented Joints," Journal of Applied Mechanics, Vol. 11, March 1944, pp. A17-A27.

107. Ojalvo, I.U., and Eidinoff, H.L., "Bond Thickness Effects upon Stresses in Single-Lap Adhesive Joints," AIAA Journal, Vol. 16, No. 3, 1978, pp. 204-211.

108. Carpenter, W.C., "A Comment on Two Current Adhesive Lap Joint Theories," AIAA journal, Vol. 18, No. 3, 1980, pp. 350-352.

109. Kline, R.A., "Stress Analysis of Adhesively Bonded Joints," Adhesive Joints, ed. by Mittal, K.L., proc. of the International Symp. on Adhesive Joints, Sept. 1982, Kansas City, Missouri, pp. 587-609.

110. Delale, F., and Erdogan, F., "Viscoelastic Analysis of Adhesively Bonded Joints," Journal of Applied Mechanics, Vol. 48, June 1981, pp. 331-336.

111. Renton, W.J., and Vinson, J.R., "Analysis of Adhesively Bonded Joints Between Panels of Composite Materials," Journal of Applied Mechanics, March 1977, pp. 101-106.

112. Delale, F., Erdogan, F., and Aydinoglu, M.N., "Stresses in Adhesively Bonded Joints" A closed form solution," J. Composite Materials, vol. 15, May 1981, pp 249-271.

113. Hart-Smith, L.J., "Analysis and Design of Advanced Composite Bonded Joints," NASA CR-2218, April 1974.

114. Hart-Smith, L.J., "Adhesive-Bonded Double-Lab Joints, "NASA CR-112235, January 1973.

115. Hart-Smith, L.J., "Adhesive-Bonded Single Lap Joints, "NSAS CR-112236, January 1973.

116. Hart-Smith, L.J., "Adhesive-Bonded Scarf and Stepped-Lap Joints, "NASA CR-112237, January 1973.

117. Mead, D.J., "A Comparison of Some Equations for the Flexural Vibration of Damped Sandwich Beam," Journal of Sound and Vibration, 83(3), 1982, pp. 363-377.

118. Nakra, B.C., "Vibration Control with Viscoelastic Materials," Shock and Vibration Digest, 8(6), 1976, pp. 3-12.

119. Saito, H., and Tani, H., "Vibrations of Bonded Beams with a Single Lap Adhesive Joint," Journal of Sound and Vibration, 92(2), 1984, pp. 229-309.

120. Prucz, J., "Analytical and Experimental methodology for Evaluating Passively Damped Structural Joints, " Ph.D. Dissertation, Georgia Institute of Technology, May 1985.

121. Blevins, R.D., Formulas for Natural Frequency and Mode Shape, Van Nostrand Reinhold Co., New York 1979.

122. Timoshenko, S., Young, D.H., and Weaver, W., Jr., Vibration Problems in Engineering, 4th ed., John Wiley & Son, New York, 1974.

123. Baker, W.E., Woolam, W.E., and Young, D., "Air and Internal Damping of Thin Cantilever Beams", International Journal of Mechanical Sciences, 9,1967, 743-766.

124. Morse, P.M., and Ingrad, K.U., Theoretical Acoustics, McGraw-Hill, 1968.

125. The Fundamentals of Signal Analysis, Hewlett Packard Application Note 243, 1985.